Visible Light Optical Coherence Tomography of the Retina: From Technical Improvements to Discovering New Bands

By

AARON MICHAEL KHO

DISSERTATION

Submitted in partial satisfaction of the requirements for the degree of

DOCTOR OF PHILOSOPHY

in

Biomedical Engineering

in the

OFFICE OF GRADUATE STUDIES

of the

UNIVERSITY OF CALIFORNIA

DAVIS

Approved:

_____

Vivek J. Srinivasan, Chair

_____

Glenn C. Yiu

_____

Robert J. Zawadzki

_____

Ravi S. Jonnal

Committee in Charge

2022

ACKNOWLEDGEMENTS

First, I would like to thank Professor Vivek Srinivasan for giving me the opportunity to be a part of his research group. He always provided the necessary help and pushed me to be a better researcher. His enthusiasm and support in these projects helped me through many obstacles that I didn't believe I could overcome. I would also like to thank my dissertation committee members, Professor Robert Zawadzki, Professor Ravi Jonnal, and Professor Glenn Yiu. Robert mentored me, especially during my first two years, and always provided the right balance between constructive criticism and support. Even when I would make mistakes, he would be understanding and be focused on a solution. Ravi always provided great advice on my research and life that I still treasure to this day. Glenn is extremely knowledgeable and taught me a lot about the retina and age-related macular degeneration.

I would like to acknowledge Marie Burns, Theresa Geer, and all of the people involved with the T32 Vision Science training grant. Marie was very supportive and always willing to help.

To the current and former lab members of the Srinivasan lab, I want to thank all of you for creating a friendly and collaborative working environment that made this a joyful experience. I want to thank Dr. Shau Poh Chong and Dr. Conrad Merkle for helping me tremendously during my first couple years in the program and for teaching me a lot about optical alignment and OCT. I also want to thank Dr. Tingwei Zhang for teaching me the fundamentals of spectrometer alignment which became very useful in my projects. Dr. Wenjun Zhou worked on a completely different project during our time together, but I want to thank him for constantly going above and beyond to help me every time I had a question. Whenever I visited his family, he made sure I felt at home. I want to thank Dr. Oybek Kholiqov for his enthusiasm and attitude that frequently lifted my mood and for all the great discussions. Last but not least, I would like to thank Dr. Jun Zhu for dealing with me and Oybek but also for providing a lot of emotional and technical support.

Next, I would like to thank my girlfriend, Vivia, for providing an enormous amount of support throughout the years. She continuously went out of her way to help and was always understanding when I had to put research first.

Lastly, I would like to thank my family. Thank you to my mom, Shirley, and my dad, Eli, for supporting me through my ups and downs. They always believed in me and gave me everything I needed to be successful in life. Thank you to my brother, Hezron, for all of the good food we ate when I visited home. Thank you to my grandmother for bringing up my mood every time I call. Thank you to my entire family for helping me achieve my dreams. All of this success is because of you.

ABSTRACT

Optical Coherence Tomography (OCT) has greatly advanced the diagnosis and management of many retinal diseases by enabling *in vivo* volumetric structural imaging of the retina with high resolution. Usually, retinal OCT is performed at near-infrared (NIR) wavelengths, limiting both axial resolution and contrast for molecules that play a role in vision. Though NIR OCT defines biomarkers that quantify progression of dry age-related macular degeneration (AMD), NIR OCT cannot yet delineate the finest structural and functional changes that define AMD.

Visible light OCT has the ability to delineate these changes by providing high resolution and spectroscopic information that can aid in assessing AMD. The higher axial resolution can observe the retinal pigment epithelium (RPE) and Bruch's membrane (BM) on a sub-micron scale, potentially expanding our knowledge of AMD progression. The molecular contrast can be used for retinal oximetry of blood vessels and potentially photopigment or melanin densitometry which could portend early AMD.

Although visible light OCT holds the promise of micron and even unprecedented sub-micron axial resolution and molecular contrast, visible light OCT systems to date have not delivered on this promise. There are many confounding factors that need to be addressed before the full potential of visible light OCT is realized. These include the cost of hardware, size of imaging system, safety considerations limiting light exposure, excess noise in light sources, motion artifacts, chromatic aberrations, and spatially-dependent dispersion. This thesis advances the development of visible light OCT by addressing all of the previously listed issues. With these advances, we can now clearly visualize additional retinal bands in the mouse (and human) retina such as the RPE, BM, inner plexiform layer (IPL) sublaminae, and the dark band inner to the external limiting membrane (ELM).

TABLE OF CONTENTS

Chapter 1: Background and Introduction

1.1. Age-related Macular Degeneration (AMD)

AMD is a leading cause of vision loss in the Western world in individuals over 50 years of age [1]. It exists in two forms, "dry" AMD, which affects 80-90% of patients, and "wet" AMD, a neovascular transformation that affects 10-20% of patients. As age is the major risk factor for AMD, the precursors of AMD are changes in older eyes [2]; namely, diffuse thickening of BM [2-4] and deposits in or below the RPE basal lamina [5], revealed by histology. This is followed by subsequent development of clinically-detectable drusen, yellow deposits between the RPE basal lamina and inner collagenous layer of BM, which are often accompanied by retinal pigment epithelium (RPE) irregularities, and later, photoreceptor and choriocapillaris changes. The risk of progression to later stages is determined by the presence of RPE depigmentation, drusen size [6] and reticular pseudodrusen [7]. A large druse progresses to hyperpigmentation, followed by regression, hypopigmentation, and eventual RPE atrophy, but other pathways are possible. In the absence of neovascular, or "wet," transformation, the end stage of dry AMD is geographic atrophy (GA). The progression of GA is inexorable, but progression rates are highly variable, ranging from 0.53 to 2.6 mm^2/year, depending on lesion size, location, multifocality, autofluorescence patterns, and fellow eye status [8], in addition to genetic [9] and environmental factors. Visual acuity is lost when the fovea is involved [10].

While wet AMD can often be effectively managed with anti-vascular endothelial growth factor (anti-VEGF) injections [11], there are no known effective treatments for GA, apart from lifestyle modifications and nutritional supplements, but there are numerous ongoing dry AMD clinical trials. Though wet AMD remains the leading cause of vision loss, GA has a higher incidence (1.9% vs. 1.8%) among Caucasians over 50 in the U.S. [12]. As management of wet AMD improves, and life expectancies increase, strategies to halt or slow the progression of GA and resulting vision loss are increasingly needed.

The only accepted intervention for dry AMD right now is oral oxidants that slow progression of intermediate AMD [13, 14] based on AREDS (Age-Related Eye Disease Study) and AREDS2. Other investigational treatment strategies for dry AMD include complement inhibition, targeting inflammation, visual cycle modulation, cell replacement therapy, laser therapy, choroidal blood flow restoration, and neuroprotection [15-18].

AMD can be diagnosed using a variety of retinal examinations and imaging techniques such as visual fields test, color fundus photography, fundus autofluorescence (FAF), fluorescein angiography, optical coherence tomography (OCT), and OCT angiography. Color fundus photography and OCT are used to observe drusen formations, fluorescein angiography and OCT angiography are used to observe the growth of new vessels or flow voids, FAF is used to observe lipofuscin autofluorescence, and the visual field test is used to observe any impairments or distortions in the visual field.

Biomarkers of both early disease progression [8] and impending atrophy [18] are needed, at a stage when interventions may be most effective [8]. Biomarkers of early AMD would provide a clearer picture of pathogenesis, and biomarkers that predict impending atrophy could help to inform the design of clinical trials. Histopathology and imaging studies suggest a sequence of events where RPE stress and pigmentary changes, exacerbated by deposits near Bruch's membrane, precedes atrophy [18]. However, in clinical NIR OCT, the RPE is barely distinguished from Bruch's membrane and the photoreceptors [19], and quantification is not possible, particularly if photoreceptor interdigitation is intact, as expected in the normal retina or far from a lesion.

1.2. Motivation of visible light OCT

Although visible light OCT was first proposed almost two decades ago [20, 21], it has recently increased in popularity in the past eight years [22] due to the commercialization of stable supercontinuum light sources with reduced noise. These light sources provide the high power and high spatial coherence needed in OCT. The main advantage of supercontinuum light sources, however, is the low temporal coherence in

the visible light range. With the development of hardware such as these light sources and broadband visible light fiber couplers [23], visible light OCT has been adopted and developed by many groups for retinal imaging [22-29] due to the ability to perform spectroscopy, and the potential to achieve ultrahigh axial resolution of less than a micron.

1.2.1 Spectroscopy of retinal chromophores

Absorption by tissue in the visible light is usually a concern in biomedical optical imaging due to decreased penetration, however visible light imaging of the retina takes advantage of the eye's natural transparency needed for vision.

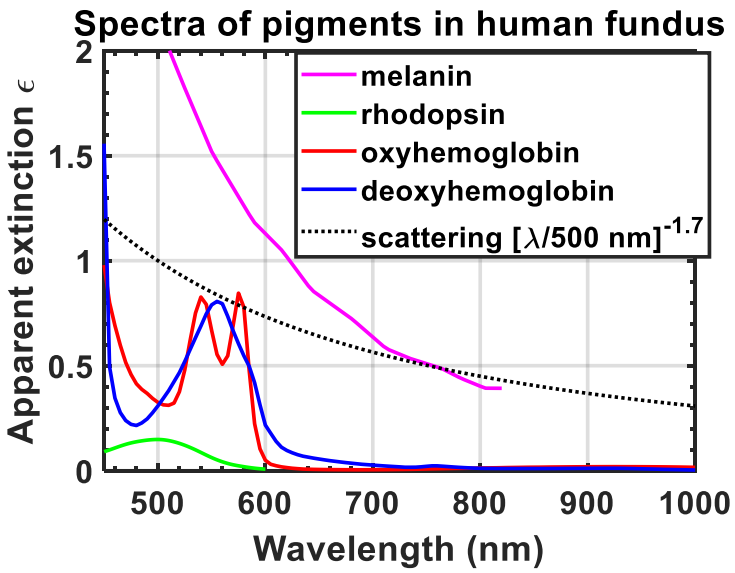

Figure 1. Extinction coefficient of hemoglobin, melanin, and rhodopsin. Scattering coefficient of tissue [29].

In the retina, chromophores, such as melanin, rhodopsin, oxyhemoglobin, and deoxyhemoglobin, have increased absorption in the visible light range, compared to the near infrared region. In addition, the visible absorption spectra have very unique shapes that aids distinguishing chromophores from each other. These factors allow spectroscopic techniques based on absorption to perform more reliably in the visible light range [22] than in the infrared range. In fact, many groups have adopted visible light OCT mainly for retinal

oximetry, which estimates saturation, the ratio of oxyhemoglobin to oxyhemoglobin and deoxyhemoglobin, using spectroscopic methods [30, 31].

1.2.2 Visualization of thin retinal layers

A unique property of OCT is the uncoupling of the transverse resolution and axial resolution (in the low numerical aperture limit) so both can be optimized without mutual tradeoffs. Axial resolution in OCT is described by the following equation:

$$\Delta z = \frac{2\ln 2}{n\pi}\frac{\lambda_0^2}{\Delta\lambda}, \tag{1}$$

where Δz is the axial resolution, n is the refractive index, λ_0 is the center wavelength, and $\Delta\lambda$ is the spectral bandwidth of the spectrum. The primary methods to increase axial resolution are to either increase the spectral bandwidth of the light source or use shorter wavelengths. Commercial supercontinuum light sources provide the ability to increase axial resolution using both methods. Improvements have led to axial resolution of less than a micron [21, 26] and improved the visualization of thin, subtle layers such as Bruch's membrane [32, 33], Retinal Pigment Epithelium (RPE) [32, 33], and the Inner Plexiform Layer (IPL) sublaminae [34].

1.3. Challenges of visible light OCT

While the advantages of visible light OCT are straightforward to describe and understand, there are many issues that need to be addressed to realize the full potential of visible light OCT. The early visible light OCT systems, including from our group, which did not fully appreciate or address some of these issues, resulted in images which were comparable or inferior to infrared OCT. These issues include the rapid spectral changes of the refractive index in the visible light range, exposure to more harmful electromagnetic radiation, and visible light hardware development.

1.3.1 Pupil constriction

Exposure of the eye to a bright visible light stimulus causes immediate involuntary constriction of the pupil. This natural evolutionary adaptation prevents excessive exposure to white light; however, this decreases image quality when imaging with visible light OCT. Imaging a constricted pupil causes vignetting and ultimately limits the field of view. Clinicians typically use mydriatic eye drops to induce dilation of the pupils, but patients ultimately prefer no dilation since it causes the eyes to be sensitive to daylight for a few hours. Dilation interferes with daily life activities causing clinicians and patients to prefer OCT imaging which does not require dilation.

1.3.2 Limited light exposure

Light safety in ophthalmic OCT imaging is always a main concern, however there are additional sources of damage in the visible light region compared to the near infrared region. Safety standards, such as the American National Standards Institute (ANSI) Standard [35], were developed to determine safe levels of light exposures in the eye. The ANSI standards considers the main sources of damage in the visible light range to be photothermal damage and photochemical damage.

When tissue absorbs light, the energy is typically converted into heat through non-radiative relaxation which subsequently increases the temperature [36]. Excessive temperature rises can damage the tissue. An example of an absorber that can mediate thermal damage in the retina is melanin. Damage can occur at longer exposure times particularly in the shorter wavelength region of the visible spectrum. Photochemical damage is thought to result from the exposure of retinal tissue to generated free radicals [36]. Light in the higher energy part of the visible spectrum produces free radicals that can induce lipid peroxidation and lysosomal dysfunction. Free radicals are generated by splitting the bond of another molecule by direct electron exchange or direct hydrogen exchange. In the case of singlet oxygen, absorption of the radiant energy leads to energy transfer from the excited chromophore to oxygen [36]. In the absence of antioxidants, free radicals can react with membranous structures and cause cell damage and disruption.

A recent study [37] has found that there are additional damage mechanisms that were not considered in the previous ANSI standards. Two unexpected changes were found with light exposure deemed safe by the ANSI standards: retinal pigment epithelium autofluorescence photobleaching and retinal pigment epithelium disruption. Based on these findings, it is beneficial to further decrease light exposure in visible light OCT to prevent any damage from mechanisms which are not yet fully understood.

1.3.3 Excess noise in light sources

Traditional near infrared OCT uses superluminescent diodes (SLD) which are generally shot noise limited and provide the best achievable sensitivity for a given power assuming that detector noise is negligible. In comparison, broadband supercontinuum light sources typically have excess noise coefficients more than two orders-of-magnitude larger than near infrared SLDs. Visible light SLDs with sufficiently low temporal coherence are not currently available so most visible light OCT systems incorporate supercontinuum light sources, with rare exceptions [38]. Although the bandwidths and power are sufficient for ultrahigh resolution visible light OCT, the large excess noise of these light sources impairs sensitivity. More excess noise would be present with a shorter integration time that averages fewer pulses, so there would be more intensity fluctuations between a-lines. Higher powers or longer integration times (slower speeds) are used to compensate for the added noise. Thus excess noise prevents high speed visible light OCT as well.

1.3.4 Cost and size of light source

Current near infrared OCT systems use SLDs that are relatively cheap (~$1000) and with a size comparable to a standard smartphone. However, the limited options of broadband visible light sources leave current visible light OCT researchers with only costly supercontinuum light sources (~>$50,000) with sizes comparable to a microwave. The cost and size issues are huge limitations to commercial visible light OCT systems and until these are addressed, it will likely only be mainly a research tool.

1.3.5 Motion artifacts

Fixational eye movements are involuntary actions of the eye that occur even when a patient is fixated on a stationary target. These movements during OCT acquisition causes the retina to displace from the optimal position, sometimes resulting in sub-par image quality. There are active [39, 40] and passive retinal tracking [41, 42] techniques that compensate for motion artifacts caused by fixational eye movements, but these methods require expensive hardware [39, 40] and/or can be computationally expensive [41, 42]. Techniques such as phase-sensitive OCT [43-46] require phase shift between scans between $-\pi$ to $+\pi$ and would either need very accurate active retinal tracking from adaptive optics (AO) [47] or MHz a-line rate [44, 46, 48, 49]. As faster line scan cameras and swept source light sources are being developed, there is a general shift in the ophthalmic OCT community [44, 46, 48, 49] to adopt faster acquisition speeds to address motion artifacts.

Motion artifacts are especially a problem in the visible light OCT field due to the limited light exposures and speed imposed by ANSI limits and excess noise, respectively. With slower speeds than near infrared OCT, visible light OCT has significant axial and transverse motion between b-scans that has limited imaging protocols and field of view.

1.3.6 Chromatic aberrations

The chromatic aberrations imposed by the eye limits the achievable resolution of visible light OCT. Chromatic aberration is substantially larger for visible wavelengths than for near infrared wavelengths [50]. In particular, both optical glass used in lenses and ocular media in the human eye exhibit large changes in refractive index with wavelength across the visible spectrum. The resulting chromatic aberrations are especially consequential in ultrahigh axial resolution and spectroscopic visible light OCT, where broad bandwidths are needed. Hence, we must consider the impact of chromatic aberrations in both the OCT sample arm (taken to include all elements in the optical path, including the human eye) and the spectrometer.

Longitudinal chromatic aberration (LCA) induces a wavelength dependent focal shift along the optical axis. LCA due to sample arm optics and the human eye can be compensated using optical simulations to design an achromatizing lens [33, 51]. These simulations use a standard eye model and assume similar LCA from the human population.

Transverse chromatic aberration (TCA) induces a wavelength dependent focal shift transverse to the optical axis. Unlike LCA, TCA cannot be mostly suppressed for all patients using an achromatizing lens. TCA has not currently been eliminated in visible light OCT, but there are efforts to minimize the effects of TCA by reducing the beam diameter on the pupil and ensuring that the beam is centered on the pupil.

1.3.7 Spatially-dependent dispersion

Group velocity dispersion occurs due to a variation of the group refractive index as a function of wavelength. Different wavelengths will travel at different speeds. For example, a wavelength with a higher group refractive index will have a lower group velocity. When reflected by a surface, in the case of OCT, that wavelength will appear to be reflected from further away if its group index is not taken into account. Apply this effect to a broadband spectrum, and a single specular reflector, imaged with OCT, will appear broadened due to a range of wavelengths having a range of group velocities.

Water has a much higher group velocity dispersion in the visible light range, compared to near infrared. Different spatial positions in the visible light OCT image will have different optimal dispersion correction values. If these spatial differences are not accounted for, optimizing dispersion correction at one location will cause other areas to have worse axial resolution.

1.4. Visible light OCT improvements that can expand AMD pathology knowledge

AMD is a complicated disease that affects thin structures in the retina which are currently not resolvable with current imaging modalities *in vivo*. Observing slight changes in the retinal structures such as perceived band thickening due to basal deposits can help us better understand AMD pathology. Higher axial resolution

is necessary to spatially resolve BM from the RPE and can be used in longitudinal studies to differentiate and understand the mechanisms of these layers.

The high photopigment bleaching levels of visible light OCT is known to induce water movement, cell swelling, scattering changes, as well as potentially, melanosome movement. There may also be long term changes due to prolonged visible light exposure that need more investigation [37]. In additional, imaging with bright light can be uncomfortable for patients and can deter both clinicians and patients from using visible light OCT. Also, quantification of rhodopsin using visible light OCT requires the acquisition of b-scans prior or at the beginning of bleaching. This task, along with the aforementioned light exposure, requires optimization of OCT sensitivity. Higher sensitivity will allow for similar quality image quality but with lower power incident on the eye.

1.5. Dissertation scope

The projects in the dissertations aims to provide technological improvements to visible light OCT to enable its application to AMD pathology and diagnostics. These projects address the following challenges of visible light OCT: limited light exposure, excess noise, cost and size of light sources, motion artifacts, and spatially dependent dispersion. We have previously addressed longitudinal chromatic aberrations [33], but the issues of pupil constriction and transverse chromatic aberrations remain to be solved. The chapters are organized as followed:

1) Chapter 2 directly compares visible light OCT with OCT in three other spectral bands (860 nm, 1060 nm, and 1325 nm). We notice that visible light OCT provides the unique opportunity to study the outer retina. Prolonged visible light exposure can cause scattering changes in the photoreceptor layers that are yet to be fully understood. With this knowledge, we plan to improve visible light OCT resolution to better resolve layers but also improve visible light OCT sensitivity to allow for less visible light exposure during imaging.

2) Visible light OCT with wider bandwidths is supposed to improve axial resolution, however we saw a disparity between the theoretical and experimental resolution. Chapter 3 investigated inconsistencies between spectral sub-band images and discovered the presence of spatially dependent dispersion. We ran simulations showing that attempting to increase axial resolution without correcting for spatially dependent dispersion can worsen image resolution. Compensating for spatially dependent dispersion provided improved and more consistent axial resolution throughout the image. Visible light OCT images of the pigmented and albino mouse retinas aided in the discovery of the Bruch's membrane band in the pigmented mouse retina.

3) Although axial resolution was improved with better dispersion correction, there still lies an inherent axial resolution broadening with depth due to inconsistent spectral resolution (measured in wavenumber) of the OCT spectrometer as a function of wavelength. The issue of sensitivity rolloff also drastically affects imaging quality if images are not taken near zero delay. Sensitivity rolloff is mainly attributed to the spectral resolution of the OCT spectrometer. Chapter 4 reports the first method to rapidly measure the spectral resolution at all wavelength in the spectrum and in a single dataset. The method, based on excess noise correlations, was used during spectrometer alignment to both improve the overall spectral resolution and reduce the variations in wavenumber spectral resolution as a function of wavelength. As a result, we improved the axial resolution and sensitivity at deeper depths in visible light OCT.

4) Chapter 5 delves deeper into the theory of spectral resolution. We note that spectral resolution and coherence rolloff are Fourier transform pairs. This relationship is used to directly derive the point spread function (PSF) sensitivity rolloff and axial resolution broadening from a single time course measurement and without interferometry. Chapter 5 is an extension of chapter 4 and further aids the spectrometer alignment process for optimal image quality.

5) Excess noise in visible light OCT causes a significant decrease in the signal to noise (SNR) ratio and its effects increase at high line rates. This issue has limited most reported visible light OCT

systems to image at speeds 3-5 times lower than near infrared OCT. Dual balanced detection in spectral domain OCT is a method that can be used to eliminate excess noise but has not yet been reported to sufficiently suppress excess noise. Chapter 6 posits that dual balanced detection requires precise wavelength matching between spectrometers on the order of tens of picometers in wavelength. We propose a method that provides sufficient wavelength matching for excess noise suppression of 22.6 dB. We improved our imaging speed by seven-fold and also decreased our imaging power by more than two-fold, all while using a less expensive light source.

To summarize, this work has enabled visible light OCT to improve in resolution, sensitivity (higher speeds and/or lower imaging power), size, and cost. The improvements have allowed the visualization of new retinal layers such as the Retinal Pigment Epithelium (RPE) [32], Bruch's membrane (BM) [32], dark band inner to External Limiting Membrane (ELM) [52], and Inner Plexiform Layer (IPL) sublaminae [34]. In our subsequent work included in the future directions section, we validated these layers against light and electron microscopy in the mouse retina, which supports that the retina has a consistent organization of organelles and subcellular features which are resolved by visible light OCT. We have also included preliminary work on visible light OCT imaging with AMD mouse models. Continued investigations of the mouse models with visible light OCT can help understand diseases such as AMD that occur on the sub-micron scale.

Chapter 2: OCT retinal imaging at four different spectral bands

2.1. Introduction

Optical Coherence Tomography (OCT) retinal imaging in humans has historically been performed in two near-infrared spectral bands (800 nm and 1050 nm). To determine the light tissue interactions responsible for OCT contrast, and evaluate emerging spectral bands, we investigate wavelength-dependent reflectivity of different retinal layers using custom-built mouse retinal imaging systems operating in distinct spectral

ranges (575 nm, 860 nm, 1060 nm, and 1325 nm). We subsequently investigated perturbations in the outer retina seen with the OCT system centered in the visible light range.

2.2. Methods

2.2.1 System design

We used four spectral domain (SD) or swept-source (SS) OCT systems for *in vivo* mouse retinal imaging: 575 nm (SD), 860 nm (SD), 1060 nm (SS), and 1325 nm (SD). All systems have ~100-135 nm full width half maximum bandwidth and similar transverse resolutions through scanning optic modifications.

The 860 nm SD-OCT system [53] and the 1060 nm SS-OCT system [54] have both been previously described. The 1325 nm SD-OCT system was modified from a previously reported system [55]. The scan lens and ocular lens were modified to have focal lengths of 100 mm and 15 mm, respectively. A free-space visible light SD-OCT system centered at 575 nm for *in-vivo* murine retinal imaging was built with a supercontinuum light source (EXW-12, NKT Photonics A/S, Denmark). The collimated beam was filtered using a combination of filters and sapphire window to achieve a spectral range of 475-650 nm and coupled to a 50/50 beamsplitter designed for visible light (CM1-BS013, Thorlabs Inc.). A 7 mm focal length protected silver reflective collimator (RC02APC-P01, Thorlabs Inc.) was used to minimize chromatic aberrations. The beam was scanned using a 2D galvanometric scanner. The scan and tube lenses were achromatic doublet pairs with 150 and 30 mm effective focal lengths, respectively, to achieve a beam diameter of 200 μm at the cornea to avoid aberrations. All sample arm lenses were matched with identical lenses in the reference arm and residual dispersion mismatch was numerically corrected post-processing. To ensure similar image quality between the OCT systems, transverse resolutions were approximately matched.

System specifications				
Wavelength (λ_0)	575 nm	860 nm	1060 nm	1325 nm
Scan lens focal length	150 mm	50.8 mm	50.8 mm	100 mm
Ocular lens focal length	30 mm	9.85 mm	9.85 mm	15 mm
Ocular lens diameter	1 inch	½ inch	½ inch	½ inch
Collimating lens focal length	7 mm	11 mm	11 mm	24 mm
Beam diameter at cornea ($1/e^2$)	250 µm	467 µm	464 µm	660 µm
Imaged Field-of-View	1.2 mm x 1.2 mm	2 mm x 2 mm	1.5 mm x 1.5 mm	2.25 mm x 2.25 mm
Fiber Type	SM450, Thorlabs	HI-780, Corning	HI-1060, Corning	SMF-28, Corning
Bandwidth (Δλ, FWHM)	110 nm	135 nm	110 nm	100 nm
Interferometer Type	Free-space	Fiber-based	Fiber-based	Fiber-based
Mode Field Diameter ($1/e^2$)	4.1 µm	5.0 µm	6.2 µm	9.2 µm
Transverse Resolution ($1/e^2$)	7.6 µm	6.1 µm	7.6 µm	6.6 µm
Axial Resolution in Air (FWHM)	1.7 µm	4.0 µm	7.5 µm	9.1 µm
Line Rate	10 kHz	125 kHz	100 kHz	91 kHz
Incident Power	300 µW	600 µW	1.5 mW	1 mW
Depth of field (FWHM)	439 µm	188 µm	235 µm	145 µm
6 dB roll-off	0.5 mm	0.8 mm	3 mm	2 mm
Refractive index of water	1.333	1.329	1.325	1.319

Table 1. System parameters for four custom systems for in vivo mouse retinal imaging. Note that it is impossible to simultaneously match effective numerical aperture, depth-of-field, and transverse resolution at all wavelengths. Here we opted to approximately match transverse resolution between the four systems. While bandwidths were similar across all four systems, axial resolution improved with decreasing wavelength due to the $\frac{\lambda_0^2}{\Delta\lambda}$ dependence of the coherence length.

2.2.2 Animal preparation and data acquisition

Experiments for the four spectral band comparisons were performed on 4-6 weeks old BALB/c (albino) and C57BL/6J (pigmented) mice (n=6 total) to investigate the effects of melanin on retinal reflectivity. Mice were initially anesthetized in a covered chamber ventilated with 2% isoflurane in a gas mixture of 80% air and 20% oxygen. The same mouse eye was imaged in vivo under isoflurane anesthesia on all systems within 24 hours. Tropicamide or phenylephrine were applied topically for pupil dilation, and goniosol was applied with a contact lens on the cornea to maintain hydration.

Additional experiments were performed on albino and pigmented mice (n=6 total) to investigate reflectance changes due to light adaptation and effects of pigmentation on image quality. Mice were dark adapted 30 minutes prior to those experiments in a covered container with water and food [56]. A 610 nm longpass filter (FGL610M, Thorlabs Inc.) was placed in the sample arm near the cornea to help with alignment using 10 μW which lasted less than 5 minutes to ensure minimal photopigment response. Various 2D repeated B-scan scanning protocols were performed with a transverse range of 300-1200 μm and an incident power of 300 μW. Reflectance were monitored throughout the retina, however only changes in and distal to the outer retina were found to be significant. All reflectance measurements were background corrected and normalized to the inner retinal reflectance (also background corrected) on a linear scale. A rolling average filter was applied to reduce reflectance fluctuations due to axial motion from breathing. Data was then normalized the baseline, to enable comparison between animals.

2.2.3 Enface image co-registration

Image co-registration between mouse retinas imaged at all four spectral bands is needed due to varying tissue morphology through the retinas. Superficial blood vessels were used as the landmarks and correlation was maximized using affine transformations. A small region of approximately 100 μm by 100 μm were co-registered between all four OCT volumes.

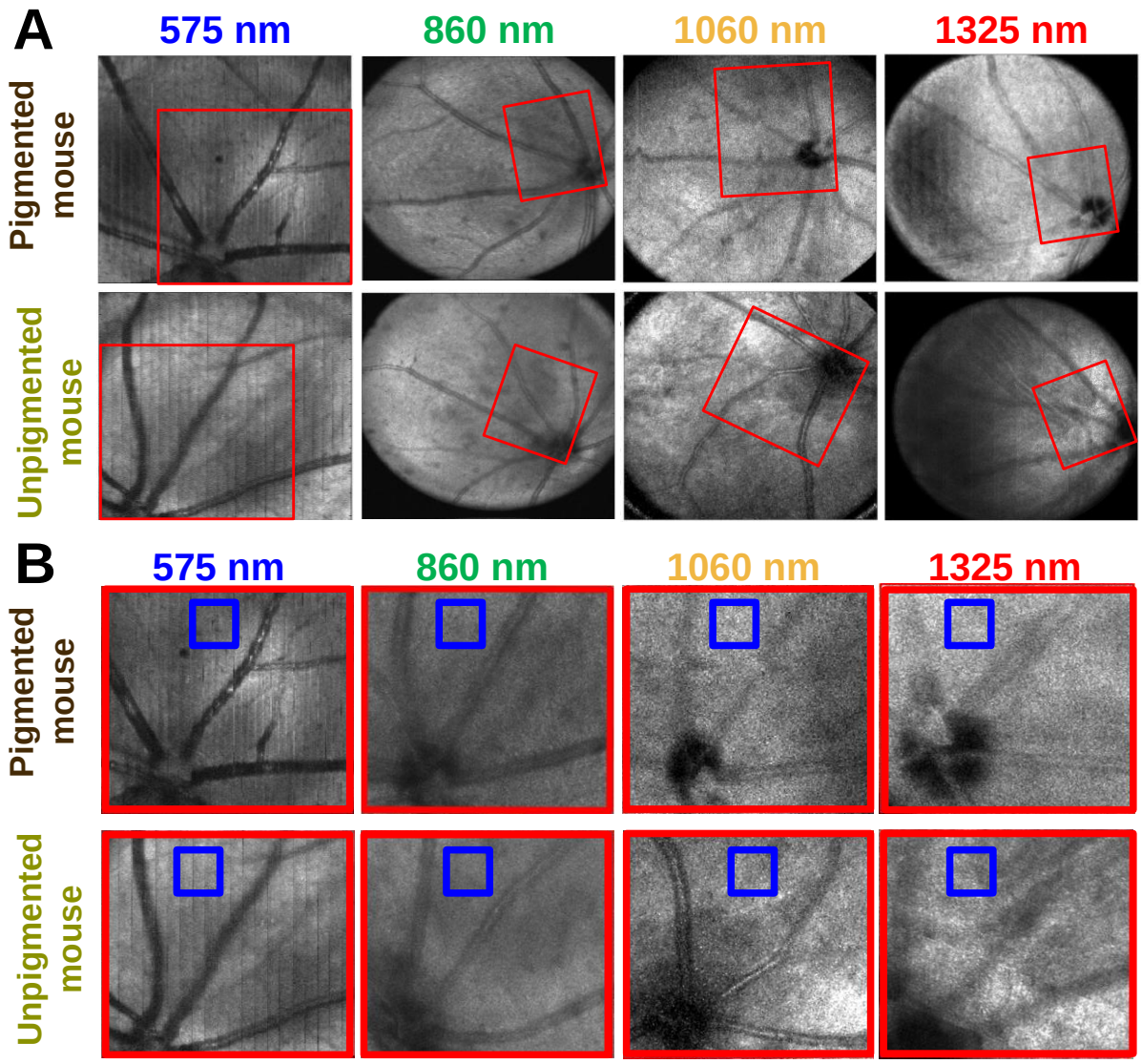

Figure 2. (A) En face images of the entire field-of-view for all systems, with the fast axis as the vertical axis and the slow axis as the horizontal axis. The red rectangular boxes shown within the en face images are corresponding fields-of-view. Note that the orientation of the red rectangular boxes is not identical between systems due to variable positioning of the mouse while imaging. (B) Magnified en face images of the red rectangular boxed regions shown in (A). Locations were scaled and orientated consistently. The blue box indicates the region from which line profiles in Figure 3 are taken.

2.3. Results

2.3.1 Four spectral band comparison

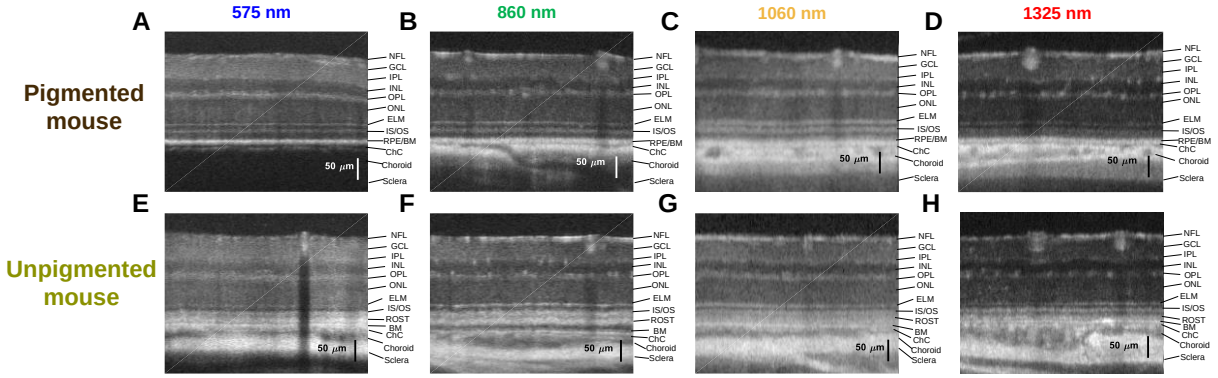

Figure 3. B-scan averaged OCT images of the pigmented (A-D) and albino (E-H) mouse retina acquired with 575 nm (A,E), 860 nm (B,F), 1060 nm (C,G), and 1325 nm (D,H) light. Note the increasing penetration with increasing wavelength for both pigmented and unpigmented mice. Nerve Fiber Layer (NFL), Ganglion Cell Layer (GCL), Inner Plexiform Layer (IPL), Inner Nuclear Layer (INL), Outer Plexiform Layer (OPL), Outer Nuclear Layer (ONL), External Limiting Membrane (ELM), Inner Segment/Outer Segment boundary (IS/OS), Rod Outer Segment Tips (ROST), Retinal Pigment Epithelium (RPE), Bruch's Membrane (BM), Choriocapillaris (ChC).

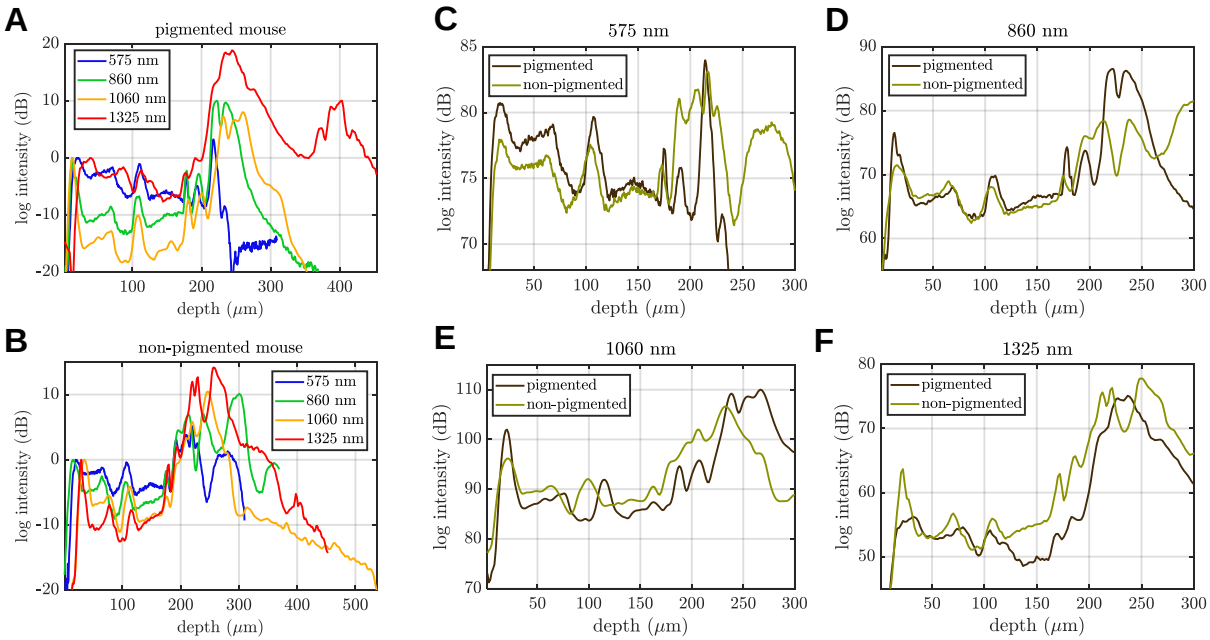

Figure 4. (A,B) Line profiles of pigmented and unpigmented mice at different wavelengths with linear background subtraction and normalization to the NFL. (C-F) Line profiles at 575 nm, 860 nm, 1060 nm, and 1325 nm of pigmented and unpigmented mice with linear background subtraction and normalization to integral over retinal depth.

The main differences in the OCT images between the albino and pigmented mice were seen in the RPE and choroid, due to melanin attenuation and scattering. Albino mouse OCT images have a hyporeflective RPE dark band, rendering the Bruch's membrane band more prominent. Albino mouse OCT images also have increased rod outer segment reflectivity. This may be due to lack of melanin absorption but differences in rod outer segment optical properties cannot be excluded. Overall, albino mouse OCT images have better penetration into the choroidal and sclera with better visibility seen at longer wavelengths.

Across the spectral bands, the inner retinal layers exhibit similar contrast implying spectrally independent reflectance. Signals from directional layers such as the internal and external limiting membrane exhibit angle dependence which introduce another source for reflectance variation that isn't intrinsic to the tissue. As expected, albino mice were shown to have increased penetration depth through the choroid and sclera for all wavelengths, indicating melanin to be the main contributor. Due to melanin's high absorption in the visible light range, we can clearly see a larger attenuation from choroidal melanin than RPE melanin based on the reflectance differences between the BM (distal to RPE) and sclera (distal to choroid). Pigmented mice have a higher penetration to the choroid and sclera with increased wavelengths, consistent with the current understanding of fundus reflectivity in OCT. Based on the penetration differences, we believe that water absorption does not play a significant role in penetration beyond the retina. For optimum penetration to the sclera without sacrificing theoretical axial resolution, the 1060 nm system seems to be the best choice.

Although the 1325 nm OCT images has the worst axial resolution, the choroid and sclera appear the sharpest in that spectral band. Melanin would have less scattering at longer wavelengths so it is possible that reduced multiple scattering may play a role. We also see sharper choroidal and scleral features in the albino mice compared to the pigmented mice which further validates the role of melanin multiple scattering in image sharpness beyond the retina.

2.3.2 Outer retinal reflectance changes seen in visible light OCT

Visible light Optical Coherence Tomography (OCT) has been demonstrated for ultrahigh resolution and molecular imaging of both the rodent [22, 57] and human retina [58]. Since visible light is absorbed by photopigment to initiate the phototransduction cascade, visible light OCT both stimulates and observes the retina simultaneously. This perturbation of retinal physiology presents both an opportunity and a challenge for visible light OCT. Visible light OCT has the potential to induce and observe bleaching-related absorption changes, as well as intrinsic scattering changes [59], swelling [53], and possible longer-term changes due to other fluorophores/chromophores [37]. Stabilized experimental animal preparations may help to understand the physiological origins of changes in the retina induced by visible light OCT, and also choose alignment and scanning protocols to avoid these during human imaging. Here we investigate changes in outer retinal reflectance during visible light OCT imaging in pigmented and albino mice and discuss the possible signal origins.

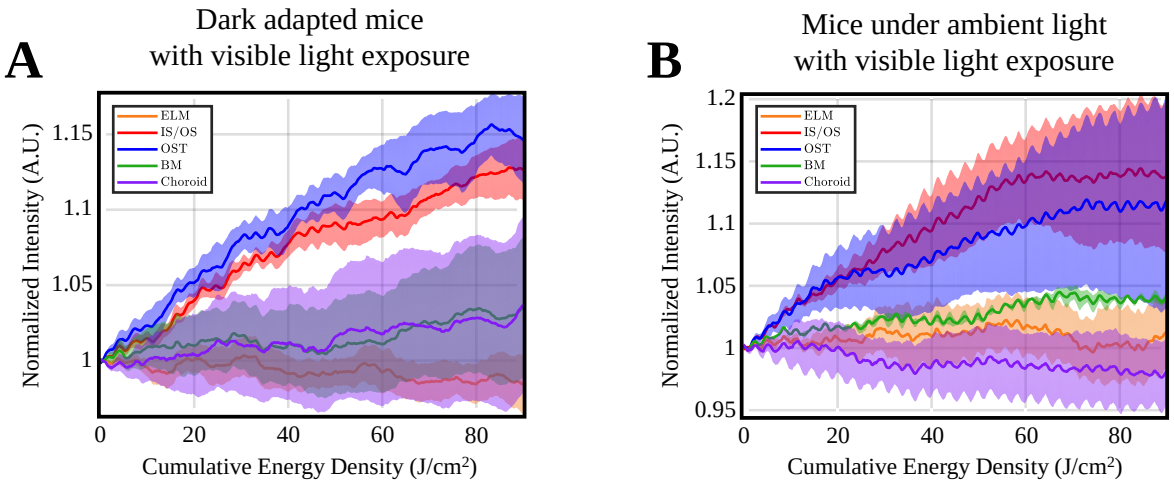

Figure 5. Outer retinal reflectance changes as a function of cumulative visible light energy density over the time scale of 30 seconds in dark adapted mice (A) and non-dark-adapted mice (B). Datasets were repeated b-scans in the same location.

When we observe changes in the outer retinal layers due to cumulative visible light exposure in repeated b-scans in Figure 5, we primarily see reflectance changes in the photoreceptor inner segment/outer segment (IS/OS) junction and the photoreceptor outer segment tips (OST), but no changes in the external limiting membrane (ELM), Bruch's membrane (BM), and choroid. There changes are seen in both dark adapted and

non-dark-adapted mice and the time scale of 30 seconds seem to be much larger than that of bleaching. We cannot completely rule out that these changes are due to bleaching and therefore have two hypotheses. Our transverse drift hypothesis says that there could be sample drift orthogonal to the b-scan which can partially expose unbleached photoreceptors leading to slower measured bleaching rate. Our Gaussian beam illumination hypothesis states that although the photoreceptors at the center of the Gaussian beam bleach quickly within the first scan, the photoreceptors at the edge of the beam are bleach much slower due to the lower power.

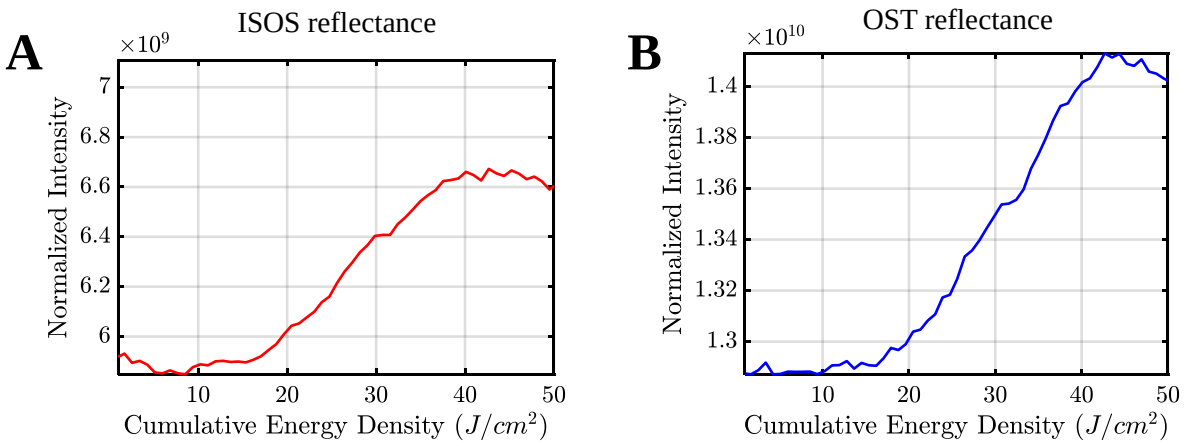

Figure 6. Outer retinal reflectance changes as a function of cumulative visible light energy density over the time scale of 30 seconds in the IS/OS junction layer (A) and the OST layer (B). Datasets were repeated 3D volumes in the same location.

We challenged these hypotheses by introducing a 3-scanning protocol that has repeated volumes instead of repeated b-scans to reduce the effects due to transverse drift and Gaussian beam illumination. We see similar changes in Figure 6 as Figure 5 so our hypotheses must be rejected.

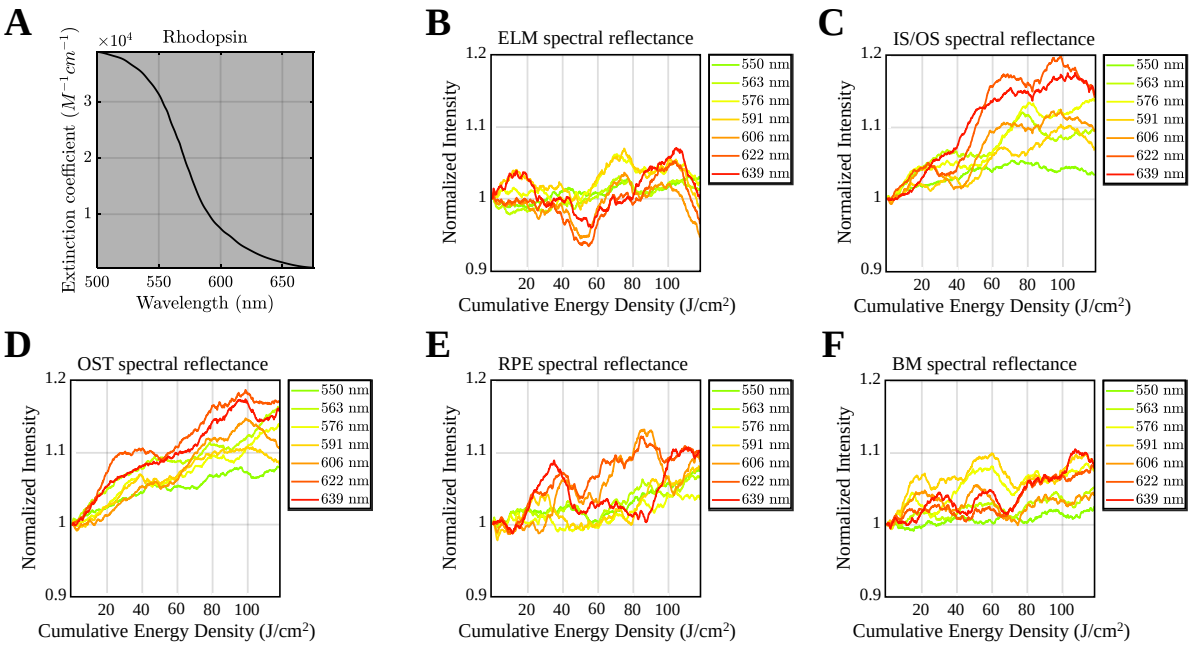

Figure 7. Rhodopsin extinction coefficients for the wavelengths in our imaging spectrum (A). Outer retinal reflectance changes as a function of cumulative visible light energy density for seven different spectral subbands in the visible light range for the ELM (B), IS/OS junction (C), OST (D), RPE (E), and the BM (F).

To further confirm that these outer reflectances changes are not due to bleaching, we investigated the changes as a function of visible light wavelength. By using the short-time Fourier transform (STFT), we produce the spectral subbands images at 7 different spectral bands. We observe that there are larger reflectance changes in the photoreceptor layers at longer wavelengths which goes against the expected spectral reflectance changes due to rhodopsin bleaching.

2.4. Conclusions

Different spectral bands, from visible to infrared, highlight different retinal layers in OCT. We discovered that the mouse inner retina has minimal spectral dependent reflectance changes. Due to the absence of melanin, we see better visibility of the RPE, choroid, and sclera in the unpigmented mouse. We also get better visibility and sharper images of the choroid and sclera at longer wavelengths due to less attenuation and less multiply scattered light. Although visible light OCT has better axial resolution, there are reflectance

changes in the photoreceptors that are not caused by photoreceptor bleaching, based on our experiments. These changes are not yet fully understood and visible light exposure needs to be better investigated. Our results aid fundamental understanding of OCT contrast mechanisms, and will help to select the optimal wavelength range for various OCT imaging applications, ranging from the inner and outer retina to the choroid.

Chapter 3: Spatially dependent dispersion correction in visible light OCT

3.1. Introduction

Visible light Optical Coherence Tomography (OCT) has recently emerged in retinal imaging, with claims of micron-scale axial resolution and multi-color (sub-band) imaging. Here, we show that the large dispersion of optical glass and aqueous media, together with broad optical bandwidths often used in visible light OCT, compromises both of these claims. To rectify this, we introduce the notion of spatially dependent (i.e. depth and transverse position dependent) dispersion. We use a novel sub-band, sub-image correlation algorithm to estimate spatially dependent dispersion in our 109 nm bandwidth visible light OCT mouse retinal imaging system centered at 587 nm. After carefully compensating spatially dependent dispersion, we achieve delineation of fine outer retinal bands in mouse strains of varying pigmentation. Spatially dependent dispersion correction is even more important for broader bandwidths and shorter visible light OCT wavelengths.

Recently, visible light Optical Coherence Tomography (OCT) has emerged for ultrahigh resolution and multi-color functional imaging in biological tissues [22, 23, 30]. In the retina, visible light OCT potentially offers micron-scale axial resolution and the intriguing ability to perform depth-resolved, multi-color retinal imaging with same wavelengths of light that initiate visual phototransduction. However, visible light OCT poses many technical challenges, such as limited exposures [37] and photon counts, high light scattering

and absorption [22], excess noise in light sources [60] and chromatic aberrations [23]. By addressing some of these challenges, recent research is beginning to realize the potential of visible light OCT [23].

3.2. Theory

In ray optics, dispersion refers to a variation in the refractive index of a material with wavelength. In OCT, as in ultrafast optics, chromatic dispersion typically refers to a nonlinear variation in the spectral phase delay versus optical frequency [61]. By either definition, dispersion is more severe for optical glass and aqueous media at visible wavelengths, as compared to near-infrared (NIR) wavelengths normally used for retinal OCT. Material dispersion is a root cause of chromatic aberration, which was previously assessed [26]. However, dispersion of the spectral phase has not been thoroughly analyzed in visible light OCT. To our knowledge, visible light OCT studies to date compensated depth-independent dispersion (DID) [26] using either physical or numerical means, or a combination thereof. In visible light OCT, depth dependent dispersion (DDD) has not been analyzed, though it has been considered at longer OCT wavelengths [62]. In this Letter, to fully manage dispersion in visible light OCT, we introduce the concept of spatially dependent dispersion, which includes both depth and transverse variation, the latter of which has not been previously treated. We present a novel, automated numerical approach, based on sub-band, sub-image correlation, to measure and correct spatially dependent dispersion. Our results show that micron-scale image resolution and accurate multi-color imaging with visible light OCT requires accounting for spatially dependent dispersion, and that disregarding it can severely compromise system performance.

To treat dispersion simply, we approximate the visible OCT wavefront as planar, neglecting curvature and the Gouy phase shift. For double-pass propagation through a material with length z, the spectral phase delay of a plane wave is given by

$$\phi(\omega, z) = 2k(\omega) \times z = 2\frac{\omega n(\omega)}{c} \times z\,, \qquad (2)$$

where $k(\omega)$ is the material propagation constant, $n(\omega)$ is the material refractive index (e.g., Figure 8A), ω is optical angular frequency, and c is the speed of light in free space. As described previously [61], $k(\omega)$ can be decomposed into a constant, linear, and nonlinear term, with subscripts "0", "L", and "NL" respectively, based on a Taylor series expansion at the center frequency, ω_0:

$$(\omega) = k_0 + k_L(\omega) + k_{NL}(\omega) = k_0 + \left.\frac{dk}{d\omega}\right|_{\omega_0}(\omega-\omega_0) + \sum_{m=2}^{\infty}\frac{1}{m!}\left.\frac{d^m k}{d\omega^m}\right|_{\omega_0}(\omega-\omega_0)^m . \quad (3)$$

The constant term in Eq. (3), with units of rad/μm, is the propagation constant at ω_0, related to the reciprocal of the phase velocity [$k_0 = k(\omega_0) = \omega_0 / v_{p,0}$]. The coefficient of the linear term, with units of fs/μm, is the reciprocal of the group velocity [$k'(\omega_0) = 1/v_{g,0}$]. The coefficient of the quadratic ($m = 2$) term, with units of fs^2/μm, is half the group velocity dispersion [$GVD/2 = k''(\omega_0)/2$].

GVD implies a change in group velocity with frequency, which causes group delay dispersion (GDD), after propagation through the material over a distance of $2z$ [$GDD = GVD \times 2z$]. GDD, with units of fs^2, resulting in temporal spreading of a short pulse with many wavelengths. Higher-order nonlinear terms ($m > 2$) also contribute to the degree of spreading. In OCT, the spectral phase *mismatch* between sample and reference arms, each containing materials with different lengths and propagation constants, comprises three terms, each corresponding with a term in Eq. (3):

$$\Delta\phi(\omega,\Delta z) = \Delta\phi_0(\Delta z) + \Delta\phi_L(\omega,\Delta z) + \Delta\phi_{NL}(\omega,\Delta z) . \quad (4)$$

Assuming henceforth that k in Eq. (3) applies to the sample propagation constant, we now study the depth-dependence of each term in Eq. (4). The constant phase term, $\Delta\phi_0(\Delta z) = \Delta\Phi_0 + 2k_0\Delta z$, comprises both a DI part ($\Delta\Phi_0$) and a DD part. By definition, the linear phase term, $\Delta\phi_L(\omega,\Delta z) = 2k_L(\omega)\Delta z = 2/v_{g,0}\times(\omega-\omega_0)\Delta z$, is DD. The dispersive nonlinear phase term,

$$\Delta\phi_{NL}(\omega,\Delta z) = \Delta\Phi_{NL}(\omega) + 2k_{NL}(\omega)\Delta z , \quad (5)$$

includes a DI part, with an assumed Taylor expansion of $\Delta\Phi_{NL}(\omega)=\sum_{m=2}^{\infty}a_m(\omega-\omega_0)^m$, and a DD part. The DI part arises from dispersive mismatch between the reference arm and sample arm at zero delay ($\Delta z=0$). Specifically, the $m=2$ term describes *GVD* mismatch. To understand DID and DDD, we consider the reconstruction of the OCT axial point spread function (PSF), neglecting mirror terms, for a point reflector at depth Δz,

$$s(\tau,\Delta z)=\Im^{-1}\left\{I(\omega-\omega_0)exp\left[i\Delta\phi(\omega,\Delta z)\right]\right\}=e^{i\Delta\phi_0(\Delta z)}\gamma(\tau-2\Delta z/v_{g,0})*\Im^{-1}\left\{e^{i\Delta\phi_{NL}(\omega,\Delta z)}\right\}. \quad (6)$$

where $\Im^{-1}$ represents an inverse Fourier transform with respect to $\omega-\omega_0$ to time lag, τ, and * denotes convolution in τ. $I(\omega-\omega_0)$ represents the interference spectrum amplitude, whose inverse Fourier transform, the mutual coherence function, $\gamma(\tau)=\Im^{-1}\left\{I(\omega-\omega_0)\right\}$, is the transform limited PSF, with no nonlinear phase and optimal resolution. Through the convolution in Eq. (6), the nonlinear phase $\Delta\phi_{NL}$ causes a broadening of the PSF. If both DID and DDD have the same sign, DID causes uniform broadening, irrespective of Δz, while DDD causes a broadening that depends on Δz. In most OCT systems, the depth-dependence of $\Delta\phi_{NL}$ can be neglected, i.e. $2k_{NL}(\omega)\Delta z\ll\pi$ for all ω and Δz of interest.

The effect of the linear phase in Eq. (4) is to shift the coherence function in Eq. (6) along the time lag axis to $\tau=2\Delta z/v_{g,0}$. The last essential step to consider is rescaling the PSF axis from time lag, τ, to axial position or depth, z_{img}, assuming a group velocity, $v_{g,img}$:

$$psf(z_{img},\Delta z)=s(\tau,\Delta z)\Big|_{\tau=2z_{img}/v_{g,img}}. \quad (7)$$

Note that $v_{g,img}$ need not necessarily equal v_g for the sample. For instance, $psf(z_{air},\Delta z)$, can be obtained by assuming $v_{g,img}=c$, or $\tau=2z_{air}/c$ in Eq. (7). Simulations (Figure 8), based on applying the above theory with $n(\omega)$ for water [9], clearly confirm that DDD degrades resolution in visible light OCT, even

for thin specimens such as the retina ($\Delta z \sim 200-300$ μm). To obtain a simple analytical expression that explains this unexpected finding, we next consider the expansion of $\Delta\phi_{NL}$ in Eq. (6) up to the GVD term, which dominates higher dispersion orders ($m > 2$) for aqueous media (Figure 8C) at visible wavelengths (Note that our ultimate correction procedure can incorporate higher dispersion orders).

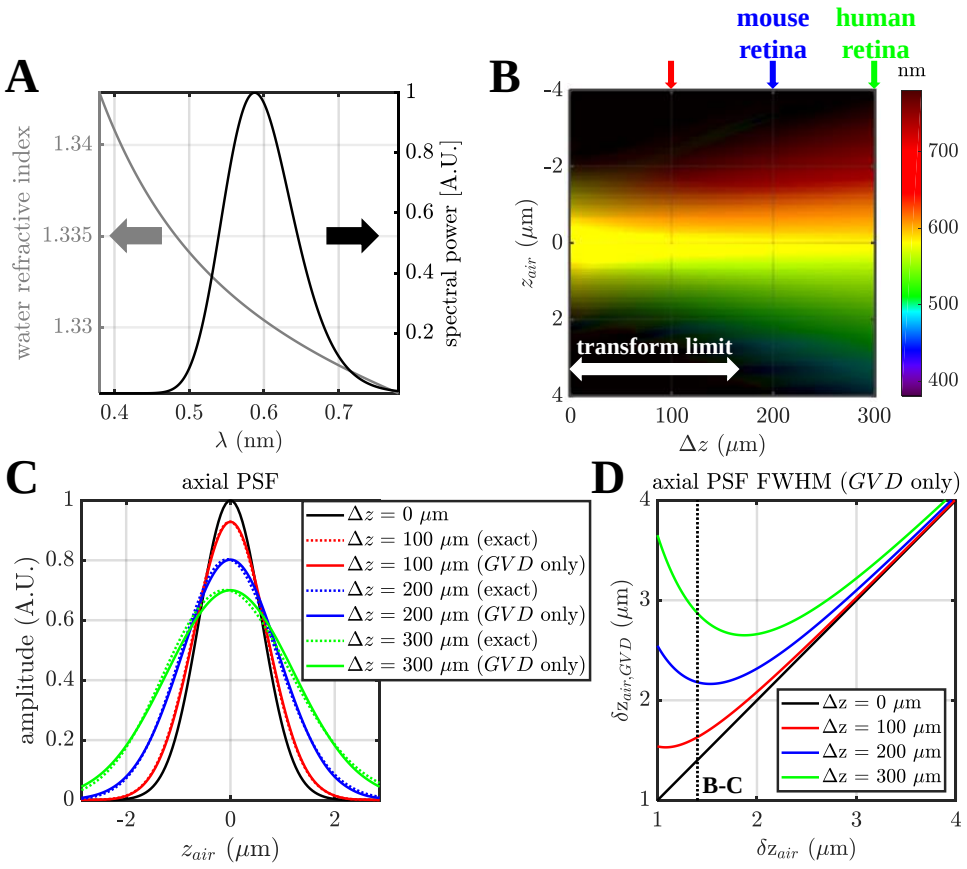

Figure 8. Simulations based on Eqs. (2)-(7) show the severity of depth dependent (DD) dispersion in our visible light OCT system (λ_0=587 nm, δλ=109 nm). A) Water refractive index and Gaussian spectrum versus wavelength. B) Simulated axial point spread function (PSF) broadens with increasing axial depth (Δz). The PSF phase slope is encoded as the visible color of the corresponding wavelength. C) The magnitude of the PSF (dotted lines) is well-predicted by group velocity dispersion (GVD) alone (solid lines), while higher dispersion orders induce PSF asymmetry. D) PSF broadening with depth [Eq. (8)] due to GVD (colored solid lines) increases as the transform limited resolution (solid black line) is improved. For our system parameters, water dispersion severely degrades resolution (dotted black line).

Considering just second-order (GVD) effects, we observe that: 1) GVD of aqueous media in the visible range is twice that in the NIR, exacerbating the effects of spatially dependent GDD [63]. 2) Practitioners

of visible light OCT typically use large optical frequency bandwidths ($\sim \delta\lambda / \lambda_0^2$) for spectroscopy or ultrahigh axial resolution. 3) The degradation of axial resolution by GDD worsens as the bandwidth increases (Figure 8D). Specifically, if $I(\omega - \omega_0)$ is Gaussian, an analytical formula for the GVD-degraded image resolution based on Eq. (6)-(7) is readily derived,

$$\delta z_{img,GVD} = \delta z_{img} \sqrt{1 + \frac{(2\log 2)^2 v_{g,img}^4 GDD^2}{\delta z_{img}^4}} \qquad (8)$$

where $\delta z_{img} = 2\log 2 \lambda_0^2 / (\pi n_{g,img} \delta\lambda)$ is the theoretical transform-limited resolution, in terms of the full-width-at-half-maximum (FWHM) wavelength bandwidth ($\delta\lambda$), group refractive index ($n_{g,img} = c / v_{g,img}$), and center wavelength ($\lambda_0 = 2\pi / k_0$). From Eq. (8) we can infer that GDD degrades resolution when $\delta z_{img,GVD} \geq \delta z_{img}\sqrt{2}$ or $\delta z_{img} \leq v_{g,img}\sqrt{2\log 2 \times GDD}$. If dispersion is matched at the internal limiting membrane (ILM) depth, since $\lambda_0 = 587$ nm and $GDD = GVD \times 2\Delta z$ where $GVD = 0.047$ fs^2/μm [63] and $\Delta z \sim 200\ (300)$ μm for the mouse (human) retina, we obtain from Eq. (8) the guideline that axial resolution is degraded at the posterior retina by GDD and DDD compensation is needed if $\delta\lambda \gtrsim 99$ (80) nm. Shorter central wavelengths result in higher GVD and even more stringent criteria. Thus, to summarize, in ultrahigh resolution OCT, if DID and DDD have the same sign, DID causes a DI resolution degradation, while DDD causes a DD resolution degradation that worsens with increasing Δz.

The effects of dispersion must also be considered in spectroscopic OCT, where the interference spectrum is divided into sub-bands. For instance, consider a sub-band with a center wavelength of $\omega_0 + \delta\omega_0$. Assuming again that sub-bands are narrow and the GVD term dominates higher order terms ($m > 2$), the main effect of dispersion is to modify the spectral phase slope in the sub-band. Performing all Taylor expansions about $\omega_0 + \delta\omega_0$ as opposed to ω_0, and considering the linear phase term yields a shift in the

apparent point spread function depth from Δz. to $\Delta z \times v_{g,0} / v_{g,s} + a_2 v_{g,0} \delta\omega_0$ where $v_{g,s}$ is the sub-band group velocity. Accounting for the rescaling operation in Eq. (6) with $v_{g,img} = v_{g,0}$ yields a depth-scaling of the sub-band image by $v_{g,0} / v_{g,s} \approx 1 + k''(\omega_0) v_{g,0} \delta\omega_0$ relative to the central sub-band, followed by a shift of the sub-band image by $\sim a_2 v_{g,0} \delta\omega_0$, where $\delta\omega_0 = \omega_s - \omega_0$ is the sub-band offset relative to the central frequency [64]. A positive GVD corresponds to a stretch of higher frequency sub-band images, since the actual group velocity is smaller than assumed in image reconstruction [Eq. (7)]. Thus, to summarize, in spectroscopic visible light OCT, DID causes a sub-band shift, while DDD causes a scaling (stretch or compression) of the sub-band depth axis.

3.3. Methods

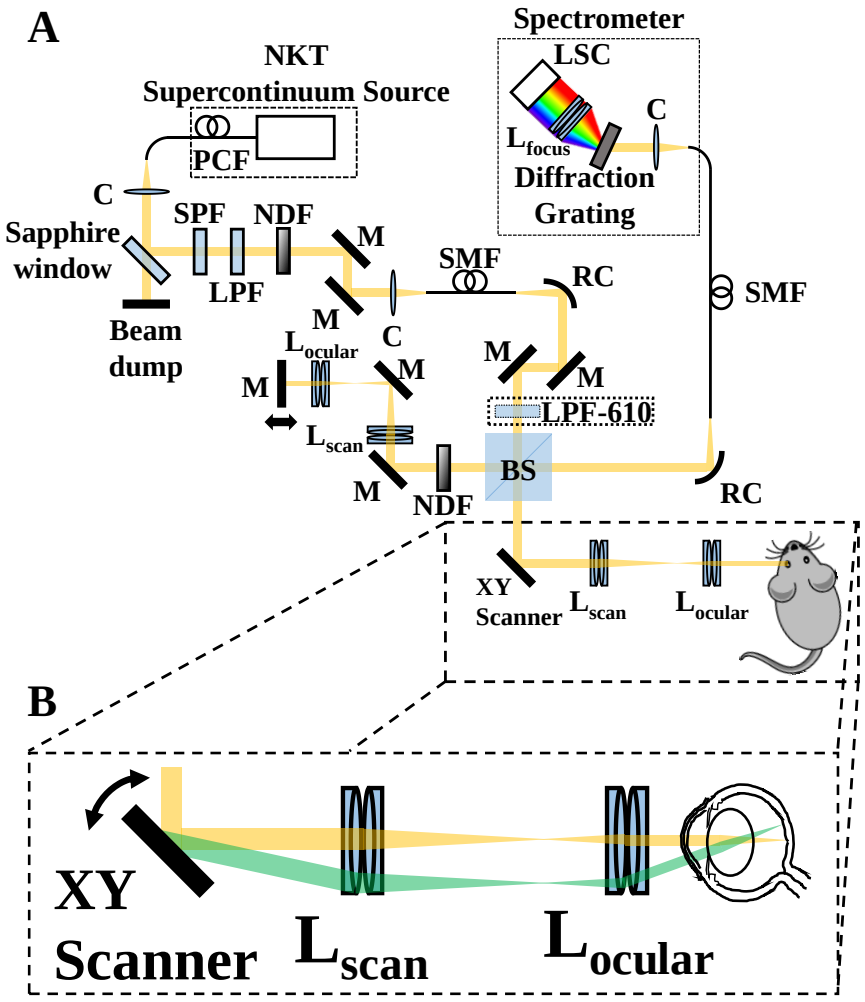

Figure 9. (A) Visible light OCT ophthalmoscope schematic. (B) Zoom shows differences in material traversed by the beam when scanning off axis (green), leading to transverse dependence of dispersion. (L: lens, SPF: short pass filter, LPF: long pass filter, NDF: neutral density filter, M: mirror, LSC: line scan camera, C: collimator, RC: reflective collimator, SMF: single mode fiber, BS: beam splitter, PCF: photonic crystal fiber, LPF-610: 610 nm long pass filter for alignment purposes).

A spectral / Fourier domain OCT ophthalmoscope for *in vivo* murine retinal imaging was built (Figure 9A) with a supercontinuum light source (EXW-12, NKT Photonics A/S, Denmark). The scan and tube lenses were achromatic doublet pairs with 150 and 30 mm effective focal lengths, respectively, to achieve a beam diameter of 200 μm at the cornea (effective NA=0.04) to mitigate aberrations. All sample arm lenses were matched with identical lenses in the reference arm. The spectrometer was calibrated using a previously

described procedure [29]. Our theoretical depth resolution in air (tissue) was 1.4 (1.0) μm. Imaging was performed with a 10 kHz line rate and 300 μW power at the cornea over a transverse angle of 26° with 350-700 axial scans. Due to the high visible light dispersion of common optical glasses, for which GVD is 2-3x larger than for NIR light, and aqueous media [63], discussed previously, as well as the fact that the OCT beam sees different material thicknesses as the beam is scanned (Figure 9B), we explicitly allow for the possibility that DID depends on transverse position [i.e. $a_m \to a_m(x)$ in the Taylor expansion of $\Delta\Phi_{NL}$]. Transverse and depth dependent dispersion, together, constitute spatially dependent dispersion.

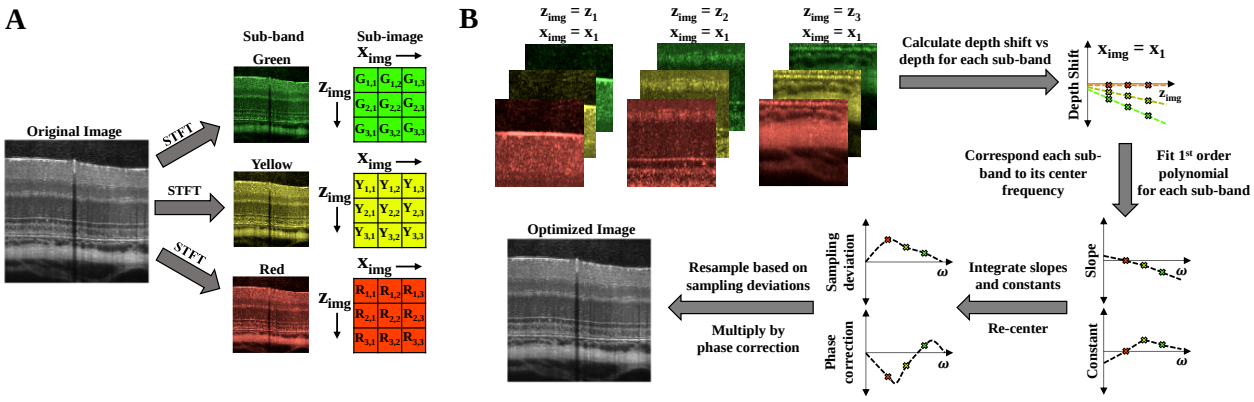

Figure 10. Correcting spatially-dependent dispersion using sub-band, sub-image correlation algorithm. A) Via Short Time Fourier Transform (STFT), original image is split into spectral sub-band images, which are further partitioned into sub-images. B) For each sub-image, each sub-band is correlated to a reference sub-band, resulting in a relative depth shift for each sub-band versus image depth. For each transverse position ($x_{img} = x_1$ shown) and sub-band, the shift with depth is fit by a 1st order polynomial with the y-intercept (constant) and first-order (slope) terms relating to depth-independent (DI) and depth-dependent (DD) dispersion, respectively. Assigning parameters to the center frequency for each sub-band and center transverse position for each sub-image, we can interpolate to find the constants and slopes for every frequency (ω) and transverse position. Integration of the slopes and constants yields the cumulative sampling deviation and phase correction. To avoid depth scaling or shifting of the image, a re-centering procedure is included. Correction is achieved by complex phase correction and resampling based on the sampling deviation.

The spectral phase of a specular reflection can be used to determine dispersion [62, 65]. However, specular reflections are not available at multiple spatial positions in an image. Here we take advantage of the laminar retinal structure, which yields distinct layers in sub-band sub-images (Figure 10). If dispersion is well-compensated, these layers must align in all sub-bands at all transverse positions and depths. Thus, we

divided the spectrum into 7 narrow sub-bands and 10-40 sub-images, over a grid of 5 transverse windows and 2-8 depth windows (Figure 10A). For each sub-image and sub-band, we calculated a depth shift relative to a reference sub-band (Figure 10B). The depth shift versus sub-image depth was fit with a first-order polynomial function. The slope corresponded to a scaling of the sub-image due to DDD, while the y-intercept corresponded to a shift due to DID. The slopes and y-intercepts were integrated versus frequency to yield functions for resampling and phase correction, respectively. After a compensation procedure based on phase correction (DID) [61] and resampling (DDD) [62], the sub-bands should overlap and coherently sum to form an ultrahigh resolution OCT image (Figure 10B). Note that DID varies between subjects due to eye length while DDD originates from the accumulation of dispersion within the imaging range (as well as possible spectrometer calibration error), which is more consistent across subjects.

3.4. Results

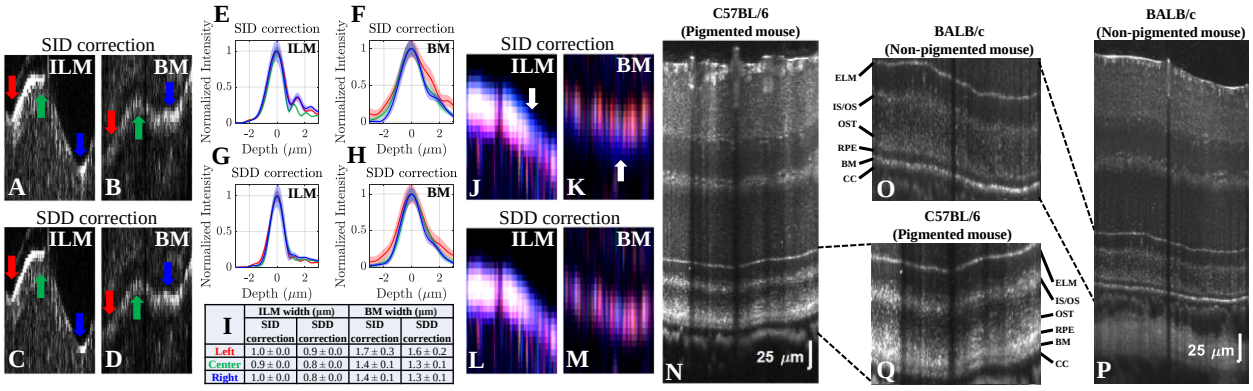

Figure 11. A-D) Zooms of visible light OCT images of the ILM and BM in a BALB/c mouse with SID (A,B) and SDD (C,D) correction. E-H) Axial intensity profiles of ILM and BM in different transverse regions denoted by the corresponding colored arrows (A-D), averaged across 100 images, with SID (E,F) and SDD (G,H) correction. Table I) The full-widths-at-half-maximum (mean ± std. dev.) of the axial profiles of the ILM and BM in (E-H) reduce with SDD correction. J-M) Zooms of spectroscopic RGB images ($\lambda_{0,blue} = 580\ nm, \lambda_{0,green} = 610\ nm, \lambda_{0,red} = 643\ nm$) of the ILM (J,L) and BM (K,M) with SID and SDD correction. With SID correction, note the blue "halo" (arrows) above the ILM and below the BM due to non-overlapping sub-bands (J,K). N,P) Averaged SDD corrected, spectrally shaped retinal images of C57BL/6 and BALB/c mice with outer retinal image zooms (O,Q). (ILM: Inner Limiting Membrane; ELM: External Limiting Membrane; IS/OS: Inner Segment/Outer Segment Junction; OST: Outer Segment Tips; RPE: Retinal Pigment Epithelium; BM: Bruch's Membrane; CC: Choriocapillaris; SID: spatially-independent dispersion; SDD: spatially-dependent dispersion).

To experimentally assess the improvement in image quality achieved by compensating spatially dependent dispersion (SDD), C57BL/6 and BALB/c mice were imaged in vivo (Figure 11) under isoflurane anesthesia, as approved by our Institutional Animal Care and Use Committee (IACUC). Different dispersion compensation methods were compared (Figure 11A-M) at the ILM and BM. With spatially-independent dispersion (SID) compensation to optimize overall image sharpness, spatial variation in group delay dispersion can shift different wavelengths in depth, even over modest axial image depths and fields-of-view of a few hundred microns (Figure 11J,K). Accounting for both transverse and depth dependent dispersion (Figure 11C,D,L,M), we made axial intensity profiles more uniform across transverse positions (Figure 11G,H) and reduced their widths (Figure 11I), enabling us to resolve thin retinal bands such as ILM and BM across entire images in both strains (Figure 11N-Q).

3.5. Conclusions

In conclusion, we have shown that spatially dependent dispersion can degrade performance of visible light OCT, even for apparently modest sample thicknesses of a few hundred μm and wavelength bandwidths of ~100 nm. Based on the observation that depth-independent and depth dependent dispersion shift and depth scale sub-band images, respectively, we introduced a sub-band, sub-image correlation approach to estimate dispersion parameters. Upon correction of spatially dependent dispersion, we resolved fine layers such as the BM and ILM in both non-pigmented and pigmented mice across the entire imaged field-of-view. Our correction method also promises to improve accuracy of spectroscopic visible light OCT.

Chapter 4: Supercontinuum excess noise can calibrate OCT spectrometers

4.1. Introduction

Across optics and photonics, excess intensity noise is often considered a liability. Here, we show that excess noise in broadband supercontinuum and superluminescent diode light sources encodes each spectral

channel with unique intensity fluctuations, which actually serve a useful purpose. Specifically, we report that excess noise correlations can both characterize the spectral resolution of spectrometers and enable cross-calibration of their wavelengths across a broad bandwidth. Relative to previous methods that use broadband interferometry and narrow linewidth lasers to characterize and calibrate spectrometers, our approach is simple, comprehensive, and rapid enough to be deployed during spectrometer alignment. First, we employ this approach to aid alignment and reduce the depth-dependent degradation of the sensitivity and axial resolution in a spectrometer-based optical coherence tomography (OCT) system, revealing a new outer retinal band. Second, we achieve a pixel-to-pixel correspondence between two otherwise disparate spectrometers, enabling a robust comparison of their respective measurements. Thus, excess intensity noise has useful applications in optics and photonics.

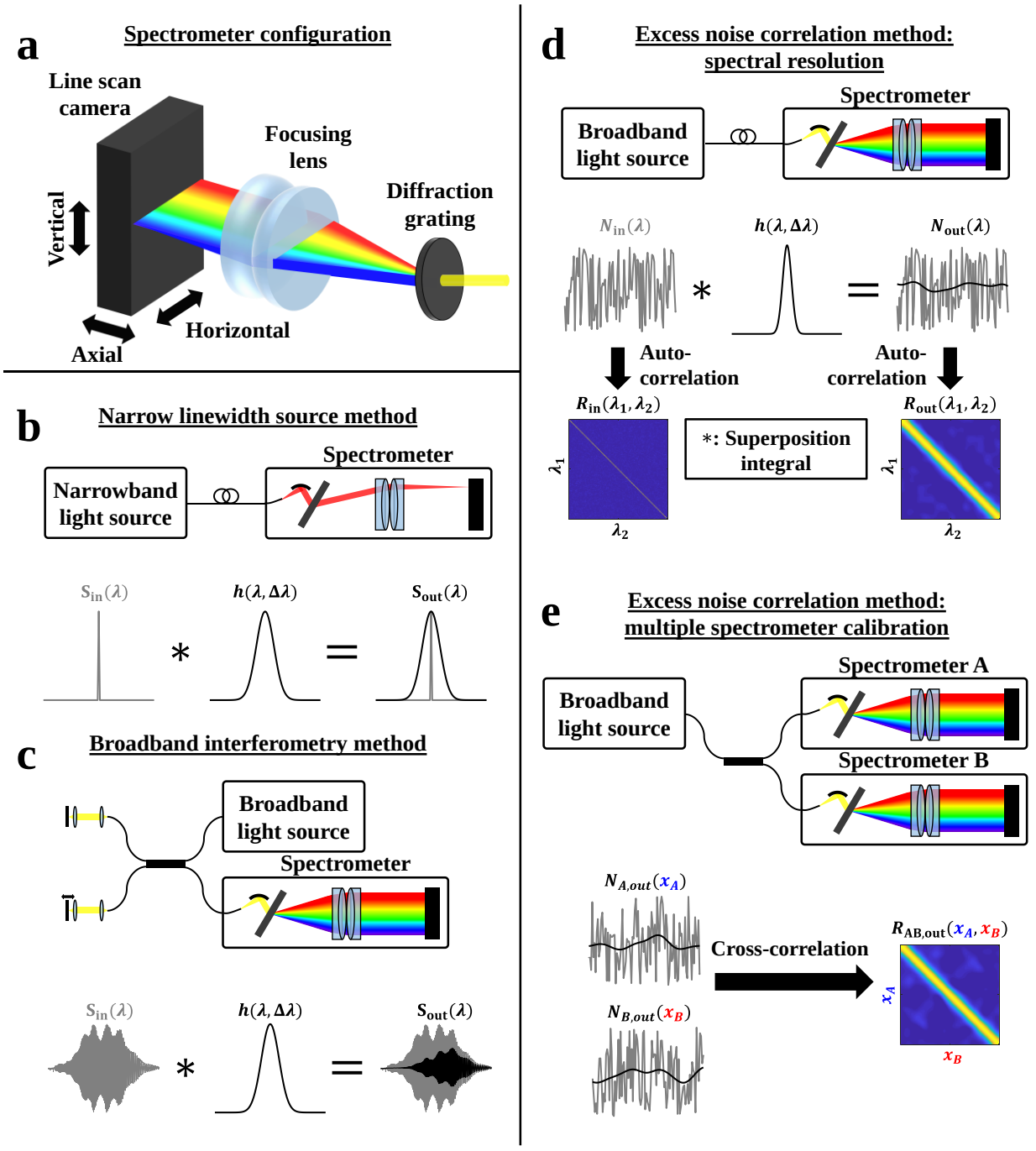

Figure 12. Spectrometer characterization and calibration methods. a Typical spectrometer. Collimated light is spectrally dispersed by the diffraction grating and focused onto a linear sensor. b The narrow linewidth source method requires a narrowband light source for each wavelength to be assessed (top). The measured spectrum output, $S_{out}(\lambda)$, is the superposition integral of the true spectrum input, $S_{in}(\lambda)$, and the spectrometer impulse response, $h(\lambda,\Delta\lambda)$: $S_{out}(\lambda)=\int S_{in}(\Lambda)h(\Lambda,\lambda-\Lambda)d\Lambda$. If the input

approximates a delta function, then the output, $S_{out}(\lambda)$, resembles $h(\lambda, \Delta\lambda)$ (bottom). c The broadband interferometry method requires an auxiliary interferometer to create an oscillating interferometric input, $S_{in}(\lambda)$ (top). The spectrometer reduces the oscillations in the output, $S_{out}(\lambda)$, depending on the impulse response (bottom). See Section 4.2 for a complete description. d In the proposed excess noise method for characterization, an appropriate broadband light source is required (top). The output, $N_{out}(\lambda)$, is the superposition integral of the excess noise input, $N_{in}(\lambda)$, and $h(\lambda, \Delta\lambda)$. For white noise input, the input autocorrelation matrix, $R_{in}(\lambda_1, \lambda_2)$, is diagonal. The output autocorrelation matrix, $R_{out}(\lambda_1, \lambda_2)$, is quasi-diagonal, with broadening depending on the local impulse response (bottom). e In the related method for cross-calibration, an appropriate broadband light source and a coupler are required (top). The excess noise outputs from spectrometers A and B, $N_{A,out}(x_A)$ and $N_{B,out}(x_B)$, respectively, are cross-correlated to yield $R_{AB,out}(x_A, x_B)$, where the highest correlation values occur for pixels that measure similar wavelengths (bottom).

Optical spectrometers, which measure light intensity on a wavelength-by-wavelength basis, benefit many fields, including biomedical science [66-68], agriculture [69], and security [70]. Spectral resolution refers to the ability of a spectrometer to distinguish fine spectral features. In a common spectrometer design that disperses light across a detector array (Figure 12a), the spectral resolution is ideally determined by the equivalent spectral widths of the sensor pixels and dispersive element resolution [71, 72]. Pixel cross-talk and optical aberrations, including those caused by misalignment of refractive elements, reflective elements, diffractive elements, and the sensor, all degrade the spectral resolution (see Section 4.3.1 for a more complete discussion of spectrometer performance). While simulations can determine idealized positioning of optical components, in practice, optimal placement of components a priori is difficult given manufacturing tolerances, and alignment is still required (see Section 4.3.2). Feedback on the spectral resolution across the entire spectrometer during alignment is highly desirable but currently impractical, as described below. Moreover, for homebuilt and commercial spectrometers with varying specifications, cross-calibration of wavelengths is needed to compare spectral features, such as Raman peaks, which relate to the chemical composition [68]. The alignment and specifications may change as spectrometers experience wear-and-tear. Overall, to improve the rigor and reproducibility of research that uses

spectrometers, we identify two unmet needs: first, rapid and comprehensive characterization of the spectrometer resolution, and second, pixel-by-pixel calibration of spectrometer wavelengths. Current approaches for spectrometer characterization and calibration [73] are slow, cumbersome, or limited in spectral range.

To provide an approach to address these problems, we turn to a somewhat unexpected phenomenon: the excess noise in broadband light sources [60, 74-76]. "Excess" refers to noise in excess of fundamental quantum shot noise. Interestingly, in photonics applications described heretofore, excess noise degraded the performance. We show that, rather than being a liability, excess noise imbues broadband light with high-resolution spectral encoding (see section 4.5.1), which is a natural conduit for spectrometer characterization and cross-calibration. Based on this insight, we develop a simple strategy to characterize the spectral resolution of spectrometers. We also develop an approach to create a precise mapping between pixels of two different spectrometers that correspond in wavelength, hereafter referred to as cross-calibration. We validate our approach against conventional methods across multiple spectral ranges, showing its broad applicability to both supercontinuum and superluminescent diode light sources. We then demonstrate its utility by improving the spectral resolution of multiple visible light optical coherence tomography (OCT) spectrometers and visualizing a new band in the mouse outer retina. Next, we demonstrate cross-calibration of two otherwise disparate spectrometers with high accuracy. Thus, our method for spectrometer characterization and cross-calibration represents a unique application of excess noise.

4.1.1 Origins of incoherent excess noise

Beyond the experimental data presented in this work, theoretical arguments support that pure spontaneous emission sources exhibit incoherent excess noise, uncorrelated at optical frequencies spaced much greater than the inverse integration time. The predominant expression for excess noise in the literature [77-79] for a single mode, thermal source with Gaussian field statistics assumes excess intensity fluctuations result from the addition of independent temporal cells. The cell number (N) is given by the ratio of the detector

integration time to the coherence time [80], i.e. $N = T/\tau_c$, leading to $1/N$ scaling of the excess noise coefficient. Equivalently, the number of independent cells is proportional to the ratio of the optical linewidth to the detection bandwidth [81]. If the effective optical linewidth is equated to the spectrometer spectral resolution, this theory implies negligible intrinsic correlation length, i.e. incoherent excess noise. How well do amplified spontaneous emission sources obey the incoherent excess noise assumption, particularly in the presence of gain saturation that could introduce correlations between wavelengths? While further work is needed, experimental measurements [79] suggest that, with an empirical factor to account for noise suppression, the predicted inverse linewidth scaling of excess noise is indeed observed for superluminescent diodes (SLDs).

For supercontinuum sources, the intrinsic correlation length is complex and critically depends on the nonlinear processes involved in spectral broadening [82-84]. For broad supercontinuum generation in a photonic crystal fiber, the degree to which modulation instability is seeded coherently (e.g. by a short pulse) versus by noise on the input pulse is a key determinant of final coherence [82]. Notably, in a low noise 1700 nm source based on self-phase modulation, incoherent excess noise was not detected (Figure 22f). However, for photonic crystal fiber-based broadband supercontinuua, a sufficiently incoherent excess noise component was inferred both at 1600-1800 nm (Figure 22d,e) and at visible wavelengths (e.g., Figure 20 and Figure 23a). A fitting procedure to exclude broader intrinsic spectral correlations and isolate this component (Figure 20 and section 4.5.1) enabled accurate determination of spectral resolution.

4.2. Current methods

4.2.1 Impulse response function method

Assessing the spectral resolution, or spectrometer characterization, essentially reduces to system identification [72, 73]. Two methods are currently used [73]. The first, the impulse response method, determines the spectral resolution from the measured intensity pattern of a narrow linewidth light source or sharp spectral feature, ideally with a lineshape much narrower than the spectral resolution (Figure 12b).

However, this approach requires additional narrow linewidth sources, narrowband optical filters, or sources with fine spectral features (e.g., Fraunhofer lines or frequency combs). For a comprehensive characterization, fine spectral features are required at each measured wavelength. While a tunable, narrow linewidth source could provide a universal approach, such sources are not available for all wavelength ranges (e.g., visible).

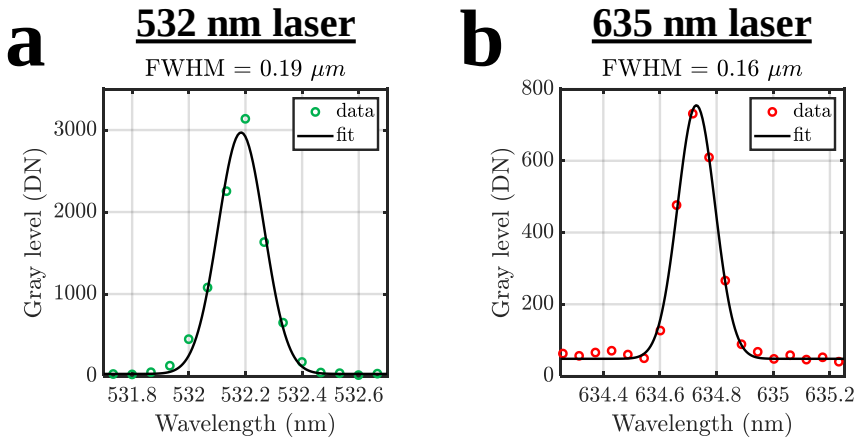

Figure 13. Narrowband laser method for spectral resolution. Gaussian fitting of the measured green (~532 nm) (a) and red (~635 nm) (b) laser spectra to obtain the spectral resolution.

The spectral resolution determined from the proposed excess noise method was validated against two well-accepted methods (Figure 21b): narrowband lasers and broadband interferometry [71-73]. For the narrowband laser method, if the laser linewidth is significantly narrower than the spectral resolution, the FWHM of the spectral intensity distribution measured by the spectrometer is the spectral resolution (Figure 13). Note that even if the laser width is comparable to the spectral resolution, the spectral resolution is still obtainable if the laser lineshape is known. Here, the lineshape was assumed to approximate a delta function.

Similarly, for the related problem of assigning pixels to wavelengths, or spectrometer calibration, current approaches utilize either fine optical features, such as narrowband lasers or spectral lines with well-known and invariant wavelengths, or interferometry [85, 86]. If the spectrometer is previously calibrated at one or more pixels, then broadband interferometry with highly accurate path length variations can be used to

calibrate the remainder [29, 87]. Otherwise, a tunable narrow linewidth source is required at all wavelengths. Thus, a simple method for pixel-by-pixel spectrometer characterization and calibration remains elusive.

4.2.2 Transfer function method

The second, the transfer function method, determines the spectral resolution across wavelengths from the attenuation of a sinusoidal interference fringe pattern envelope as the path length mismatch increases (Figure 12c). This method can yield the spectral resolution for every sensor pixel, but only if the spectral resolution is slowly varying across the sensor. Data acquisition can be time consuming, requiring multiple measurements with an external, variable path length interferometer. Thus, neither of the two existing characterization methods are practical during spectrometer alignment.

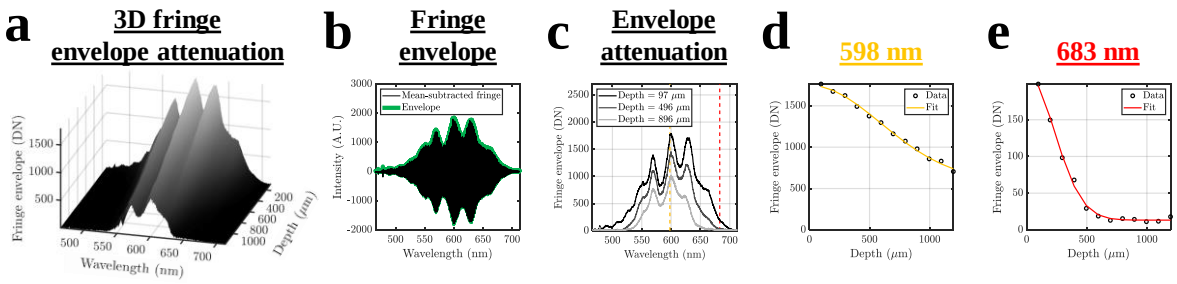

Figure 14. Interferometry method for spectral resolution. a Interference fringe envelope versus wavelength and depth (path length mismatch divided by two). To highlight the effects of wavelength-variant spectral resolution, the original, sub-optimal configuration of spectrometer A (Figure 25a) was used. b The interference fringe and its envelope at a depth of 97 μm. c Fringe envelope, as a function of wavelength, is shown at various depths with the colored dotted lines showing wavelengths in d and e. Fringe envelope attenuation with depth is shown at λ = 598 nm (d) and λ = 683 nm (e).

For the broadband interferometry method, the attenuation of the interference fringe envelope with increasing spectral oscillation rate (path length) is caused by the finite spectral distribution measured by each pixel. Multiple datasets at different path length mismatches were acquired to obtain the attenuation of the fringe envelope with depth (path length divided by two), for each pixel or wavelength in the spectrum (Figure 14a-c). For each pixel/wavelength (Figure 14d-e), we fit a Gaussian function to the interference

fringe attenuation versus depth, whose FWHM width, $\Delta z(\lambda)$, is the axial resolution for optical coherence tomography (OCT), at that corresponding pixel/wavelength. Since the spectral resolution can also be viewed as the spectral bandwidth at a given pixel, we can derive the spectral resolution from $\Delta z(\lambda)$ using the OCT axial resolution equation [88]:

$$FWHM_h(\lambda) = \frac{2ln2}{\pi}\frac{\lambda^2}{\Delta z(\lambda)} \tag{9}$$

where $FWHM_h(\lambda)$ is the spectral resolution and λ is the center wavelength at the given pixel.

4.3. Simulations

4.3.1 Spectral resolution theoretical limit and impulse response shape

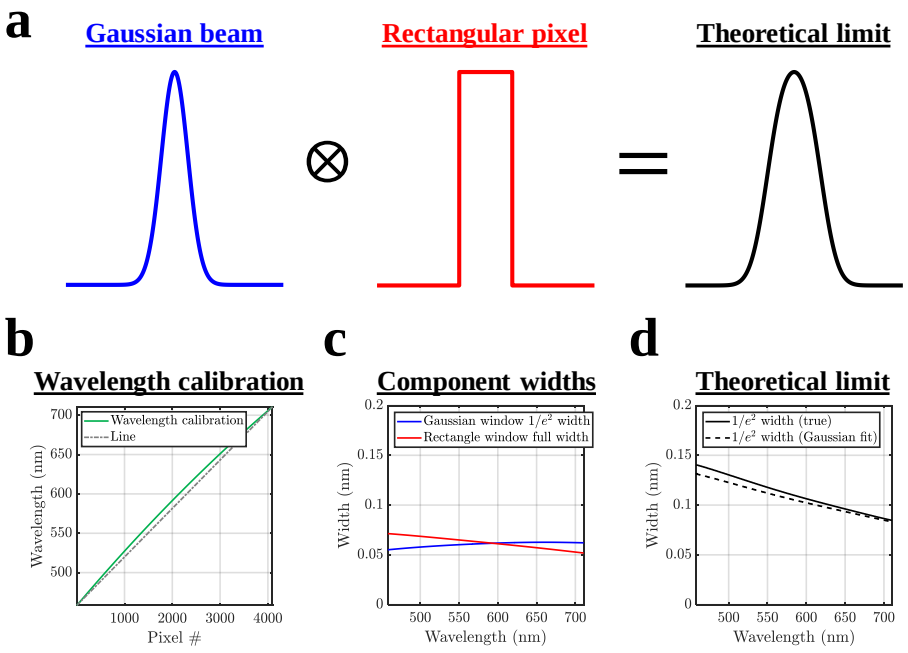

Figure 15. Theoretical limit of spectral resolution. a The theoretical impulse response that yields the spectral resolution limit (black) is obtained through the local convolution, denoted by "⊗", of the transverse Gaussian beam on the camera sensor (blue) with the rectangular width of the sensor pixel (red). b Wavelength versus sensor pixel. Note that the wavelength is not linear with pixel number. c The spectral

widths of the Gaussian beam (blue) and the rectangular pixel (red) for every wavelength in the spectrum. d The true width of the theoretical impulse response limit is similar to the fitted Gaussian width for all wavelengths.

Not accounting for aberrations and pixel cross-talk, we assume that the theoretical spectral resolution of a spectrometer is given by the local convolution of the transverse Gaussian beam on the sensor with the rectangular pixel [71, 72] (Figure 15a). Given the estimated mode field diameter at all wavelengths and the focal lengths of the collimator and focusing lens in Spectrometer A, we calculate the wavelength-dependent Gaussian spot size on the sensor. Both the Gaussian and rectangular window widths (Figure 15c) are converted to spectral widths, according to our wavelength calibration[57] (Figure 15b), and are locally convolved to obtain the spectral resolution theoretical limit (Figure 15d). This simulation does not account for chromatic aberrations or the change in refractive index of the core and cladding with wavelength, which changes the numerical aperture. The $\frac{1}{e^2}$ width of a fitted Gaussian is comparable to the true $\frac{1}{e^2}$ width of the theoretical limit (Figure 15d). Given the small error of the width determined by Gaussian fitting, we conclude that Gaussian fitting can correctly infer the spectral resolution from the impulse response, and by extension, the excess noise autocorrelation matrix.

4.3.2 Ray tracing to predict spectrometer performance

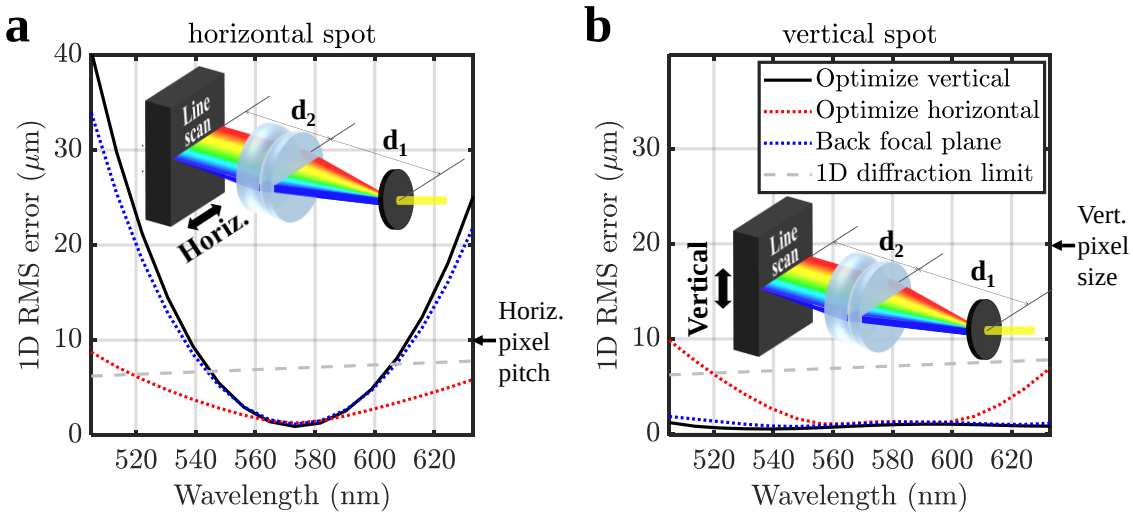

Figure 16. Horizontal (a) and vertical (b) one-dimensional (1D) root-mean-squared (RMS) spot sizes at the sensor, based on ray tracing, explain the performance improvement observed in Figure 27a. Ray tracing was performed in OpticStudio (Zemax, LLC) with variable d_1, d_2, and sensor horizontal tilt, with a 9.5 mm pupil to optimize either the vertical direction (black line) or the horizontal direction (dotted red line). A standard back focal plane configuration is also shown for comparison (dotted blue line). Optimizing the vertical direction yields a poor horizontal 1D RMS error (black in a), hence poor spectral resolution, towards the edges of the spectrum. On the other hand, optimizing the horizontal direction improves the horizontal 1D RMS error (dotted red line in a) to near the 1D diffraction limit (dashed gray line in a) and below the horizontal pixel pitch (arrow in a), without degrading the vertical 1D RMS error (dotted red line in b) significantly relative to the vertical pixel size (arrow in b). Even accounting for diffraction effects (dashed gray line in b), we suggest that horizontal optimization does not incur significant loss of light compared to vertical optimization, as both the vertical 1D RMS error and diffraction limit remain less than half the vertical pixel size (b). Optimal distances in simulation were d_1 = 139.9 mm and d_2 = 118.8 mm for vertical optimization (black), d_1 = 72.0 mm and d_2 = 118.8 mm for horizontal optimization (dotted red), and d_1 = 118.8 mm and d_2 = 118.8 mm for the back focal plane configuration (dotted blue). The diffraction limit was estimated from the spectrometer magnification of 2.4, assuming a fibre mode field diameter of 3.5 microns at 488 nm.

We performed ray tracing (Figure 16) of the spectrometer later characterized in Section 4.6.7 (spectrometer B) to better understand the origins of the experimentally observed improvements in performance. Simulations were performed to optimize either the vertical direction, and thus intensity (black line), or the horizontal direction, and thus spectral resolution (dotted red line). Individually optimized configurations were compared against the back focal plane configuration, where the grating is placed in the back focal plane of the lens (dotted blue line). Optimization of the vertical direction resulted in poor performance along the horizontal direction (Figure 16a), as measured by the one-dimensional (1D) root-mean-squared (RMS) error. On the other hand, it was possible to significantly improve the horizontal RMS error (Figure 16a) without degrading the vertical RMS error (Figure 16b) enough to significantly impact performance. This is due in part to the vertical pixel size of 20 microns (arrow in Figure 16b), which is tolerant to vertical aberrations. These simulations justify our experimental approach of choosing the lens-to-grating distance to optimize the spectral resolution (horizontal direction), as this configuration also achieves near-optimal intensity.

Note that while spectrometer optimization driven by ray tracing provides insight into the improved performance, simulations cannot substitute for experimental measurements of spectral resolution. For

instance: 1) Tolerances for the fiber mode field diameter and numerical aperture at visible wavelengths are on the order of 15%, leading experimental uncertainty. 2) Pixel cross-talk, which increases the effective sensor pixel size, is wavelength dependent and challenging to measure and model. 3) Manufacturing tolerances necessitate some form of mechanical adjustment, particularly for homebuilt spectrometers.

4.4. Theory

4.4.1 Spectral resolution characterization with excess noise correlations

We assume that the spectrometer is a linear, but not necessarily wavelength shift-invariant, system such that $N_{out}(\lambda) = \int N_{in}(\Lambda) h(\Lambda, \lambda - \Lambda) d\Lambda$, where $N_{out}(\lambda)$ and $N_{in}(\lambda)$ are the measured and intrinsic source excess noise, respectively, as a function of wavelength (λ). In this shift-variant linear system, $N_{out}(\lambda)$ is the superposition integral of $N_{in}(\lambda)$ and $h(\lambda, \Delta\lambda)$. The spectrometer impulse response function, $h(\lambda, \Delta\lambda)$, is a function of λ, the input wavelength, and $\Delta\lambda$, the difference between the measured and input wavelengths. The first argument allows the impulse response to vary with wavelength. As $h(\lambda, \Delta\lambda)$ is a possible spectral intensity distribution (Figure 12b), it must be nonnegative. Our proposed method utilizes the correlation of the excess noise, $R_{out}(\lambda_1, \lambda_2)$, between pairs of measured wavelengths, λ_1 and λ_2, to infer $h(\lambda, \Delta\lambda)$ and extract its width in $\Delta\lambda$, known as the spectral resolution. The input (true) and output (measured) excess noise correlations are

$$R_{in}(\lambda_1, \lambda_2) = \langle N_{in}(\lambda_1) N_{in}(\lambda_2) \rangle \text{ and} \tag{10}$$

$$R_{out}(\lambda_1, \lambda_2) = \langle N_{out}(\lambda_1) N_{out}(\lambda_2) \rangle, \tag{11}$$

respectively, where N_{in} is the zero-mean input excess noise and N_{out} is the zero-mean output excess noise. We take $\langle \bullet \rangle$ to denote the ensemble average, which is estimated here by time averaging. All quantities are assumed to be real. Using the linear system assumption described above, Eq. (11) takes the form

$$R_{out}(\lambda_1, \lambda_2) = \left\langle \int N_{in}(\Lambda_1) h(\Lambda_1, \lambda_1 - \Lambda_1) d\Lambda_1 \int N_{in}(\Lambda_2) h(\Lambda_2, \lambda_2 - \Lambda_2) d\Lambda_2 \right\rangle \quad (12)$$

We can then substitute Eq. (10) into Eq. (12), using the fact that h is invariant, to obtain $R_{out}(\lambda_1, \lambda_2)$ in terms of $R_{in}(\lambda_1, \lambda_2)$:

$$R_{out}(\lambda_1, \lambda_2) = \iint R_{in}(\Lambda_1, \Lambda_2) h(\Lambda_1, \lambda_1 - \Lambda_1) d\Lambda_1 h(\Lambda_2, \lambda_2 - \Lambda_2) d\Lambda_2 \quad (13)$$

Assuming that the excess noise is white, we can express $R_{in}(\lambda_1, \lambda_2)$ as a delta function, $\delta(\lambda_2 - \lambda_1)$. Thus,

$$R_{in}(\lambda_1, \lambda_2) = \sigma^2(\lambda_1) \delta(\lambda_2 - \lambda_1) \quad (14)$$

where $\sigma^2(\lambda)$ is the wavelength-dependent variance. In cases where the white noise assumption is invalid [75], the above expression can be modified to accommodate a nonimpulsive R_{in} (see Section 4.4.3). Substituting Eq. (14) into Eq. (13) yields

$$R_{out}(\lambda_1, \lambda_2) = \int \sigma^2(\Lambda_1) h(\Lambda_1, \lambda_1 - \Lambda_1) h(\Lambda_1, \lambda_2 - \Lambda_1) d\Lambda_1 \quad (15)$$

Assuming that $\sigma^2(\lambda)$ varies slowly on the scale of the spectral resolution, we can remove it from the integral:

$$R_{out}(\lambda_1, \lambda_2) = \sigma^2\left(\frac{\lambda_1 + \lambda_2}{2}\right) \int h(\Lambda_1, \lambda_1 - \Lambda_1) h(\Lambda_1, \lambda_2 - \Lambda_1) d\Lambda_1 \quad (16)$$

We can further simplify Eq. (16) by using the substitutions $\Lambda' = \lambda_1 - \Lambda_1$ and $\Delta\lambda = \lambda_2 - \lambda_1$:

$$R_{out}\left(\lambda_1,\lambda_2\right)=\sigma^2\left(\frac{\lambda_1+\lambda_2}{2}\right)\int h\left(\lambda_1-\Lambda',\Lambda'\right)h\left(\lambda_1-\Lambda',\Lambda'+\Delta\lambda\right)d\Lambda' \tag{17}$$

If $h\left(\lambda,\Delta\lambda\right)$ varies slowly in λ compared to $\Delta\lambda$, then Eq. (17) can take the form

$$R_{out}\left(\lambda_1,\lambda_2\right)=\sigma^2\left(\lambda_{avg}\right)h\left(\lambda_{avg},\Delta\lambda\right)\star h\left(\lambda_{avg},\Delta\lambda\right) \tag{18}$$

where $\lambda_{avg}=\frac{\lambda_1+\lambda_2}{2},\Delta\lambda=\lambda_2-\lambda_1$, and $\star$ denotes the cross-correlation with respect to $\Delta\lambda$. This leads to the natural reparameterization $R_{out}^{'}\left(\lambda_{avg},\Delta\lambda\right)=R_{out}\left(\lambda_{avg}-\frac{\Delta\lambda}{2},\lambda_{avg}+\frac{\Delta\lambda}{2}\right)$. If we assume a Gaussian impulse response (see Section 4.3.1), i.e.,

$$h\left(\lambda_{avg},\Delta\lambda\right)\sim\mathcal{N}\left[0,\sigma_\lambda^2\left(\lambda_{avg}\right)\right] \tag{19}$$

where $\mathcal{N}$ denotes a normal distribution with zero mean and a variance of $\sigma_\lambda^2\left(\lambda_{avg}\right)$, then

$$h\left(\lambda_{avg},\Delta\lambda\right)\star h\left(\lambda_{avg},\Delta\lambda\right)\sim\mathcal{N}\left[0,2\sigma_\lambda^2\left(\lambda_{avg}\right)\right] \tag{20}$$

By using Eqs. (19) and (20), we find the relationship between the full-width-at-half-maximum (FWHM) of $h\left(\lambda_{avg},\Delta\lambda\right)$ and the FWHM of $R_{out}^{'}\left(\lambda_{avg},\Delta\lambda\right)$ to be

$$FWHM_h\left(\lambda_{avg}\right)=\frac{FWHM_{R_{out}^{'}}\left(\lambda_{avg}\right)}{\sqrt{2}} \tag{21}$$

Therefore, we can find the desired FWHM spectral resolution, $FWHM_h\left(\lambda_{avg}\right)$, by analyzing the excess noise autocorrelation matrix, $R_{out}\left(\lambda_1,\lambda_2\right)$, either directly or in normalized form (Section 4.5.1).

4.4.2 Spectrometer cross-calibration with excess noise correlations

To describe the cross-calibration of spectrometers A and B, we express the input and output excess noise correlations as

$$R_{in}\left(\lambda_1,\lambda_2\right)=\left\langle N_{in}\left(\lambda_1\right)N_{in}\left(\lambda_2\right)\right\rangle \text{ and} \tag{22}$$

$$R_{AB,out}\left(x_A,x_B\right)=\left\langle N_{A,out}\left(x_A\right)N_{B,out}\left(x_B\right)\right\rangle, \tag{23}$$

respectively, where $N_{in}(\lambda)$, $N_{A,out}(x_A)$ and $N_{B,out}(x_B)$ are the zero-mean real-valued input and output excess noise of spectrometers A and B. Note that the premise of the cross-calibration method is that the spectrometer wavelengths are unknown *a priori*, so we assume that $R_{AB,out}\left(x_A,x_B\right)$ is a function of the chosen pixels, x_A and x_B, in the respective spectrometers. Spectrometers A and B are assumed to have partially overlapping wavelength ranges but unknown pixel-to-wavelength mappings, $\lambda_A\left(x_A\right)$ and $\lambda_B\left(x_B\right)$, which can be determined through a separate procedure.

As above, from the linear shift-variant system assumption, Eq. (14) becomes

$$R_{AB,out}\left(x_A,x_B\right)=\left\langle\int N_{in}\left(\Lambda_A\right)h_A\left[\Lambda_A,\lambda_A\left(x_A\right)-\Lambda_A\right]d\Lambda_A\int N_{in}\left(\Lambda_B\right)h_B\left[\Lambda_B,\lambda_B\left(x_B\right)-\Lambda_B\right]d\Lambda_B\right\rangle. \tag{24}$$

Eq. (24) can be expressed in terms of $R_{in}\left(\lambda_A,\lambda_B\right)$ using Eq. (22):

$$R_{AB,out}\left(x_A,x_B\right)=\iint R_{in}\left(\Lambda_A,\Lambda_B\right)h_A\left[\Lambda_A,\lambda_A\left(x_A\right)-\Lambda_A\right]d\Lambda_A h_B\left[\Lambda_B,\lambda_B\left(x_B\right)-\Lambda_B\right]d\Lambda_B. \tag{25}$$

Assuming excess noise is white, we can express the input excess noise correlation as Eq. (14). Using Eq. (14) and assuming that $\sigma^2\left(\lambda\right)$ varies slowly compared to the spectral resolution, Eq. (25) becomes

$$R_{AB,out}\left(x_A,x_B\right)=\sigma^2\left\{\frac{\lambda_A\left(x_A\right)+\lambda_B\left(x_B\right)}{2}\right\}\int h_A\left[\Lambda_A,\lambda_A\left(x_A\right)-\Lambda_A\right]h_B\left[\Lambda_A,\lambda_B\left(x_B\right)-\Lambda_A\right]d\Lambda_A \tag{26}$$

For a given pixel on spectrometer A, x_A, the cross-correlation $R_{AB,out}\left(x_A,x_B\right)$ achieves a maximum when both impulse response functions, h_A and h_B, share the same maximum with respect to Λ_A in Eq. (26). Therefore, the output excess noise correlation, $R_{AB,out}\left(x_A,x_B\right)$, is maximized when $\lambda_A\left(x_A\right)=\lambda_B\left(x_B\right)$, i.e., when the pixels measure the same wavelength. Even if the excess noise is not white, this conclusion remains valid for a wide range of

$R_{in}(\lambda_1, \lambda_2)$, h_A, and h_B, provided that reasonable assumptions are made (e.g., $R_{in}(\lambda_1, \lambda_2)$ decreases with increasing $|\lambda_2 - \lambda_1|$, while h_A and h_B are symmetric in $\Delta\lambda$ and decrease with increasing $|\Delta\lambda|$).

4.4.3 Light source intrinsic spectral correlation length

Our method of spectrometer characterization, as implemented, assumes a short excess noise spectral correlation length, so that any measured spectral correlation is attributable to our spectrometer impulse response function [Eq. (18)]. Here, by extending the linear shift-variant system analysis in section 4.4.1, we assess the validity of this assumption. In particular, we experimentally place bounds on the intrinsic spectral correlation length of the light sources.

Extending on the analysis in section 4.4.1, we relax the assumption in Eq. (14) that $R_{in}(\lambda_1, \lambda_2)$ is a delta function. Thus, we start from Eq. (13):

$$R_{out}(\lambda_1, \lambda_2) = \iint R_{in}(\Lambda_1, \Lambda_2) h(\Lambda_1, \lambda_1 - \Lambda_1) d\Lambda_1 h(\Lambda_2, \lambda_2 - \Lambda_2) d\Lambda_2 \qquad (27)$$

We further assume that the intrinsic correlation function (including the wavelength-dependent variance and intrinsic spectral correlation length) is slowly varying on the scale of the spectral resolution (This is less restrictive than in section 4.4.1, where we assume the intrinsic spectral correlation length is much smaller than the spectral resolution). Our assumption leads to the natural reparameterization $R'_{in}(\lambda_{avg}, \Delta\lambda) = R_{in}\left(\lambda_{avg} - \frac{\Delta\lambda}{2}, \lambda_{avg} + \frac{\Delta\lambda}{2}\right)$, where $\lambda_{avg} = \frac{\lambda_1 + \lambda_2}{2}$ and $\Delta\lambda = \lambda_2 - \lambda_1$, where R'_{in} is slowly varying in the first argument, and symmetric in the second argument, yielding

$$R_{out}(\lambda_1, \lambda_2) = \iint R'_{in}\left(\frac{\Lambda_1 + \Lambda_2}{2}, \Lambda_2 - \Lambda_1\right) h(\Lambda_1, \lambda_1 - \Lambda_1) d\Lambda_1 h(\Lambda_2, \lambda_2 - \Lambda_2) d\Lambda_2 \qquad (28)$$

We then make the substitutions $\Lambda'_1 = \lambda_1 - \Lambda_1$ and $\Lambda'_2 = \lambda_2 - \Lambda_2$ to yield

$$R_{out}\left(\lambda_1,\lambda_2\right)=\iint R_{in}^{'}\left[\frac{\lambda_2+\lambda_1-\left(\Lambda_2'+\Lambda_1'\right)}{2},\lambda_2-\lambda_1-\left(\Lambda_2'-\Lambda_1'\right)\right]h\left(\lambda_1-\Lambda_1',\Lambda_1'\right)d\Lambda_1'h\left(\lambda_2-\Lambda_2',\Lambda_2'\right)d\Lambda_2' \tag{29}$$

As $R_{in}^{'}$ and h are both assumed to be slowly varying in their first arguments compared to their second arguments, we can approximate that

$$R_{out}\left(\lambda_1,\lambda_2\right)=R_{in}^{'}\left(\lambda_{avg},\Delta\lambda\right)\otimes\left[h\left(\lambda_{avg},\Delta\lambda\right)\star h\left(\lambda_{avg},\Delta\lambda\right)\right] \tag{30}$$

where $\star$ and $\otimes$ denote cross-correlation and convolution, respectively, with respect to $\Delta\lambda$. This suggests the natural reparameterization, $R_{out}^{'}\left(\lambda_{avg},\Delta\lambda\right)=R_{out}\left(\lambda_{avg}-\frac{\Delta\lambda}{2},\lambda_{avg}+\frac{\Delta\lambda}{2}\right)$. The term in square brackets represents the ideal excess noise correlation function in the absence of intrinsic spectral correlations in the light source. Thus, according to Eq. (30), the effect of intrinsic source excess noise correlations can be modelled as an additional convolution in $\Delta\lambda$. As $\Delta\lambda$ is related to the distance from the diagonal, the convolution implies a broadening of the quasi-diagonal. At the same time, Eq. (30) suggests a way to estimate intrinsic source correlations, if present. In particular, the width of $h\star h$ may be estimated accurately from the interferometry method, which does not require uncorrelated excess noise. At the same time $R_{out}^{'}\left(\lambda_{avg},\Delta\lambda\right)$ is the excess noise autocorrelation matrix. We empirically find that both h and $R_{out}^{'}$ are nearly Gaussian in their second arguments. If all relevant functions are Gaussian, then

$$\left[FWHM_{R_{out}^{'}}\left(\lambda_{avg}\right)\right]^2=\left[FWHM_{R_{in}^{'}}\left(\lambda_{avg}\right)\right]^2+2\left[FWHM_{h}\left(\lambda_{avg}\right)\right]^2 \tag{31}$$

Thus, the squared width of R_{in}' can be estimated from a deconvolution:

$$\left[FWHM_{R_{in}^{'}}\left(\lambda_{avg}\right)\right]^2=\left[FWHM_{R_{out}^{'}}\left(\lambda_{avg}\right)\right]^2-2\left[FWHM_{h}\left(\lambda_{avg}\right)\right]^2 \tag{32}$$

Here, $\left[FWHM_{R_{out}^{'}}\left(\lambda_{avg}\right)\right]^2$ is determined from Gaussian fitting of the excess noise autocorrelation matrix and $\left[FWHM_{h}\left(\lambda_{avg}\right)\right]^2$ is determined from Gaussian fitting of the coherence rolloff, and Eq. (18).

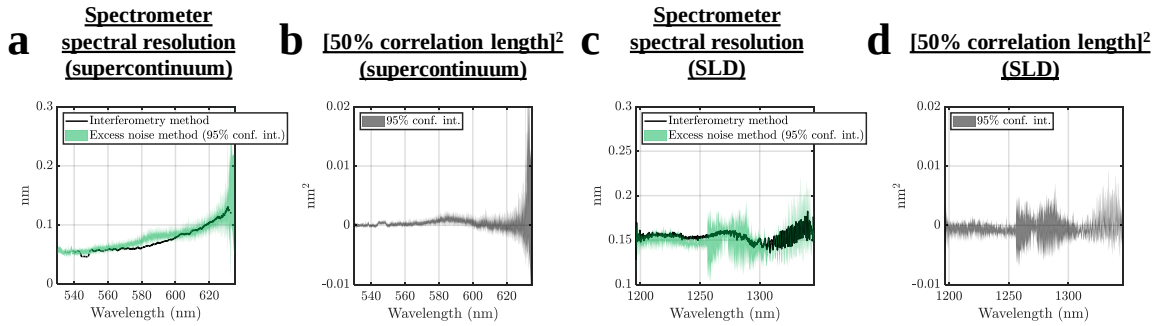

Figure 17. Intrinsic light source spectral correlations. Spectral resolution of visible light spectrometer B (Figure 27b) using a supercontinuum source (a) and commercial 1300 nm spectrometer (Figure 24a-b) using an SLD (c). Systematic overestimation by the excess noise characterization method relative to interferometry would indicate intrinsic light source correlations. To investigate this possibility, applying the deconvolution in Eq. (32), the light source intrinsic spectral correlation length squared is shown for both the supercontinuum source (b) and the SLD (d). Note that the correlation length squared is determined, as sometimes the right-hand side of Eq. (32) is negative. Further investigations of this effect are warranted, particularly for supercontinuum sources, using higher resolution spectrometers and longer integration times.

Spectral resolution estimates are reproduced with supercontinuum (Figure 17a) and SLD light sources (Figure 17c) using both interferometry, i.e. $FWHM_h$, and the proposed excess noise method, i.e. $FWHM_{R_{out}^{'}}/\sqrt{2}$, including confidence intervals. Based on Eq. (32), we find confidence intervals for the intrinsic 50% correlation length squared, determined as $\left[FWHM_{R_{in}^{'}}/2\right]^2$ (Figure 17b,d). Accounting for confidence intervals, there are no clear deviations from zero for either light source. For more precise investigation of the intrinsic spectral correlation length, particularly for the supercontinuum source, further investigation using higher resolution spectrometers such as those with virtually imaged phase arrays, relaxation of the Gaussian assumption, and longer integration times, are warranted.

While the analysis in section 4.4.1, which neglected intrinsic light source correlations, appears valid for spectrometers and sources investigated herein, three additional comments are in order. First, for the

supercontinuum source, we were able to exclude correlations on the few nanometer scale by fitting a two Gaussian model (see Figure 20 and discussion at the end of Section 4.5.1). Second, in applications where intrinsic source correlations (i.e. $R_{in}^{'}$) are present and known *a priori*, they can be incorporated into the analysis, as per Eq. (30), to improve accuracy. Third, there are theoretical arguments supporting the incoherence of excess noise from pure spontaneous emission.

4.4.4 Relationship of spectral correlations to noise floor

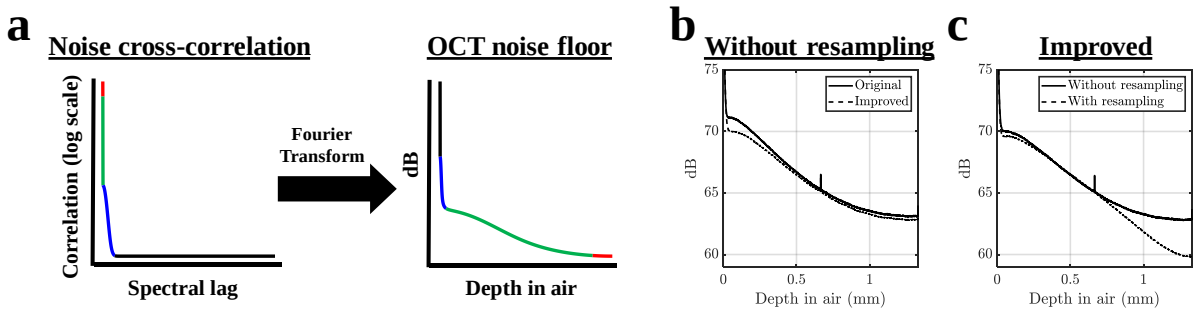

Figure 18. Noise floor rolloff. a Diagram of noise spectral cross-correlation and its Fourier transform pair, the OCT noise floor. The red component represents shot noise, the green component represents spectral resolution, the blue component represents the broader excess noise correlations from the light source, and the black component represents spectrum fluctuations related to laser instability. b The improved configuration (Figure 25b) narrows the excess noise spectral correlations, resulting in a broader noise floor relative to the original configuration (Figure 25a). c The resampling procedure broadens the noise spectral correlations digitally, resulting in a narrower noise floor with a steeper rolloff. The inverse relationship between the widths of the spectral correlations and the noise floor are understood through the Wiener-Khinchin theorem.

Spectral correlations were previously discussed in the context of supercontinuum sources and related to the rolloff of the spectral/Fourier domain OCT noise floor (the Fourier transform of the correlation function). However, in this prior work, spectral correlations, causing the noise floor reduction with depth, were attributed to the supercontinuum source [89-91]. Here we argue that the intrinsic spectral resolution of the spectrometer and the linear in wavenumber resampling procedure must both be considered in predicting the OCT noise rolloff. Notably, with an improved spectral resolution configuration (Figure 25b), we can broaden the green component in the noise rolloff profile (Figure 18a) to reduce the noise at short path length

mismatches (Figure 18b), without changing the light source. Also, the resampling procedure, commonly applied in OCT to ensure spectral data is linearly spaced in wavenumber, digitally induces spectral correlations and thus narrows the noise floor, reducing the noise at larger path length mismatches (Figure 18c). Therefore, the noise rolloff, commonly observed in OCT images using supercontinuum light sources, is not only affected by the intrinsic spectral correlations of the source, but also by spectral resolution of the spectrometer and the resampling procedure.

4.5. Method

Here, we present a method that provides both the spectral resolution and wavelength correspondence between spectrometers from a single time series of noise registered by different sensor pixels. If the intrinsic source noise is incoherent or uncorrelated between wavelengths separated on the scale of the spectral resolution, then any measured excess noise correlation between pixels is attributable to the nonzero spectral resolution (Figure 12d and Section 4.5.1), which causes those pixels to measure similar wavelengths (see Section 4.4.3 for a discussion of the applicability when this assumption is violated). The local extent of this measured correlation across pixels in the spectrometer relates to the spectral resolution. The conditions responsible for spectrally uncorrelated or "incoherent" noise were briefly described in Section 4.1.1.

4.5.1 Autocorrelation matrix estimation and normalization

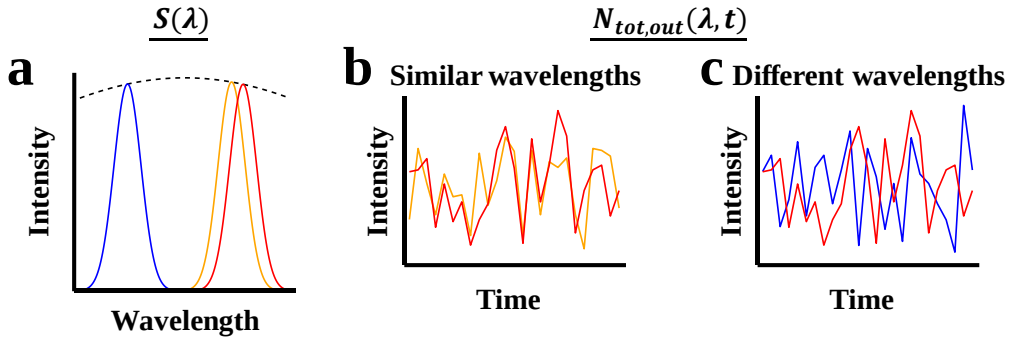

Figure 19. Excess noise spectrally encodes broadband light. a Three narrowband channels, e.g. spectrometer pixels, are represented as individual colors within a broadband spectrum (dotted line). b Since the red and orange channels measure overlapping wavelengths (a), their excess noise fluctuations are similar, leading to higher correlation. c By comparison, since the red and blue channels do not measure

overlapping wavelengths (a), their excess noise fluctuations are dissimilar, leading to lower correlation. This simple principle forms the basis for the proposed methods of spectrometer characterization and cross-calibration.

Our measured spectrum comprises spectral channels at every wavelength, λ, each with a corresponding intensity, $S(\lambda)$ (Figure 19a). The noise values (Figure 19b,c) at each time point, t, measured by the spectrometer after mean subtraction, $N_{tot,out}(\lambda,t)$, are represented by an X by N matrix, with X being the number of sensor pixels, or wavelengths, and N being the total number of lines in time. The autocorrelation of $N_{tot,out}(\lambda,t)$ yields the X by X symmetric total noise autocorrelation matrix, $R_{tot}(\lambda_1,\lambda_2)=\langle N_{tot,out}(\lambda_1,t)N_{tot,out}(\lambda_2,t)\rangle_t$, where $\langle\bullet\rangle_t$ denotes a time average. Since total noise includes independent contributions from detector noise (comprising dark noise and read noise), shot noise, and excess noise, we estimated the excess noise autocorrelation matrix, $R_{out}(\lambda_1,\lambda_2)$, described in section 4.4.1, by subtraction of the detector noise autocorrelation matrix, $R_{detector}(\lambda_1,\lambda_2)$ and the shot noise autocorrelation matrix, $R_{shot}(\lambda_1,\lambda_2)$:

$$R_{out}(\lambda_1,\lambda_2)=R_{tot}(\lambda_1,\lambda_2)-R_{detector}(\lambda_1,\lambda_2)-R_{shot}(\lambda_1,\lambda_2) \tag{33}$$

$R_{detector}(\lambda_1,\lambda_2)$ is estimated similarly to $R_{tot}(\lambda_1,\lambda_2)$, albeit from a dataset acquired with no light on the detector. $R_{shot}(\lambda_1,\lambda_2)$ is a diagonal matrix with the shot noise variance along the diagonal. Note that while sometimes relative intensity noise (RIN) and excess noise are used interchangeably [77, 79], this usage is not universal and we refrain from discussing RIN. Since shot noise follows a Poisson distribution, the variance in a given pixel can be estimated from the source spectrum gray level (DN), given by $S_{out}(\lambda)$, in that pixel given, the Full Well Capacity (FWC) and bit depth (BD):

$$R_{shot}(\lambda,\lambda)=S_{out}(\lambda)\left(\frac{FWC}{2^{BD}}\right)\left(\frac{2^{BD}}{FWC}\right)^2=S_{out}(\lambda)\left(\frac{2^{BD}}{FWC}\right) \tag{34}$$

When the full-well capacity of the camera was not precisely known, it was estimated by performing a quadratic polynomial fit of the pixel noise versus source spectrum gray level [92]. After normalization to the product of the excess noise standard deviations in the corresponding pixels, we obtain the experimental normalized excess noise autocorrelation matrix:

$$r_{out}\left(\lambda_1,\lambda_2\right)=\frac{R_{out}\left(\lambda_1,\lambda_2\right)}{\sqrt{R_{out}\left(\lambda_1,\lambda_1\right)R_{out}\left(\lambda_2,\lambda_2\right)}} \tag{35}$$

where the diagonals of the autocorrelation matrix, $R_{out}\left(\lambda,\lambda\right)$, represent the variance. An alternative normalization to the source spectrum gray level at each wavelength, $S_{out}\left(\lambda\right)$, yields the matrix, $r_{out}^{coeff}\left(\lambda_1,\lambda_2\right)$, in terms of the relative magnitude of excess noise fluctuations. This normalization enables direct comparison of excess noise correlations between different light sources or spectrometers. For this normalization, the diagonal is the excess noise coefficient, or the variance of intensity fluctuations relative to the mean intensity squared.

$$r_{out}^{coeff}\left(\lambda_1,\lambda_2\right)=\frac{R_{out}\left(\lambda_1,\lambda_2\right)}{S_{out}\left(\lambda_1\right)S_{out}\left(\lambda_2\right)} \tag{36}$$

Broadening of the quasi-diagonal of $r_{out}\left(\lambda_1,\lambda_2\right)$ was quantified by the full-width-at-half-maximum (FWHM) of a fitted Gaussian function centered on the diagonal (Figure 20). The FWHM of $r_{out}\left(\lambda_1,\lambda_2\right)$, assumed to be equal to the FWHM of $\mathrm{R}_{out}\left(\lambda_1,\lambda_2\right)$, in units of pixels was converted to FWHM spectral resolution, $FWHM_h\left(\lambda\right)$, based on Eq. (21) and our pixel-to-wavelength calibration [57] (Figure 15b).

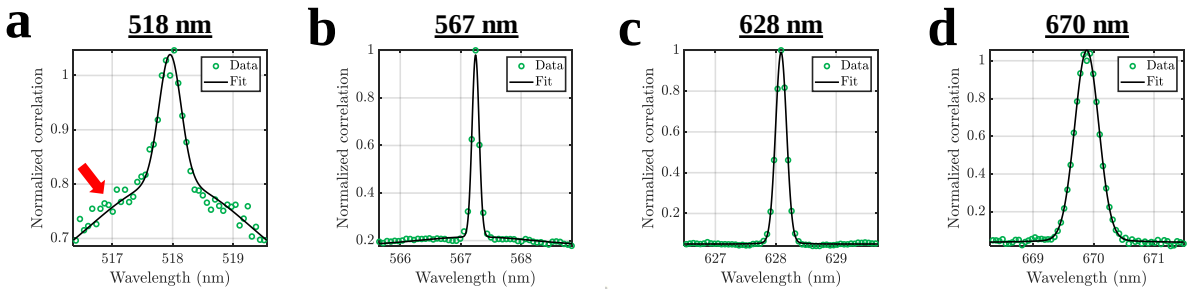

Figure 20. Autocorrelation matrix quasi-diagonal fitting. Two Gaussian fitting of the autocorrelation matrix along the diagonal at wavelengths 518 nm (a), 567 nm (b), 628 nm (c), and 670 nm (d). The red arrow indicates the appearance of the broader Gaussian pedestal at shorter wavelengths that is not informative about the spectrometer spectral resolution.

Some spectral ranges of the supercontinuum contained an additional excess noise component, evidently not related to spectral resolution. This additional component appeared as a broader Gaussian pedestal (Figure 20a, red arrow) in the excess noise autocorrelation function, with a correlation length of 2-3 nm. Within our measured bandwidth, this broader excess noise component was most significant below 555 nm. This component is likely due to intrinsic noise correlations across broader spectral ranges of the light source, which violate the white noise assumption [75]. To avoid confounding our estimates of spectral resolution, we fit a two Gaussian model where spectral resolution was extracted from the more informative, narrower Gaussian component.

4.5.2 Cross-correlation matrix estimation and normalization

Spectrometer cross-calibration requires the cross-correlation of simultaneously measured noise time courses from spectrometer A, $N_{A,tot,out}\left(x_A,t\right)$, and spectrometer B, $N_{B,tot,out}\left(x_B,t\right)$, for each time point, t, and each corresponding spectrometer pixel, x_A and x_B, respectively. This yields the total noise cross-correlation matrix, $R_{AB,tot}\left(x_A,x_B\right)=\left\langle N_{A,tot,out}\left(x_A,t\right)N_{B,tot,out}\left(x_B,t\right)\right\rangle_t$. Unlike the autocorrelation matrix in Section 4.5.1, $R_{AB,tot}\left(x_A,x_B\right)$ is not influenced by shot noise and detector noise, which should be uncorrelated between spectrometers. Therefore $R_{AB,tot}\left(x_A,x_B\right)$ is equal to the excess noise cross-

correlation matrix, $R_{AB,out}\left(x_A, x_B\right)$, described in section 4.4.2. Through normalization to the product of the excess noise standard deviations in the corresponding pixel for both spectrometers, we obtain the experimental normalized excess noise cross-correlation matrix, $r_{AB,out}\left(x_A, x_B\right)$:

$$r_{AB,out}\left(x_A, x_B\right) = \frac{R_{AB,out}\left(x_A, x_B\right)}{\sqrt{R_{A,out}\left(x_A, x_A\right) R_{B,out}\left(x_B, x_B\right)}} \tag{37}$$

$R_{A,out}\left(x_A, x_A\right)$ and $R_{B,out}\left(x_B, x_B\right)$ are the excess noise autocorrelation matrices (see Section 4.5.1) for each spectrometer, containing the variances for each pixel along the principal diagonal. For a given pixel in one spectrometer, the pixel in the other spectrometer with the highest correlation, given by $r_{AB,out}\left(x_A, x_B\right)$, measures similar wavelengths.

4.5.3 Data acquisition and processing

Spectrometers A and B were built for visible light spectral/Fourier domain OCT systems for *in vivo* mouse and human retinal imaging with supercontinuum light sources (EXW-12 and EXU-3, NKT Photonics) with pulse repetition rates of 78 MHz and 156 MHz, respectively. Each spectrometer has a transmission grating (1800 l/mm @ 532 nm, Wasatch Photonics) and a complementary metal-oxide semiconductor (CMOS) line scan camera (SPL 4096-140 km, Basler) with a nominal 20 μm pixel height and a 10 μm pixel pitch. Spectrometer A (mouse) uses a 33 mm focal length reflective collimator (RC08APC-P01, Thorlabs) and a 75 mm effective focal length achromatic doublet pair focusing lens (AC508-150-A, Thorlabs), while spectrometer B (human) uses a 50.8 mm focal length reflective collimator (RC12PC-P01, Thorlabs) and a 125 mm effective focal length achromatic doublet pair focusing lens (AC508-250-A, Thorlabs). Our characterization and calibration approaches were validated with a 1 mW collimated laser diode at 635 nm (CPS180, Thorlabs) and a 4.5 mW collimated laser-diode-pumped laser module at 532 nm (CPS532, Thorlabs). The characterization and calibration methods utilized time courses with 32768 points acquired at a 70 kHz line rate. The spectrum intensity was maximized while avoiding saturation to increase excess noise for robust measurements. The light intensity was controlled by a variable neutral density filter in the reference arm, and time courses were

acquired with the sample arm covered. For demonstration of the cross-calibration method, spectrometer A (mouse) was used to calibrate spectrometer B (human) using the supercontinuum light source (EXW-12, NKT Photonics).

4.5.4 Mouse retinal imaging with visible light OCT

4.6. Results

A free-space visible light spectral/Fourier domain OCT system [32] was used for *in vivo* retinal imaging of one- to eighteen-month-old mice, as approved by our Institutional Animal Care and Use Committee (IACUC). Experiments were performed on four pigmented mice (C57BL/6J, The Jackson Laboratory) and two albino mice (BALB/cJ, The Jackson Laboratory). In addition to the improved spectrometer, several additional improvements were incorporated relative to a previous report [32]. We replaced the 50/50 beamsplitter with a 90/10 beamsplitter (BS028, Thorlabs) and added a polarization controller (FPC-3, Fiber Control) to the fibre connected to the spectrometer. We also broadened the bandwidth by utilizing all 4096 sensor pixels instead of the previous 3072 pixel configuration [32]. The full spectral width used for imaging was 259 nm, and the axial resolution was 1.0 μm in tissue. Retinal imaging was performed with a 300 μW power on the cornea with a 30 kHz line rate. Eight repeated volumetric datasets with 512 a-lines and 128 b-scans each over 17.5 seconds were acquired over a 1 mm range along the fast axis, with a total slow axis offset of 0.12 mm range for speckle reduction. The raw fringes were processed with linear wavenumber resampling, spatially dependent dispersion compensation [32], spectral shaping, Fourier transformation, and axial motion correction. Images were averaged prior to display.

4.6.1 Correlation between excess noise correlation and spectral resolution

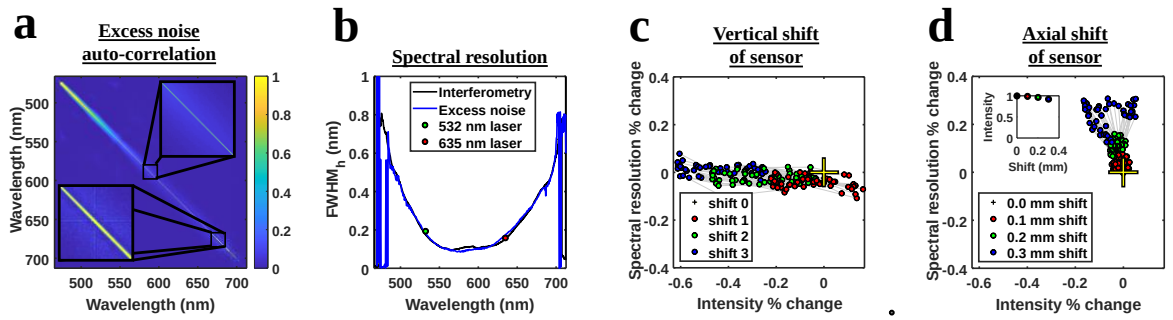

Figure 21. Excess noise autocorrelation can characterize spectrometers. a Excess noise autocorrelation matrix from a previously reported visible light OCT spectrometer [32]. The zoom-ins of the autocorrelation matrix show a thinner quasi-diagonal at central wavelengths than at peripheral wavelengths in the spectrum. b The spectral resolution measured from this autocorrelation matrix with the proposed method agrees well with the conventional interferometry and narrowband laser calibration method results. c Vertical shifting of the sensor (as depicted in Figure 12a), relative to the optimal position, mainly changes the intensity measured by the pixels (dots). Shift 1 denotes the smallest shift, while shift 3 denotes the largest shift from the optimal position. Due to the small magnitude of the shift relative to the translation stage screw pitch, the shifts were not precisely measured. d Axial shifting of the sensor (as depicted in Figure 12a) towards the focusing lens, relative to the optimal position, mainly changes the spectral resolution. The subplot shows the summed total spectrum intensity for each shift normalized to the total spectrum intensity at the optimal position.

The excess noise autocorrelation matrix (Figure 21a), estimated from individual pixel time courses and corrected for shot and detector noise (comprising dark noise and read noise), is the basis of our method for characterizing the spectral resolution (see Section 4.5.1). Shot noise must be uncorrelated between pixels, with a variance proportional to the pixel grey level, while the excess noise variance goes as the square of the grey level. While relative intensity noise (RIN) and excess noise are sometimes used interchangeably [77], this usage is not universal [72, 79, 93], and we will refrain from discussing RIN. Practically, we can distinguish shot noise and detector noise from excess noise based on the quadratic light intensity dependence of the latter. Pairs of pixels with high excess noise correlations are observed along a quasi-diagonal region (Figure 21a subplots). A broader quasi-diagonal width, seen here at the edges of the sensor (lower right of the matrix), implies degraded spectral resolution (Figure 21b) compared to the narrower quasi-diagonal width towards the middle of the sensor (center of the matrix). For a visible light OCT spectrometer used for mouse retinal imaging [32], spectral resolutions from the excess noise method were

directly compared to those obtained from both narrow linewidth (Figure 12b) and interferometry (Figure 12c) methods (see Section 4.2), which required additional narrowband light sources and an auxiliary interferometer, respectively. The three methods agree well across most of the spectrometer range (Figure 21b), supporting the validity of the excess noise method. The methods disagree at the edges of the spectral range due to the low intensities and insufficient excess noise. The excess noise of an infrared (NIR-II) superluminescent diode, though more than two orders of magnitude smaller than that of the visible supercontinuum (see Section 4.6.2), was further employed to characterize two spectrometers, yielding results in agreement with interferometry (see Section 4.6.3).

4.6.2 Feasibility with other light sources

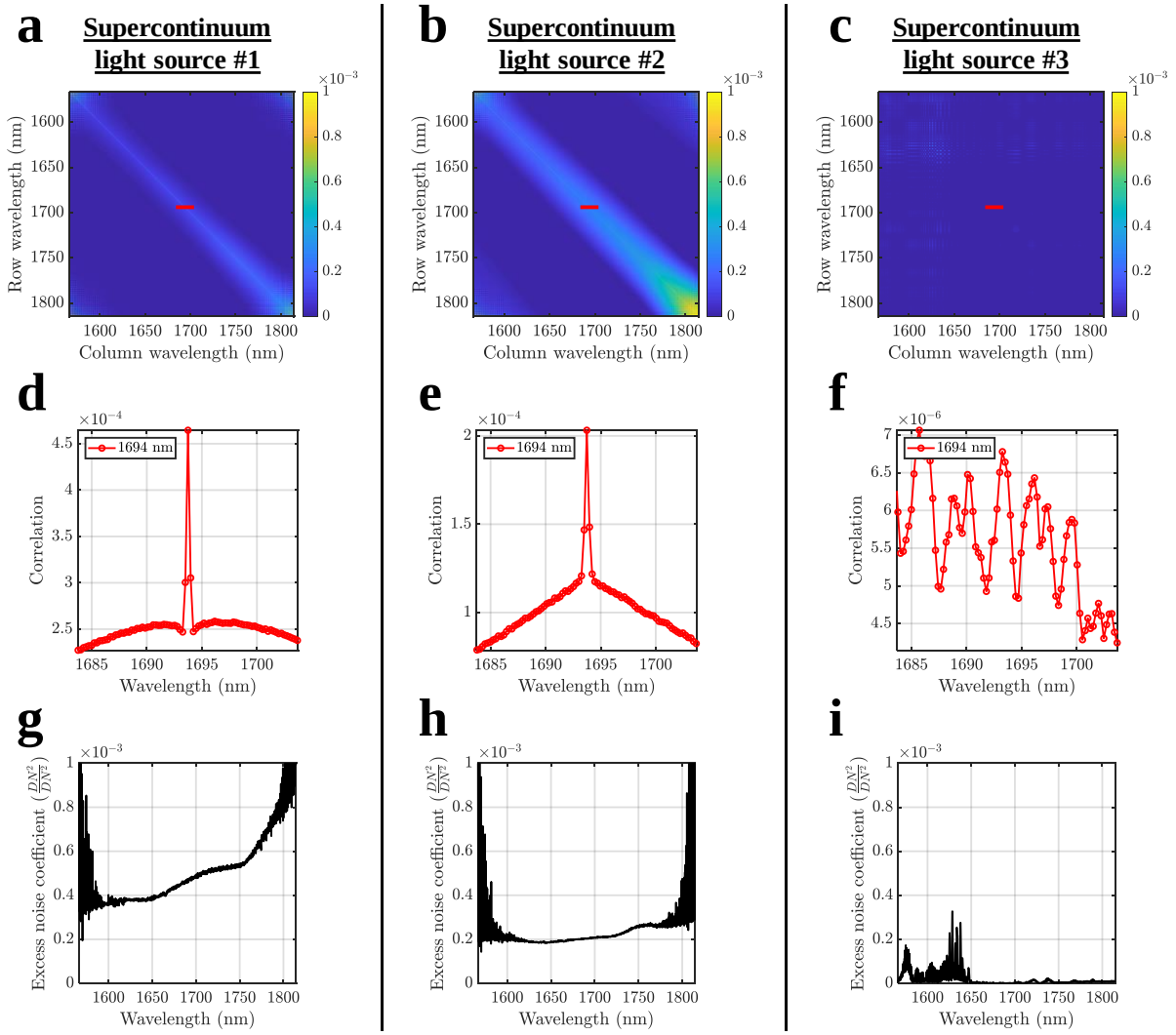

Figure 22. Feasibility of spectrometer characterization method with different supercontinuum light sources. a-c Normalized excess noise autocorrelation matrices in coefficient form [Eq. (36)] for supercontinuum sources #1 (a), #2 (b), and #3 (c). Red lines in a-c represent the locations of d-f. The narrow peaks in zooms around the diagonal near 1694 nm (d,e), which are informative about the spectral resolution, are not apparent in f. Respective excess noise coefficients (diagonals of a-c), plotted in g-i, show that source #3 possesses the least excess noise.

Our characterization approach was applied to a spectrometer centered around 1700 nm (1567-1815 nm spectral range), to investigate the performance of supercontinuum light sources from different manufacturers with different excess noise levels. Light source #1 and light source #2 (EXW-12, NKT Photonics) were broadband supercontinua based on photonic crystal fibers with repetition rates of 40 MHz

and 78 MHz, respectively. Light source # 3 had a repetition rate of 50 MHz, but produced a narrower spectrum from self-phase modulation.

The characterization method was applied to time courses with 46900 points acquired at a 47 kHz line rate. Spectrometer calibration was deemed possible with a quasi-diagonal excess noise component (Figure 22a,b) that correctly predicted the spectral resolution determined by broadband interferometry. For each source, we also quantified the excess noise coefficient as described previously described (Figure 22g-i) [92]. More excess noise appears to give more robust measurements (Figure 22a,b,d,e,g,h). Importantly, the characterization failed with the supercontinuum light source based on pure self-phase modulation, which also had significantly less excess noise (Figure 22c,f,i). Self-phase modulation may also lead to correlated fluctuations at different wavelengths, invalidating the white noise assumption.

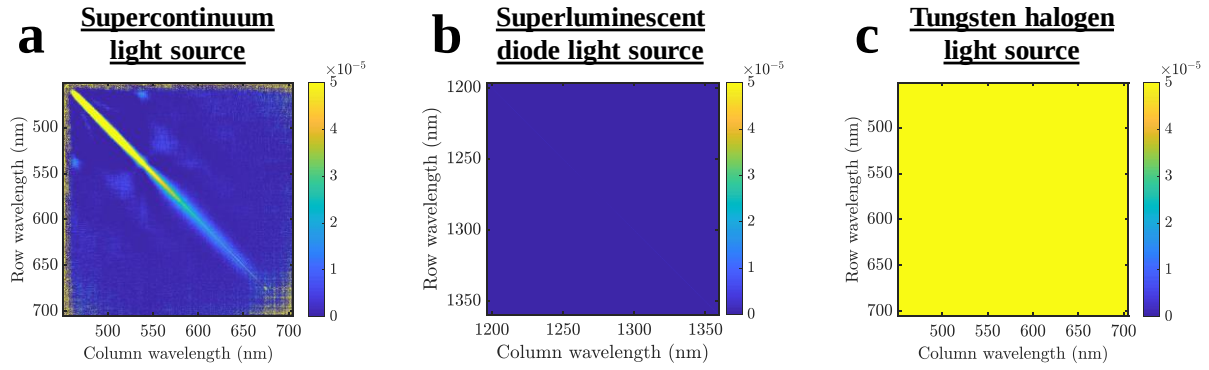

Figure 23. Feasibility of spectrometer characterization method with non-supercontinuum light sources. Normalized excess noise autocorrelation matrices in coefficient form [Eq. (36)] for a supercontinuum source (a), superluminescent diode (SLD) (b), and a tungsten halogen light source (c) show that the significant excess noise correlations along the quasi-diagonal are not apparent in all broadband sources.

Furthermore, we assessed the feasibility of applying our approach with non-supercontinuum light sources: a superluminescent diode (SLD1325, Thorlabs) (Figure 23b) and a tungsten halogen light source (JCR21V-150W, Ushio) (Figure 23c). Autocorrelation matrices were normalized according to Eq. (36) and compared to those of the original supercontinuum light source used in this study (EXW-12, NKT Photonics) (Figure 23a). Correlations were observed with the superluminscent diode light source, though excess noise levels

were very low (Figure 23b). Further investigation (see Section 4.6.3) later revealed that indeed, excess noise characterization was possible with the SLD source. The tungsten halogen source, though having large excess noise, likely related to technical noise, did not clearly show excess noise correlations along the quasi-diagonal, which are required for characterization (Figure 23c).

4.6.3 Excess noise in a superluminescent diode (SLD) can also characterize spectrometers

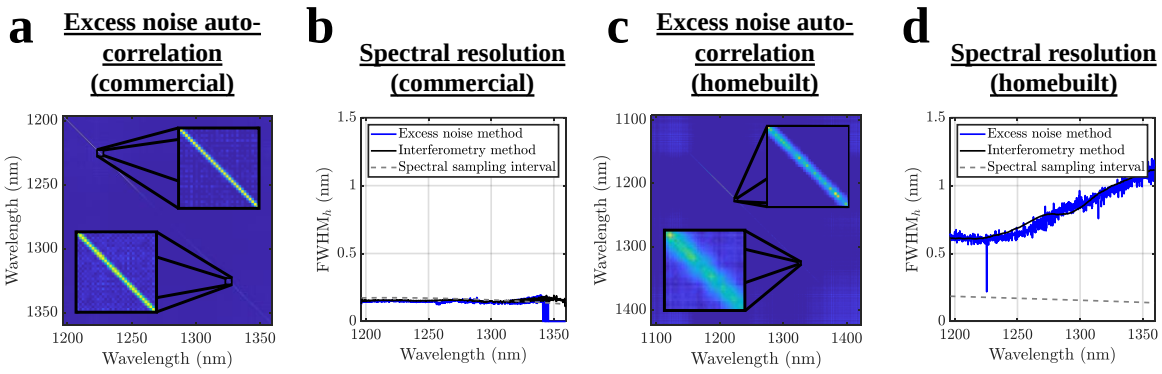

Figure 24. Spectrometer characterization with a superluminescent diode (SLD) source. Excess noise autocorrelation matrices (a,c) and estimated spectral resolutions (b,d), employing an SLD source with both a commercial spectrometer (a,b) and a homebuilt spectrometer (c,d), the latter with a coarser spectral resolution. Insets in a,c are zooms of the respective quasi-diagonals from 1223-1228 nm (upper right) and from 1323-1328 nm (lower left). Although the homebuilt spectrometer (d) has a larger spectral range, the spectral resolution is only shown across the spectral range of the commercial spectrometer (b) to facilitate comparison.

Superluminescent diodes (SLDs) are less expensive and exhibit lower excess noise than supercontinuum sources, making them the light source of choice for OCT and many sensing applications. Thus, we investigated the feasibility of employing an SLD for spectrometer characterization, with an extended integration time of 0.72 seconds (compared to the 0.47 seconds used for visible light supercontinuum sources). Spectral resolution measurements were first performed on a 91 kHz line rate spectrometer inside a commercial OCT system (TELESTO-II, Thorlabs), using the built-in SLD light source (SLD1325, Thorlabs). The non-uniform spectral shape of the commercial SLD prevents simultaneously operating near the full well capacity of each pixel, which is desirable to maximize contribution of excess noise relative to

other noise sources. Thus, we acquired multiple time courses with different levels of attenuation, to ensure the existence of a time course for each pixel with counts just below the full well capacity. No other measures were taken to enhance excess noise. For this spectrometer, although the spectral resolution was comparable to the spectral sampling interval (Figure 24b), leading to a narrow quasi-diagonal with decorrelation within two pixels from the diagonal (Figure 24a insets), spectral resolution measurements are nonetheless possible, showing (Figure 24b) good agreement with the gold standard interferometry method.

We next performed measurements on an auxiliary homebuilt spectrometer, employing the same SLD light source. This homebuilt spectrometer had a spatially varying spectral resolution that greatly exceeded the spectral sampling interval (Figure 24d). Briefly, the light entering the spectrometer was collimated with a 40 mm achromatic doublet (AC254-040-C, Thorlabs). A volume transmission grating (1145 lines per millimeter, Wasatch Photonics) dispersed the light, which was then focused onto a 147 kHz line scan camera (GL2048R, Sensors Unlimited) using an achromatic doublet pair with an effective focal length of 40 mm (AC300-080-C, Thorlabs). As the spectral resolution of this spectrometer was coarse relative to the spectral sampling interval, the quasi-diagonal of the excess noise correlation matrix was likewise broad (Figure 24c). The coarse spectral resolution was quantitatively confirmed by the interferometry method (Figure 24d). Since the spectral range of the homebuilt spectrometer was wider than that of the SLD light source, and neither method could characterize spectral resolution at the edges of the spectrometer range, the full spectrometer range is not shown in Figure 24d. In summary, excess noise characterization agreed with interferometry across two spectral resolution ranges (Figure 24b,d), supporting the potential to perform spectrometer calibration with excess noise of an SLD source.

Notably, despite the extended integration time, spectrometer characterization results with the SLD were noisy, particularly near the edges of the light source spectrum. We suggest that although the low noise of superluminescent diodes is an asset in OCT, reduced excess noise may be detrimental to our method of characterization, which is most efficient in the regime where excess noise dominates shot noise and detector noise. To this end, strategies such as reducing gain saturation by driving the SLD at a lower current, and

reducing the exposure time while maintaining count levels near the full well capacity of each pixel, may help to improve upon the results presented here.

4.6.4 Validation through misalignment

Returning to the visible light OCT spectrometer, the sensor was then deliberately misaligned by translation in the vertical and axial directions (Figure 12a) to investigate the effects on both the spectral resolution and intensity (taken as the pixel grey level). Vertical misalignment results in the focused line missing the sensor, reducing the intensity (Figure 21c), while axial misalignment defocuses the light hitting the sensor, reducing the intensity and degrading the spectral resolution. Due to our asymmetric pixel size of 10 x 20 (horizontal x vertical) microns, the spectral resolution is far more sensitive than the intensity to axial misalignment (Figure 21d). Thus, the intensity and spectral resolution are complimentary, and both are needed for accurate spectrometer alignment.

4.6.5 Improving spectrometer alignment

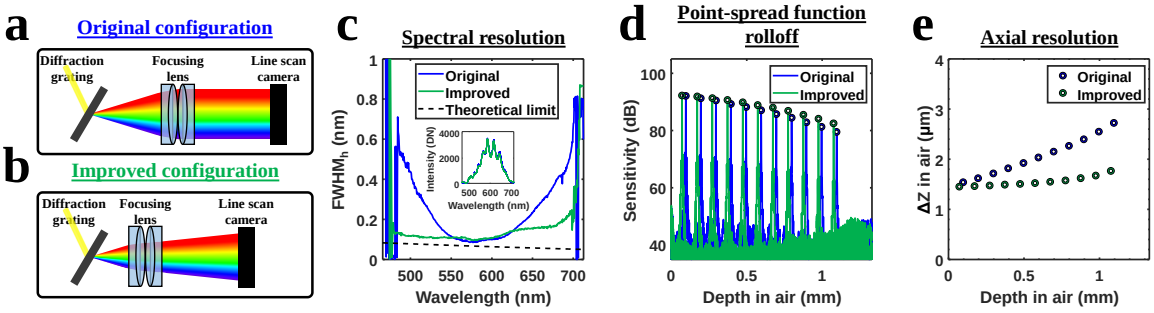

Figure 25. Quasi-real-time characterization improves the OCT spectrometer alignment. a Original spectrometer configuration with the diffraction grating at the back focal plane of the focusing lens. b Improved spectrometer configuration enabled by monitoring the spectral resolution during the alignment process. c The spectral resolution was noticeably more uniform across the spectrum in the improved configuration, though the measured spectrum intensities of both configurations, with an input power into the spectrometer of 1.55 μW, were indistinguishable (inset). The OCT point spread function rolloff (d) and axial resolution degradation versus depth (e) demonstrate a marked improvement.

Next, we investigated further rearrangement of the optical components while monitoring the spectral resolution and intensity simultaneously. We improved our original spectrometer primarily by translating the focusing lens and sensor closer to the diffraction grating compared to the original back focal plane configuration (Figure 25a,b). Although these two positions yielded very different spectral resolutions (Figure 25c), they were essentially indistinguishable based on the conventional metrics of the spectral shape and intensity (Figure 25c subplot). This is expected because aberrations, including defocusing, along the vertical plane (Figure 12a) affect the registered intensity, while those along the horizontal plane (Figure 12a) affect the spectral resolution. In this case, the asymmetric pixel size enabled improvement of the horizontal focus, i.e., spectral resolution, at the expense of the vertical focus, without compromising the intensity. The improved configuration homogenized the spectral resolution across the spectral range (Figure 25c). The theoretical spectral resolution limit (see Section 4.3.1) is shown for reference.

For this spectrometer, designated henceforth as spectrometer A, the point spread function (PSF) rolloff improved to 8.7 dB, from 11.7 dB (Figure 25d), and the axial resolution degradation improved to 18%, from 75% (Figure 25e), over the first 1 mm of imaging depth in air (75% of the imaging range). The maximal sensitivity was virtually unchanged in the improved configuration. A change was noted in the noise floor rolloff, explainable through the Wiener-Khinchin theorem (see Section 4.4.4). For another spectrometer, designated henceforth as spectrometer B, for human retinal imaging, a similar alignment procedure improved the PSF rolloff to 3.4 dB, from 6.3 dB, and improved the axial resolution degradation to 5%, from 43%, over the first 1 mm of imaging depth in air (48% of the imaging range) (see Section 4.6.7). The near-uniform axial resolution arises from mitigation of the wavelength-dependent spectral resolution (wavenumber space), which mitigates the spectrally dependent rolloff. The improvement mechanism is confirmed by ray tracing simulations (see Section 4.3.2).

4.6.6 Mouse retinal imaging

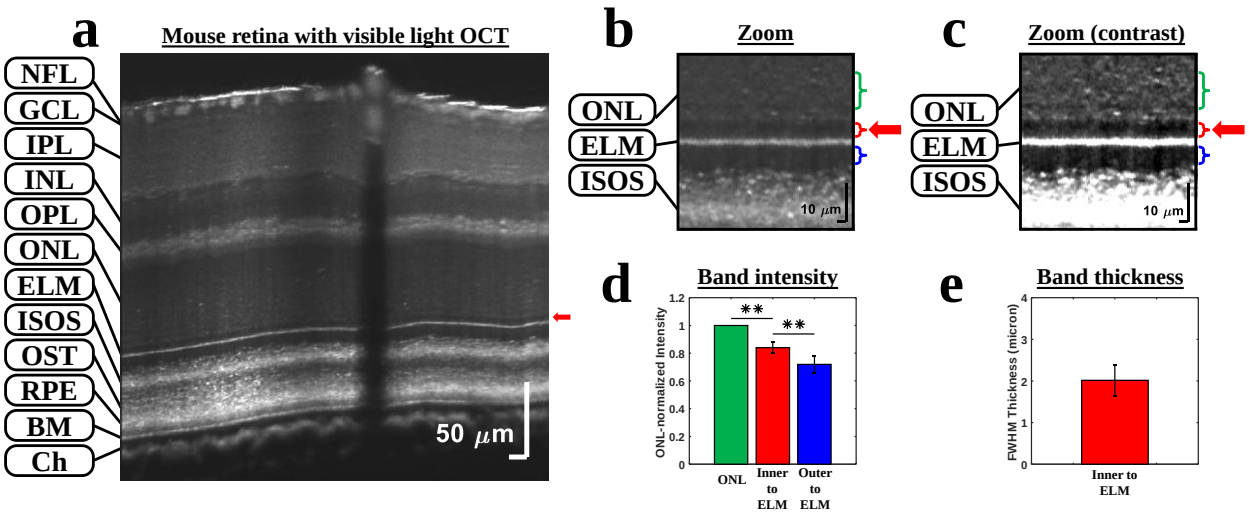

Figure 26. Visible light OCT visualizes a new outer retinal band with an improved spectrometer. a Cross-sectional linear-scaled image of a pigmented mouse retina, acquired by a visible light OCT system with a spectrometer aligned using excess noise correlations Figure 21 and Figure 25). A total of 1024 frames, acquired over 17.5 seconds with a 0.12 mm offset along the slow axis, were averaged. The red arrow indicates a dark band inner to the ELM. b Linear-scaled, outer retinal zoomed-in view showing the newly visualized dark band (red arrow). c Contrast-enhanced zoomed-in view on a linear scale. d The ONL-normalized intensity of the dark band inner to the ELM (red brackets in b,c) is significantly different from 1 and from that of the inner segments (blue brackets in b,c) in six mice (The ONL region for normalization is denoted by green brackets in b,c). e The thickness of this dark band, taken as the FWHM of a fitted Gaussian, was ~2 µm in six mice. Error bars represent standard deviations across subjects (p<0.05). Note that no error bars are shown for the ONL in d due to normalization. (NFL: nerve fiber layer; GCL: ganglion cell layer; IPL: inner plexiform layer; INL: inner nuclear layer; OPL: outer plexiform layer; ONL: outer nuclear layer; ELM: external limiting membrane; ISOS: inner segment/outer segment junction; OST: photoreceptor outer segment tips; RPE: retinal pigment epithelium; BM: Bruch's membrane; Ch: choroid).**

When employed in a spectral/Fourier domain visible light OCT system (Figure 26a), the improved spectrometer A helped visualize a hyporeflective band inner to the external limiting membrane (ELM) in the mouse retina (Figure 26b,c). This band was found to possess different reflectivity than both the inner segments (IS) and outer nuclear layer (ONL) (Figure 26d). Though situated in a stratum conventionally assigned to the ONL, a layer mostly composed of cell bodies, this hyporeflective band could represent a cell nuclei free layer inner to the junctional complexes that comprise the ELM observed in fluorescence microscopy [94] and electron microscopy [95]. The reflectivity and regularity of this band could relate to photoreceptor or Müller cell health and organization. While several bands are more consistently resolved

with visible light OCT than with near-infrared OCT, this thin hyporeflective band (Figure 26e) is, to the best of our knowledge, the first new retinal feature revealed by visible light OCT.

4.6.7 Human retinal imaging

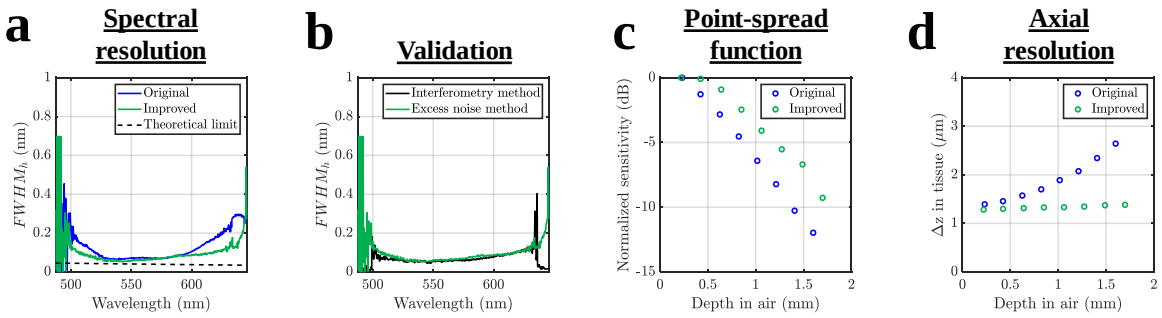

Figure 27. Quasi-real time characterization improves human OCT spectrometer alignment. a Spectral resolution across the spectrum for the original and improved configurations of spectrometer B (analogous to Figure 25a,b for spectrometer A), achieved using excess noise correlations for alignment. b Validation of excess noise method against broadband interferometry for the improved configuration. c OCT point-spread function rolloff. d Axial resolution degradation versus depth in air.

The excess noise correlation method was applied to a human visible light OCT spectrometer [34] (spectrometer B) to improve its performance by moving the focusing lens closer to the diffraction grating, as shown in Figure 25a-b (Figure 27a). The sensitivity rolloff improved to 6.9 dB, from 12.6 dB, and the axial resolution degradation improved to 8%, from 89%, at a 1.5 mm imaging depth in air (Figure 27c,d). These marked improvements in spectral resolution are supported by ray tracing described in Section 4.3.2. Having a full spectral bandwidth of 156 nm, ~0.6 times than that of spectrometer A, shown in Figure 25, spectrometer B achieves ~0.6 times finer spectral resolution. In addition, compared to the higher noise, lower repetition rate source used in Figure 25, this spectrometer used a lower noise, higher repetition rate source. Still, the excess noise method showed good agreement with the broadband interferometry method (Figure 27b). Therefore, for investigated spectrometers, our spectral resolution measurement is not limited by intrinsic spectral correlations of the supercontinuum light source, and the smallest measurable spectral resolution is less than 0.05 nm (Figure 27b). Detailed investigation of potential intrinsic correlations is described in Section 4.4.3.

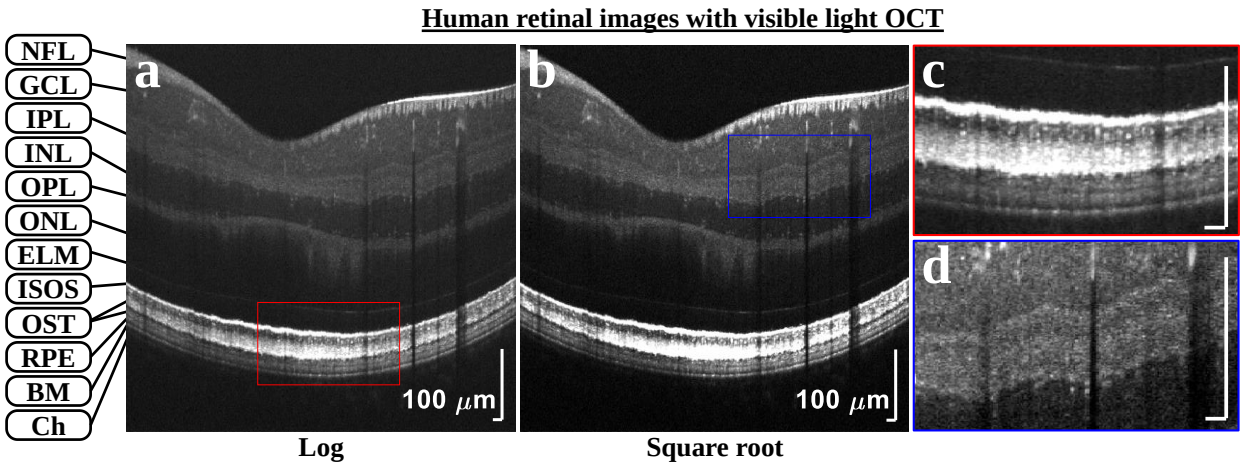

Figure 28. Visible light OCT of the human retina. Cross-sectional images of the human retina, on log (a) and square root (b) scale, acquired by a visible light OCT system with a spectrometer aligned by excess noise correlations (NFL: Nerve Fibre Layer; GCL: Ganglion Cell Layer; IPL: Inner Plexiform layer; INL: Inner Nuclear Layer; OPL: Outer Plexiform Layer; ONL: Outer Nuclear Layer; ELM: External Limiting Membrane; ISOS: Inner Segment / Outer Segment Junction; OST: photoreceptor Outer Segment Tips; RPE: Retinal Pigment Epithelium; BM: Bruch's Membrane; Ch: Choroid).

A fiber-based visible light spectral/Fourier domain OCT system [34] with the previously described spectrometer improvements was used for *in vivo* retinal imaging of a twenty-six year old human male (Figure 28). Retinal imaging was performed with 150 μW power on the cornea with a 30 kHz line rate. A detailed safety calculation based on ANSI Z136.1 – 2014 American National Standard for Safe Use of Lasers published by the Laser Institute of America is described previously [33, 92]. All experimental procedures and protocols were reviewed and approved by the UC Davis Institutional Review Board (IRB). A volumetric dataset with 512 a-lines and 200 b-scans each was acquired over a 5 mm range along the fast axis, with a total offset along the slow axis of 0.2 mm for speckle reduction [34]. The raw fringes were processed with linear wavenumber resampling, spatially dependent dispersion compensation [32], spectral shaping [34], Fourier transformation, and transverse and axial motion correction. Images were averaged prior to display.

4.6.8 Inter-spectrometer calibration using excess noise correlations

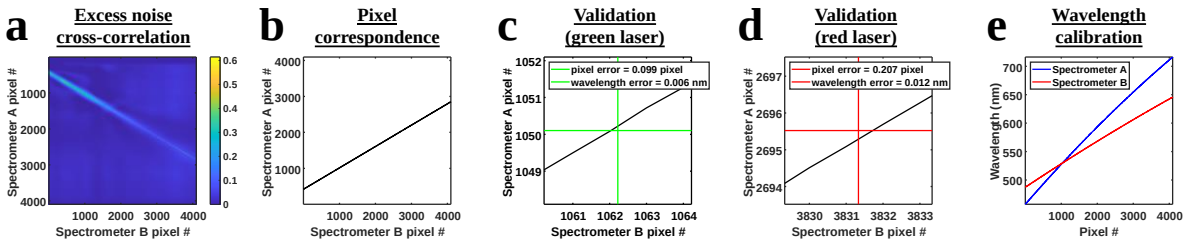

Figure 29. Excess noise cross-correlation can cross-calibrate spectrometers. a Excess noise cross-correlation matrix for two spectrometers with different spectral bandwidths: an already-calibrated spectrometer A (Figure 21 and Figure 25) and spectrometer B (see Section 4.6.7), which had to be calibrated de nuovo. b Pixel correspondence between the two spectrometers. For each spectrometer A pixel (row), the spectrometer B pixel that yields the largest normalized excess noise cross-correlation matrix value (a) corresponds best in wavelength. The spectrometer A pixel position of maximum correlation for each spectrometer B pixel was estimated using Gaussian fitting for subpixel accuracy. c and d The inter-spectrometer calibration was validated with a green (~532 nm) laser and a red (~635 nm) laser, respectively, with subpixel estimates of the centroids of the laser distributions. The errors calculated as the shortest distances in pixels to the validation values (cross centers in c-d) range from 10-21% of a pixel. The errors calculated by the difference in assigned wavelengths are 0.013 nm for both narrowband lasers. e Thus, using this method, given wavelength calibration of spectrometer A, spectrometer B can be accurately calibrated.

The spectral encoding provided by supercontinuum noise also aids the cross-calibration of multiple spectrometers (Figure 12e) via a cross-correlation matrix (Figure 29a). While the rows and columns of the autocorrelation matrix represent pixels of the same spectrometer, the rows and columns of the cross-correlation matrix represent pixels of different spectrometers, with correlations calculated from synchronous time courses (see Section 4.5.2). A high correlation indicates measurement of similar wavelengths. Therefore, for each pixel in one spectrometer, the pixel in the other with the maximum correlation is closest in wavelength (Figure 29b).

Inter-spectrometer calibration was validated by measuring the intensity distributions of narrowband green (~532 nm) and red (~635 nm) lasers on both spectrometers simultaneously. For each laser, the centroid was determined on both spectrometers, providing a subpixel correspondence that did not require knowledge of the exact wavelength. This two-point correspondence between spectrometers determined based on the narrowband lasers was compared to the comprehensive pixel-to-pixel correspondence from the excess noise correlation method (Figure 29c,d). The pixel error, defined as the distance from the two designated

corresponding points to the pixel calibration curve (Figure 29c,d), was much less than 1. The difference in the assigned wavelengths for the two spectrometers (Figure 29e) was 0.013 nm for both designated corresponding points.

The cross-calibration method does not, by itself, provide the absolute wavelengths of either spectrometer. However, this method can calibrate any spectrometer via another that was calibrated previously. For example, if the first spectrometer is calibrated and kept under controlled laboratory conditions while the second spectrometer is used in the field, the cross-calibration approach could be used to recalibrate the second spectrometer upon its return. We show that our method can calibrate a spectrometer *de nuovo* using another previously calibrated one via subpixel fitting and interpolation (Figure 29e). Moreover, even in the absence of an absolute calibration, cross-calibration may improve the reproducibility of measurements taken by different spectrometers. The cross-calibration method could eventually improve the performance of OCT systems that employ multiple spectrometers [46, 86].

4.7. Conclusions

This work, to our knowledge, presents a novel and useful application of excess intensity noise in optics. Unlike previous approaches for characterizing and calibrating spectrometers, our excess noise correlation method is computationally simple, comprehensive, and fast. It can be applied *in situ*, providing essential information to guide spectrometer alignment and determine the wavelength correspondence. This application benefits from higher levels of excess noise, which is characteristic of lower cost (lower repetition rate) supercontinuum sources. Notably, the idea fails with low noise sources based on pure self-phase modulation in nonlinear fibres and tungsten halogen lamps (see Section 4.6.2) but applies to amplified spontaneous emission sources (see Section 4.6.3). Though the finest measurable spectral resolution is ultimately limited by the intrinsic spectral correlations of the light source [75], such a limitation was not detectable with either superluminescent or supercontinuum sources at spectral resolutions of 0.05-0.15 nm (see Section 4.4.3). Our formalism can be modified to incorporate the intrinsic spectral correlations of the light source, if known, to mitigate this limitation (see Section 4.4.3). Moreover, a modified fitting approach

can exclude excess noise with a distinctly longer spectral correlation length to better isolate filtered incoherent noise to retrieve the spectral resolution (see Section 4.5.1).

After the invention of the laser, the observed speckle pattern was initially viewed as a hindrance. However, temporal speckle correlations were later found to solve many problems in optics, providing information about blood flow and particle size, while spatial speckle correlations provided information about the diffraction limit of imaging systems [96, 97]. Analogously, we hope that this work galvanizes the investigation of excess intensity noise correlations to solve other problems in optics.

Chapter 5: Predicting the SD-OCT PSF rolloff without an interferometer

5.1. Introduction

In spectral domain Optical Coherence Tomography (SD-OCT), spectrometer design and alignment are crucial for overall system performance. An optimal SD-OCT spectrometer considers the equivalent spectral width of the sensor pixel, dispersive element resolution, pixel cross-talk, and optical aberrations caused by imperfect lens design and misalignment of optical components within the spectrometer to minimize the coherence rolloff [72, 77, 93, 98]. Specifically, the results should be a narrow overall spectral resolution to minimize sensitivity rolloff and a wavenumber-invariant spectral resolution to minimize axial resolution rolloff [99, 100]. Currently, measuring this depth-dependent performance requires the labor-intensive process of acquiring datasets at many different path length mismatches by translating a mirror resulting in coherence rolloff measurements being used mostly as a display of spectrometer performance rather than a procedure used to aid the alignment process. Here, we propose an alternative to traditional rolloff acquisition methods that only requires a single time-course dataset of less than 0.25 seconds to enable easy monitoring of sensitivity and axial resolution rolloffs during the alignment process due to its computational and experimental simplicity. Unlike the traditional method, this method does not have a tradeoff between

axial sampling of the coherence rolloff and acquisition time so acquiring Point Spread Functions (PSF) at all path length mismatches within the imaging depth is feasible. Interestingly, our method does not require interference to predict the coherence rolloff and only requires incoherent excess noise of the light source [60, 79, 89], typically viewed as a hindrance. Here, we demonstrate our method using a visible light supercontinuum light source.

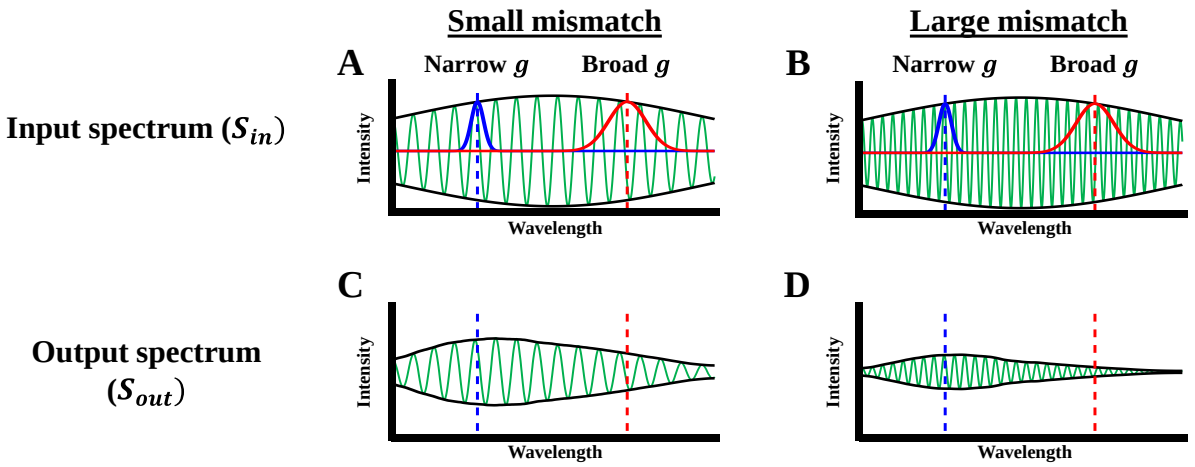

Figure 30. The effects of spectral resolution on the interference fringes with small path length mismatch (A,C) and large path length mismatch (B,D) between the sample and reference arms. A narrow spectral resolution (blue) causes minimal fringe attenuation while a boarder spectral resolution (red) causes significant fringe attenuation. Wavelength-varying spectral resolutions (blue and red) results in a fringe envelope (C,D) that does not resemble its intrinsic shape (A,B). The attenuation caused by the finite spectral resolution is greater with larger path length mismatches (B,D).

5.2. Theory

We assume that the spectrometer is a linear shift-variant system. The input spectrum is given by $S_{in}(\lambda)$. By the Weiner-Kinchine theorem, the field autocorrelation, or coherence rolloff, for a pixel measuring wavelength λ_{out}, is the inverse Fourier transform of the pixel-wise power spectral density, $PSD(\lambda_{out}, \Delta\lambda)$, where $\Delta\lambda = \lambda_{out} - \lambda$. We assume that λ_{out} is discretized due to sampling by spectrometer pixels. For a fixed λ_{out}, broader PSD widths in $\Delta\lambda$ lead to faster coherence rolloffs. To describe the spectrometer, we further define the impulse response, $g(\lambda_{out}, \Delta\lambda)$, which is the spectrometer photoelectric response at a

pixel corresponding to wavelength λ_{out}, to an impulsive input at wavelength λ, separated by $\Delta\lambda = \lambda_{out} - \lambda$. We then have that $PSD(\lambda_{out}, \Delta\lambda) = S_{in}(\lambda) g(\lambda_{out}, \Delta\lambda)$.

Note that while the pixel-wise PSD determines the OCT rolloff, the output spectrum, $S_{out}(\lambda_{out})$, measured across pixels, determines the axial resolution. Neglecting digitization, we may represent the measured spectrum, $S_{out}(\lambda_{out})$, in units of gray levels, as $S_{out}(\lambda_{out}) = \int PSD(\lambda_{out}, \Delta\lambda) d\Delta\lambda = \int S_{in}(\lambda) g(\lambda_{out}, \Delta\lambda) d\Delta\lambda$. Thus $S_{out}(\lambda_{out})$ is the superposition integral of the true spectrum input, $S_{in}(\lambda)$ and the impulse response. In some applications that use frequency combs, both S_{in} and g can contribute to the pixel power spectral density shape. More often, however, the spectrum S_{in} is smoothly varying on the scale of the spectrometer spectral resolution (determined by the second argument of g) and $PSD(\lambda_{out}, \Delta\lambda) \approx S_{in}(\lambda_{out}) g(\lambda_{out}, \Delta\lambda)$. In this common scenario, the second argument of the spectrometer response, $g(\lambda_{out}, \Delta\lambda)$, determines the power spectral density shape, and hence, the coherence rolloff, for each pixel.

In this work, we use the intrinsic excess noise of a supercontinuum light source as a probe to determine g and thus characterize the OCT system without an interferometer. For a zero-mean excess noise input (N_{in}) to the spectrometer, the zero-mean noise output is given by $N_{out}(\lambda_{out}) = \int N_{in}(\lambda) g(\lambda_{out}, \Delta\lambda) d\Delta\lambda = \int N_{in}(\lambda) g(\lambda_{out}, \lambda_{out} - \lambda) d\lambda$. We analyze second-order output excess noise statistics from the spectrometer:

$$\begin{aligned} &R_{excess,out}(\lambda_{out,1}, \lambda_{out,2}) = \left\langle N_{out}(\lambda_{out,1}) N_{out}(\lambda_{out,2}) \right\rangle = \\ &\iint R_{excess,in}(\lambda_1, \lambda_2) g(\lambda_{out,1}, \lambda_{out,1} - \lambda_1) d\lambda_1 g(\lambda_{out,2}, \lambda_{out,2} - \lambda_2) d\lambda_2 \end{aligned}, \tag{38}$$

where $R_{excess,in}(\lambda_1, \lambda_2) = \left\langle N_{in}(\lambda_1) N_{in}(\lambda_2) \right\rangle$ is the intrinsic correlation of the source spectrum, and $\langle \bullet \rangle$ is an ensemble average, estimated in this work by averaging over a time course.

Assuming that the excess noise is incoherent, or uncorrelated between wavelengths, we have that $R_{excess,in}\left(\lambda_1,\lambda_2\right)=\sigma^2\left(\lambda_1\right)\delta\left(\lambda_2-\lambda_1\right)$, where $\sigma^2\left(\lambda\right)$ is the wavelength-dependent variance, which is assumed to vary slowly on the scale of the spectral resolution. With this assumption, we approximate that

$$R_{excess,out}\left(\lambda_{out,1},\lambda_{out,2}\right)=\sigma^2\left(\frac{\lambda_{out,1}+\lambda_{out,2}}{2}\right)\int g\left(\lambda_{out,1},\lambda_{out,1}-\lambda_1\right)g\left(\lambda_{out,2},\lambda_{out,2}-\lambda_1\right)d\lambda_1 . \tag{39}$$

We can further simplify by substituting $\lambda_1^{'}=\lambda_{out,1}-\lambda_1$ and $\Delta\lambda=\lambda_2-\lambda_1$:

$$R_{excess,out}\left(\lambda_{out,1},\lambda_{out,2}\right)=\sigma^2\left(\frac{\lambda_{out,1}+\lambda_{out,2}}{2}\right)\int g\left(\lambda_{out,1},\lambda_1^{'}\right)g\left(\lambda_{out,2},\lambda_1^{'}+\lambda_{out,2}-\lambda_{out,1}\right)d\lambda_1^{'} . \tag{40}$$

We immediately recognize the integral as a cross-correlation, enabling us to write,

$$R_{excess,out}\left(\lambda_{out,1},\lambda_{out,2}\right)=\sigma^2\left(\lambda_{avg}\right)g\left(\lambda_{out,1},\Delta\lambda\right)\star g\left(\lambda_{out,2},\Delta\lambda\right), \tag{41}$$

where $\lambda_{avg}=\frac{\lambda_{out,1}+\lambda_{out,2}}{2}$, $\Delta\lambda=\lambda_{out,2}-\lambda_{out,1}$, and $\star$ denotes the cross-correlation with respect to $\Delta\lambda$.

Assuming g varies slowly in its first argument relative to its second argument, we obtain

$$R^{'}_{excess,out}\left(\lambda_{avg},\Delta\lambda\right)=\sigma^2\left(\lambda_{avg}\right)g\left(\lambda_{avg},\Delta\lambda\right)\star g\left(\lambda_{avg},\Delta\lambda\right), \tag{42}$$

where for convenience, we have replaced $R^{'}_{excess,out}\left(\lambda_{avg},\Delta\lambda\right)=R_{excess,out}\left(\lambda_{avg}-\Delta\lambda/2,\lambda_{avg}+\Delta\lambda/2\right)$. Above we argued that by the Weiner-Kinchine theorem, the coherence roll-off Γ is the inverse Fourier transform of the PSD, which is proportional to g. More specifically, assuming that $\Delta\lambda=-\frac{\lambda_{avg}^{\ 2}}{2\pi}\Delta k$, and taking an inverse Fourier transform with respect to Δk, we obtain

$$\Gamma(\lambda_{avg},z)=\frac{\int g\left(\lambda_{avg},-\frac{\lambda_{avg}^{\ 2}}{2\pi}\Delta k\right)\exp\left(j2\Delta kz\right)d\Delta k}{\int g\left(\lambda_{avg},-\frac{\lambda_{avg}^{\ 2}}{2\pi}\Delta k\right)d\Delta k}, \tag{43}$$

where the normalization in the denominator ensures $\Gamma(\lambda_{avg},0)=1$. However, as per Eq. (42), $R'_{excess,out} \sim g \star g$, not g, is experimentally accessible. By the autocorrelation property of the Fourier transform, $|\Gamma|^2$ Fourier transforms to $g \star g$. Thus, we take an inverse Fourier transform of $R'_{excess,out}$, and take the square root. We obtain the roll-off as:

$$\left|\Gamma(\lambda_{avg},z)\right| = \sqrt{\frac{\left|\int R'_{excess,out}\left(\lambda_{avg},-\frac{\lambda_{avg}^{\ 2}}{2\pi}\Delta k\right)\exp(j2\Delta kz)d\Delta k\right|}{\int R'_{excess,out}\left(\lambda_{avg},-\frac{\lambda_{avg}^{\ 2}}{2\pi}\Delta k\right)d\Delta k}}, \tag{44}$$

where, again, normalization in the denominator ensures $\left|\Gamma(\lambda_{avg},0)\right|=1$.

Our experimental setup cannot readily observe $R_{excess,out}$, free from shot noise and detector noise. To distinguish between these different noise sources, we parametrically acquire time courses at different intensity levels, $N_{tot,out}(\lambda_1,t,\alpha)$, where α is an attenuation parameter. We then obtain the autocorrelation matrix

$$R_{tot,out}(\lambda_{out,1},\lambda_{out,2},\alpha) = \left\langle N_{tot,out}(\lambda_{out,1},t,\alpha)N_{tot,out}(\lambda_{out,2},t,\alpha)\right\rangle_t. \tag{45}$$

We assume that this matrix can be written as

$$R_{tot,out}(\lambda_{out,1},\lambda_{out,2},\alpha) = R_{detector}(\lambda_{out,1},\lambda_{out,2}) + R_{shot}(\lambda_{out,1},\lambda_{out,2}) + R_{excess,out}(\lambda_{out,1},\lambda_{out,2}). \tag{46}$$

The first matrix represents detector noise, the second matrix represents shot noise, and the third matrix represents excess noise. We assume that the shot noise matrix is zero except along the diagonal, where

$$R_{shot}(\lambda_{out},\lambda_{out}) = \left(\frac{2^{BD}}{FWC}\right)S_{out}(\lambda_{out},\alpha), \tag{47}$$

where the coefficient in parentheses depends on the full well capacity (FWC) and the bit depth (BD). We also assume that

$$R_{excess,out}\left(\lambda_{out,1},\lambda_{out,2}\right)=r_{excess,out}\left(\lambda_{out,1},\lambda_{out,2}\right)S_{out}\left(\lambda_{out,1},\alpha\right)S_{out}\left(\lambda_{out,2},\alpha\right), \quad (48)$$

where $r_{excess,out}\left(\lambda_{out,1},\lambda_{out,2}\right)$ is the unitless spectrum-normalized excess noise auto-correlation. With this normalization, $r_{excess,out}\left(\lambda_{out,1},\lambda_{out,1}\right)$ is the excess noise coefficient.

5.3. Method

5.3.1 Point spread function estimation

A previously described visible light OCT spectrometer [32] was used with a supercontinuum light source (EXW-12, NKT Photonics). Spectral intensity time courses are acquired at 70 kHz line rate and near saturation of sensor pixels to maximize excess noise. To quantify the extent of the correlations between pixels, we perform the auto-correlation of the time courses in respect to wavelength. The method was previously described in Chapter 4. The auto-correlation matrix includes contributions from not only excess noise, but also shot noise and detector noise. Shot noise is corrected along the diagonal through the assumption that shot noise follows a Poisson distribution and therefore the mean photon count is equal to its variance. The variance in a given pixel can be estimated from the camera gray level, full well capacity, and bit depth. Detector noise, comprised of dark noise and read noise, is corrected by subtraction of the autocorrelation matrix from data acquired with no light on the camera. After these corrections, we are left with the excess noise auto-correlation matrix, $R'_{excess,out}\sim g\star g$ (Figure 32A).

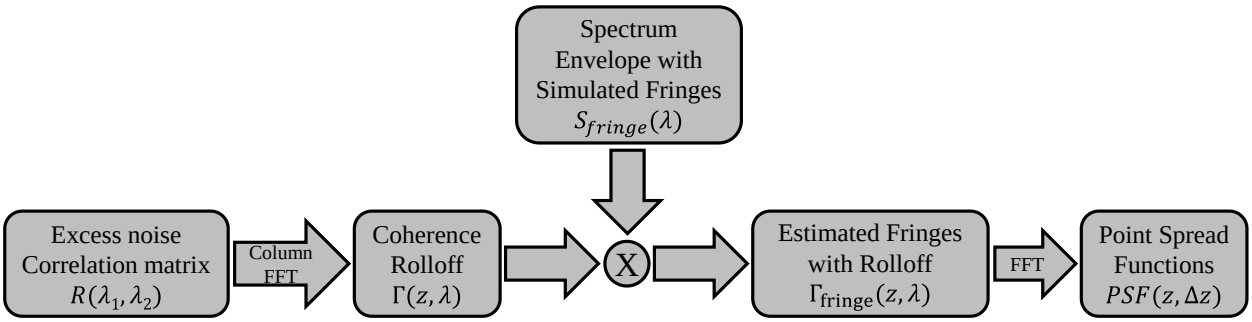

Figure 31. Block diagram of the point spread function estimation method using excess noise correlations.

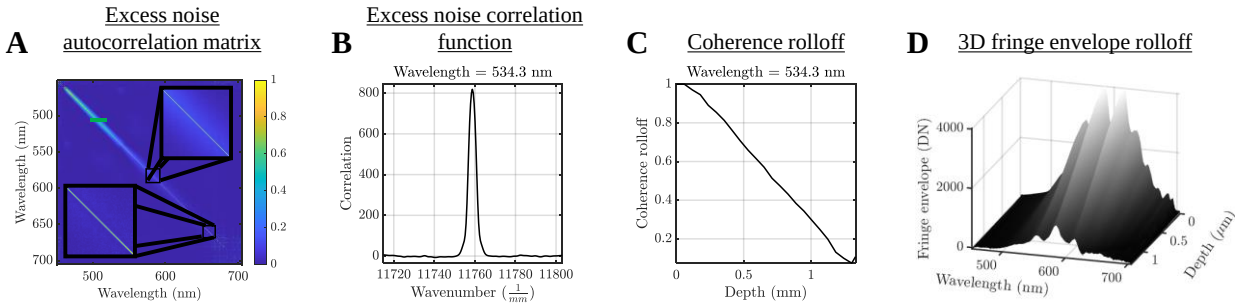

Figure 32. (A) The excess noise autocorrelation matrix with zooms showing the quasi diagonal has varying width dependent on the spectral resolution. (B) Each row in (A) is the excess noise correlation function at the specified wavelength. The function is plotted to be linear in wavenumber. (C) Fourier transform of the excess noise correlation function yields the coherence rolloff function. The function is normalized to the value at zero depth. (D) The fringe envelop rolloff is the multiplication of the coherence rolloff with the spectra.

As mentioned in section 5.2, the coherence rolloff, $\Gamma(z, \lambda)$, is the inverse Fourier transform of the pixel-wise power spectral density, correlated with spectrometer photoelectric response, g. Assuming a slowly varying spectrum, S_{in}, on the scale of the photoelectric response, we can find the coherence rolloff (Figure 32C) through the square root of the fast Fourier transform (FFT) along the columns of the excess noise auto-correlation matrix (Figure 32B), uniformly sampled in wavenumber (Figure 31). The coherence rolloff is normalized to zero-delay for all wavenumbers (Figure 32C). To predict both the sensitivity and axial resolution rolloffs, we simulate the intrinsic interference fringes, $S_{fringe}(\lambda)$, for all path length mismatches using the spectrum shape obtained from time courses. The generated fringes are multiplied with the normalized coherence rolloff (Figure 31) to obtain the estimated fringes with rolloff, $\Gamma_{fringe}(z, \lambda)$, (Figure

32D) and Fourier transformed to obtain the PSFs at all depths, $PSF(z, \Delta z)$, similar to what would be acquired by traditional rolloff measurements.

5.4. Results

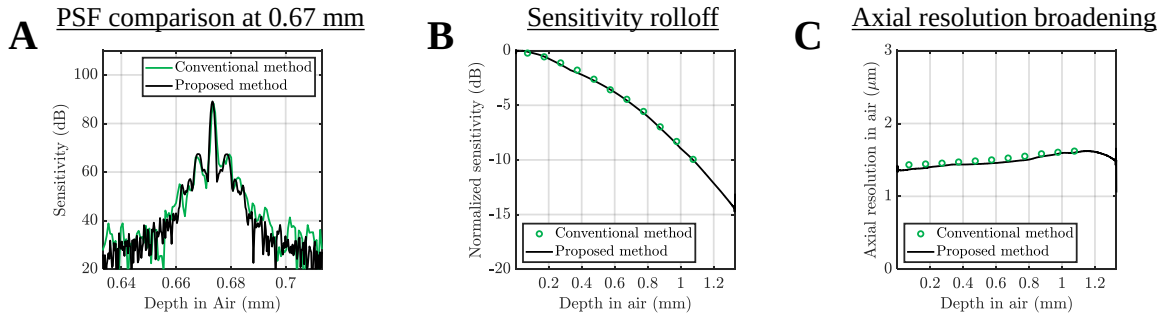

Figure 33. The PSF functions' shapes (A), sensitivity (B), and axial resolution (C), obtained with the excess noise correlation method (green) were compared to those obtained from the traditional method (black).

The sensitivities and axial resolutions were measured for the estimated PSFs, $PSF(z, \Delta z)$, at all depths. Results were compared with sensitivities and axial resolutions of the PSFs measured using the traditional method of moving a mirror in the reference arm between acquisitions (Figure 33). There was good agreement between the two methods, demonstrating that the PSFs at all path length mismatches within the imaging range can be accurately estimated using excess noise correlations.

5.5. Conclusions

The excess noise correlation method was extended to predict the PSFs positioned at all imaging depths using a single time course dataset and with no additional manual labor. This method can significantly speed up the OCT system characterization process and provides an additional application of excess noise correlations.

Chapter 6: Excess noise suppression using balanced detection in visible light OCT

6.1. Introduction

Supercontinuum sources for visible light spectral domain OCT (SDOCT) are noisy and often expensive. Balanced detection can reduce excess noise, but is rarely used in SDOCT. Here, we show that balanced detection can achieve effective excess noise cancellation across all depths if two linear array spectrometers are spectrally well-matched. We propose excess noise correlation matrices as tools to achieve such precise spectral matching. Using optomechanical adjustments, while monitoring noise correlations, we proactively match wavelength sampling of two different spectrometers to just a few picometers in wavelength, or 0.001% of the overall spectral range. We show that proactively-matched spectrometers can achieve an excess noise suppression of more than two orders-of-magnitude in balanced visible light OCT, outperforming simple retrospective software calibration of mismatched spectrometers. High noise suppression enables visible light OCT of the mouse retina at 70 kHz with 125 microwatts incident power, with an inexpensive, 30 MHz repetition rate supercontinuum source. Averaged images resolve the retinal pigment epithelium in a highly pigmented mouse strain.

Light source noise degrades optical imaging, metrology, and information transmission. Typically, “excess” noise is defined as noise in excess of, or in addition to, shot noise, which arises from the quantum nature of light. Though not as fundamental as shot noise, excess noise is intrinsic to some mechanisms of light generation, including, for instance, thermal light [76] and supercontinua [101]. To achieve performance limited by shot noise at the detector, approaches to mitigate excess noise are often employed, such as light source engineering [79, 102, 103] and careful choice of system operating point [78, 104].

Balanced detection [78, 105] is a popular hardware approach that can mitigate excess noise. Balancing has been applied in fields like optical frequency domain reflectometry [78, 105] and Optical Coherence Tomography (OCT) imaging [106]. Balancing takes advantage of the phase shifts between the two crossed

channels of an interferometer, which yields an interferometric phase shift of π. Thus, if the signals in the two detection arms of a balanced interferometer are subtracted, the excess (common mode) noise is ideally eliminated, along with D.C. and autocorrelation (self-interference) terms, the shot noise variance is doubled, and the interferometric signal (cross-interference term squared) is quadrupled.

Balanced detection is the standard practice in swept source OCT (SSOCT) [107], where high excess noise is driven by wide SSOCT detection bandwidths (several orders of magnitude higher than the a-line rate) and amplified spontaneous emission in rapidly tunable lasers [108]. In the field of spectral domain OCT (SDOCT), balancing is rarely used [109]. This is because SDOCT typically uses a linear array spectrometer with lower detection bandwidths (on the order of the a-line rate) and relatively low noise superluminescent diode sources, making it easier to achieve the shot noise limit [110]. SDOCT approaches for balanced detection have been presented; yet in many cases, since each detection arm was already operating close to the shot noise limit [111-113], these works achieved the shot noise limit without requiring stringent noise cancellation.

Visible light OCT is an emerging area of SDOCT with unique capabilities for ultrahigh resolution imaging and spectroscopy [21, 22, 25, 26, 30, 34, 114]. In visible light OCT, broadband supercontinuum sources are most often used, with typical excess noise coefficients more than two orders-of-magnitude larger than SLDs [52]. Inexpensive supercontinuum sources with longer seed pulses or lower repetition rates [60, 115] are generally noisier, and employed less often in SDOCT. Most supercontinuum sources do not reach the shot noise limit in SDOCT, with rare exceptions [103]. In the field of visible light OCT, the resulting high cost and poor performance have prevented widespread adoption. Recently, a normalization scheme was proposed for visible light OCT, which requires acquisition of a separate reference spectrum [115] for each pulse. Although this study showed excess noise suppression, it still deviated from the shot noise limit. Better dual balancing could enable the use of noisier, less expensive supercontinuum sources, driving down the net system cost of visible light OCT.

Noise suppression in balanced OCT is challenged by asymmetries in the two detection arms. For single wavelength systems, asymmetry may result from imbalances in the detected power, while in broadband systems, power imbalances may vary across the spectrum. While the detriment of power imbalance is well-appreciated [112, 116], the importance of matching spectral sampling and resolution in balanced SDOCT has not been explored.

Here, we show that spectral matching is critical in demanding applications such as high-speed visible light OCT imaging with noisy light sources. We present a formalism for balanced SDOCT, and use it to illustrate the theoretical benefits of spectral matching. We then present a proactively matched, dual-balanced visible light OCT system. To yield identical spectral resolution and wavelength sampling, we use excess noise correlations as a tool to proactively co-align two spectrometers, achieving a residual error (root mean squared deviation) of just 0.04 pixels across a 4096 pixel spectral range. Proactive matching is contrasted with a simple retrospective approach, wherein two existing spectrometers are calibrated in software [117]. With the proactive matching approach, we achieve an overall excess noise suppression of more than two orders of magnitude with a relatively inexpensive, 30 MHz repetition rate supercontinuum source, enabling imaging of the mouse retina at a 70 kHz a-line rate and 125 microwatts incident power.

6.2. Theory

This section first presents a formalism for balancing based on linear operations or matrix multiplications. This formalism is then used to highlight the detrimental effects of mismatches in spectral sampling or resolution. Finally, this section concludes that precise spectral matching is required for effective balancing.

6.2.1 Balancing formalism

In spectral domain OCT, balancing is performed digitally, often in software, on the raw digitized values from two different spectrometers [111, 118-121]. We represent the signals from these two spectrometers (denoted as A and B) as vectors $\vec{s}_A$ and $\vec{s}_B$, with elements of the vectors representing spectrometer pixels. We compute the balanced signal, $\vec{s}_{A-B}$, as the difference of $\vec{s}_A$ and a linear operation on $\vec{s}_B$, i.e.

$\vec{s}_{A-B} = \vec{s}_A - H\vec{s}_B$, where H is a real matrix that defines the linear operation. In other words, the ith pixel in spectrometer A is approximated as a linear superposition of pixels in spectrometer B, where the coefficients of the linear superposition are the ith row of H. The matrix H can implement an interpolation of spectrometer pixels (to account for pixel offsets in wavelength), as well as a scaling of spectrometer pixels (to account for asymmetries in coupling to the two detection arms, for instance). To clearly separate these scaling and interpolation operations, we write $H = SI_{AB}$, where S is a diagonal scaling matrix and I_{AB} is the interpolation (resampling) matrix, whose row sum is 1 (Figure 34). An alternative formulation where scaling occurs before interpolation is also possible. Note that while scaling can improve suppression of excess noise, it does worsen the shot noise limited sensitivity, akin to spectral shaping [122]. Scaling has previously been discussed [112, 116], and is not the primary focus of this work.

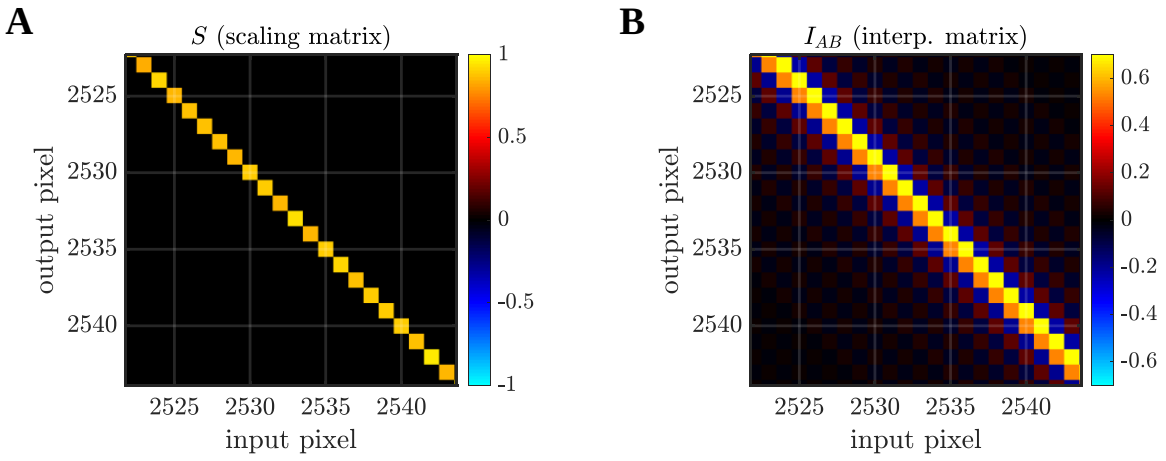

Figure 34. The H matrix, or balancing matrix, can be decomposed as the product of two matrices, $H = SI_{AB}$, where S is a diagonal scaling matrix and I_{AB} is an interpolation matrix whose row sum is 1. Balancing is then performed as $\vec{s}_{A-B} = \vec{s}_A - H\vec{s}_B$, where $\vec{s}_A$ and $\vec{s}_B$ represent data from spectrometers A and B, respectively. Portions of scaling (A) and interpolation (B) matrix constructed by DFT upsampling are shown.

6.2.2 Optimal balancing

What level of excess noise suppression is achievable? In this section, we argue that the optimal H for excess noise cancellation, and ultimately, best achievable noise suppression, depend on the degree of

matching of the two spectrometers. Thus, the post-processing algorithm (i.e., H) should not be a passive choice that is made after the system is built. Rather, the optimization of post-processing should be a consideration that proactively guides system alignment.

The optimal H to minimize residual excess noise can be readily derived. To determine the maximal level of noise suppression, we consider just excess noise outputs of each spectrometer $\vec{n}_A$ and $\vec{n}_B$, with cross-correlation matrix $R_{AB} = \langle \vec{n}_A (\vec{n}_B)^T \rangle$ and autocorrelation matrices $R_{AA} = \langle \vec{n}_A (\vec{n}_A)^T \rangle$ and $R_{BB} = \langle \vec{n}_B (\vec{n}_B)^T \rangle$, respectively, where $\langle \ldots \rangle$ denotes expectation. Here, we recognize that balancing can be reformulated as an estimation of excess noise in spectrometer A, $\hat{\vec{n}}_A$, given observations of excess noise in spectrometer B, $\vec{n}_B$, i.e. $\hat{\vec{n}}_A = H\vec{n}_B$. The linear minimum mean squared error (LMMSE) estimate which minimizes the sum of squared errors $\left\langle \left(\hat{\vec{n}}_A - \vec{n}_A \right)^2 \right\rangle$ across pixels is given by $H = R_{AB}(R_{BB})^{-1}$. The LMMSE estimate is identical to a finite impulse response Wiener filter for a discrete series [123, 124]. The LMMSE estimator is also the optimal estimator (in the sense of minimizing the mean squared error) if the excess noise is Gaussian. Note that the LMMSE estimate is designed to maximize the degree of excess noise cancellation, irrespective of the other noise sources, and therefore serves as a useful benchmark for all other balancing methods (i.e., other choices of H).

The autocorrelation matrix of excess noise after dual balancing, in $\vec{n}_{A-B} = \vec{n}_A - H\vec{n}_B$, is $R_{(A-B)(A-B)} = \langle \vec{n}_{A-B} (\vec{n}_{A-B})^T \rangle = R_{AA} - R_{AB}H^T - H\left(R_{AB}\right)^T + HR_{BB}H^T$. Noting that $R_{BA} = \left(R_{AB}\right)^T$, we find that $R_{(A-B)(A-B)} = R_{AA} - R_{AB}(R_{BB})^{-1}R_{BA}$ for the LMMSE estimator. The residual excess noise variance after balancing is given by the trace of the matrix $R_{(A-B)(A-B)}$.

6.2.3 Detector and shot noise

The detector noise and shot noise autocorrelations are readily obtained in our formalism. If detector noise is uncorrelated between the two spectrometers, the detector noise autocorrelation after balancing is given

by $R_{det,(A-B)(A-B)} = R_{det,AA} + HR_{det,BB}H^T$. As shot noise is uncorrelated between pixels and between spectrometers, the shot noise autocorrelation after balancing is given by $R_{shot,(A-B)(A-B)} = R_{shot,AA} + HR_{shot,BB}H^T$, where $R_{shot,AA}$ and $R_{shot,BB}$ are diagonal matrices with the reference spectrum multiplied by a conversion factor along the diagonal. As with excess noise, the detector and shot noise variances after balancing are given by the traces of their respective autocorrelation matrices. The detector and shot noise variances after Fourier transformation are given by the diagonals of $FR_{det,(A-B)(A-B)}F^\dagger$ and $FR_{shot,(A-B)(A-B)}F^\dagger$, respectively, where F is the DFT matrix and † represents the conjugate-transpose. Note that balancing can lead to a non-diagonal shot noise autocorrelation, and consequently, a shot noise floor that varies with depth. While the shot noise and detector noise should be considered in analyzing the system sensitivity, our primary focus in this work remains on excess noise suppression. Thus, we subtract detector and shot noise estimates to isolate just excess noise.

6.2.4 Excess noise elimination

Importantly, R_{AB}, R_{AA}, and R_{BB} can be actively modified through the alignment process. We observe that excess noise (trace of $R_{(A-B)(A-B)}$) can be completely eliminated if $R_{AA} = R_{AB}(R_{BB})^{-1}R_{BA}$. One way to achieve this is $R_{AB} = \Sigma_A R \Sigma_B$, $R_{AA} = \Sigma_A R \Sigma_A$, and $R_{BB} = \Sigma_B R \Sigma_B$, where Σ_A and Σ_B are diagonal matrices with positive elements and R is a positive definite autocorrelation matrix. This can be achieved if both spectrometers are matched and sample the same wavelengths with the same spectral resolutions. The autocorrelation matrices then differ only in scaling, which is described by diagonal matrices Σ_A and Σ_B. Applying the LMMSE estimator with matched alignment leads to a diagonal H matrix, or $H = \Sigma_A(\Sigma_B)^{-1}$, which is a pure scaling operation with $S = \Sigma_A(\Sigma_B)^{-1}$. Note that with perfect matching, I_{AB} becomes the identity matrix, which implies no interpolation is needed.

6.3. Simulations

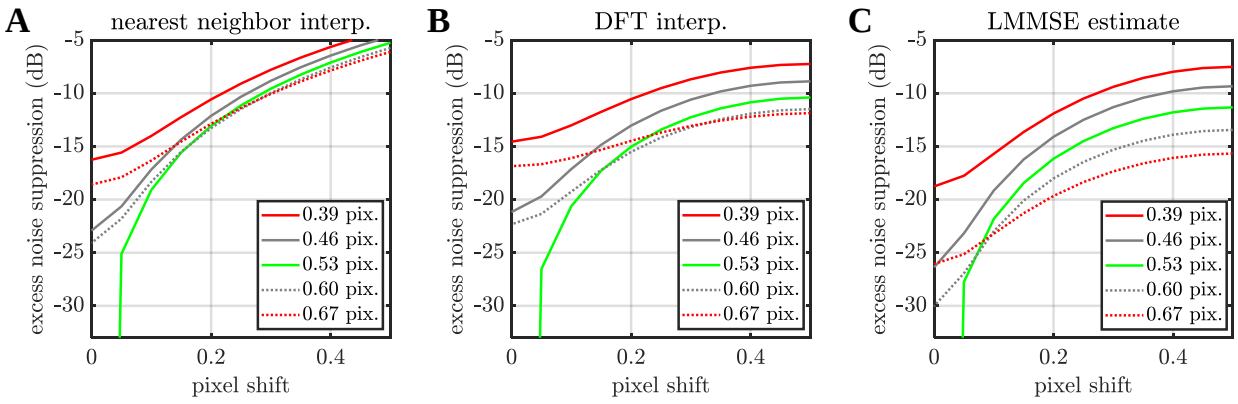

Figure 35. Balancing simulations, with a spectrometer A resolution of 0.53 pixels, show that only by matching pixel sampling (i.e. a pixel shift of 0 pixels) and spectral resolution (i.e. a spectrometer B resolution of 0.53 pixels) can excess noise elimination be achieved. With spectrometer matching, all methods converge as interpolation becomes unnecessary and I_{AB} approaches the identity matrix. Balancing based on the linear minimum mean squared error (LMMSE) estimate (C) consistently outperforms both nearest neighbor and DFT interpolation (A-B), as expected. The spectrometer B resolution is shown in the legends.

The previous section showed theoretically that matched spectrometers enable excess noise elimination. To assess performance with imperfect matching, we next simulated balancing of two spectrometers (Figure 35), based on the formalism in Sections 6.2.1 and 6.2.2. We assumed that spectrometer A had a Gaussian spectral resolution of 1.06 pixels full width at half maximum (FWHM). We simulated varying spectrometer B sampling error (from 0 to 0.5 pixels) and spectral resolution (0.78-1.34 pixels FWHM). For simulations we assumed purely incoherent source excess noise [52]; therefore, the autocorrelation matrix was determined solely by the spectral resolution. We also considered the excess noise suppression as a function of axial image depth, as well as the point spread function (PSF) rolloff and shot noise rolloff. We tested nearest neighbor interpolation (equivalent to no interpolation or I_{AB} equal to the identity matrix for pixel shifts below 0.5), and Discrete Fourier Transform (DFT) upsampling, benchmarking all approaches against the linear minimum mean squared error (LMMSE) estimator [125]. Note that balancing with scaling and

nearest neighbor or no interpolation requires only P multiplications, where P is the number of spectrometer pixels, whereas other balancing methods may require up to P^2 multiplications.

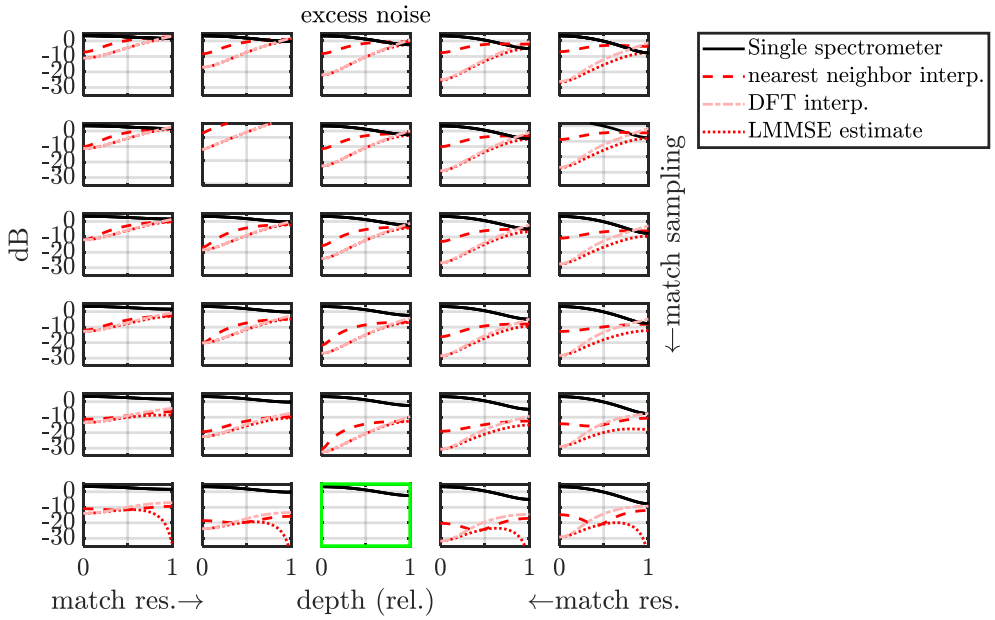

Figure 36. Residual excess noise of simulated balancing as a function of pixel mismatch and spectral resolution. Rows represent decreasing pixel shifts from 0.5 pixels (mismatched, top row) to 0.0 pixels (matched, bottom row). Columns represent worsening spectrometer B spectral resolution, from 0.39 pixels (mismatched, left column) to 0.53 pixels (matched, center column) to 0.67 pixels (mismatched, right column). Note that the LMMSE estimator outperforms nearest neighbor and DFT interpolation at all depths. Note that the residual noise after balancing matched spectrometers (green box) is zero, or negative infinity on a dB (logarithmic) scale.

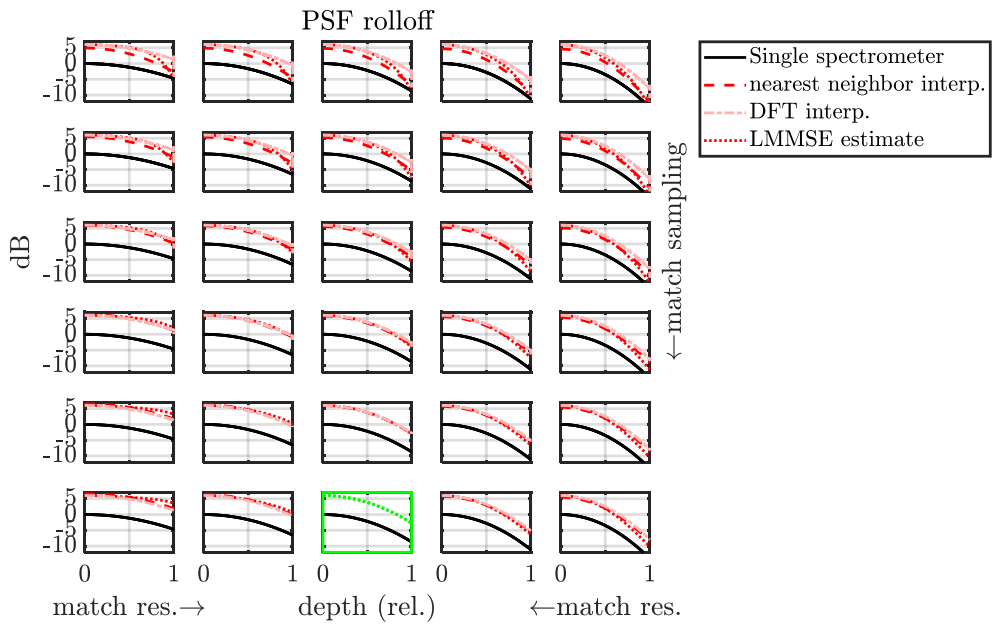

Figure 37. Point spread function (PSF) rolloff of simulated balancing as a function of pixel mismatch and spectral resolution. Rows represent decreasing pixel shifts from 0.5 pixels (mismatched, top row) to 0.0 pixels (matched, bottom row). Columns represent worsening spectrometer B spectral resolution, from 0.39 pixels (mismatched, left column) to 0.53 pixels (matched, center column) to 0.67 pixels (mismatched, right column). Note that differences in the PSF rolloff of the LMMSE estimate (dotted lines) tend to be offset by differences in shot noise (Error! Reference source not found.**). For matched spectrometers (green box) the balanced PSF rolloff exceeds the single spectrometer PSF rolloff by 6 dB.**

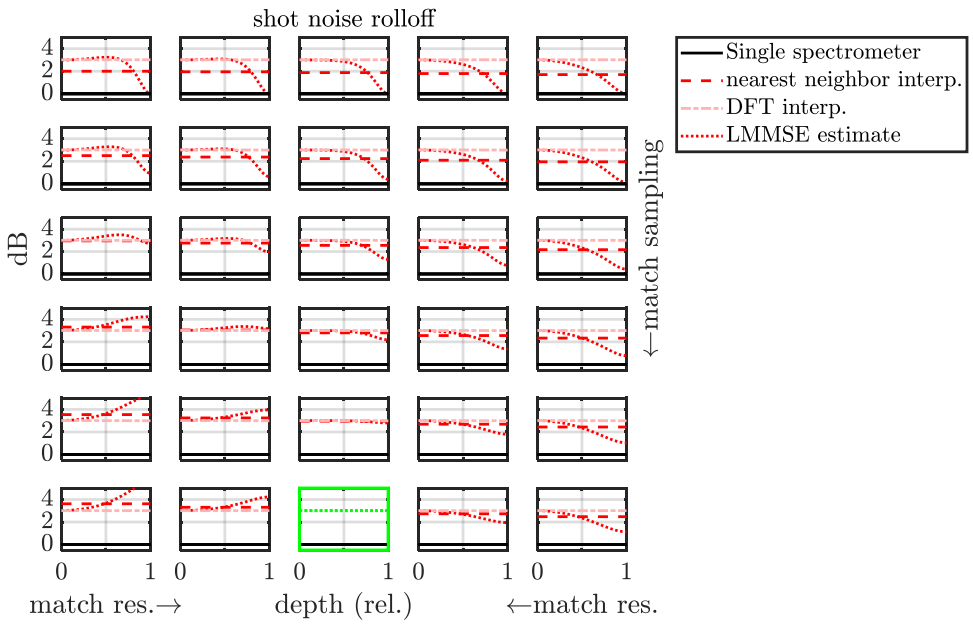

Figure 38. Shot noise rolloff of simulated balancing as a function of pixel mismatch and spectral resolution. Note that the shot noise level is not necessarily invariant with depth after balancing. Rows represent decreasing pixel shifts from 0.5 pixels (mismatched, top row) to 0.0 pixels (matched, bottom row). Columns represent worsening spectrometer B spectral resolution, from 0.39 pixels (mismatched, left column) to 0.53 pixels (matched, center column) to 0.67 pixels (mismatched, right column). For matched spectrometers (green box) the balanced shot noise exceeds the single spectrometer shot noise by 3 dB.

As predicted in the previous section, simulations showed that excess noise elimination (no residual excess noise) could only be achieved if spectral resolution and pixel sampling are matched (Figure 35). The ability to suppress excess noise degraded significantly by orders of magnitude with even a fraction of a pixel mismatch. The LMMSE estimator achieved the best excess noise suppression, as expected, but changed the shot noise and signal rolloff characteristics. Yet, we found that a steeper PSF rolloff of the LMMSE estimate tended to be counterbalanced by a steeper shot noise rolloff. Discrete Fourier Transform (DFT) upsampling interpolation had sub-optimal excess noise suppression, but did not affect the shot noise or signal rolloff. For matched spectrometers with a purely diagonal H (i.e., I_{AB} is the identity matrix), the PSF rolloff of the balanced signal was equivalent to the single spectrometer rolloff.

With a mismatch of pixel sampling, even with matched spectral resolutions, the excess noise suppression degraded markedly with depth. This makes sense because with sampling errors, it becomes harder to suppress high frequency excess noise components. Since rapidly varying signals along the spectrometer are mapped to deeper depths by the Fourier transform operation in SDOCT, such sampling errors lead to more residual excess noise at larger depths.

In summary, simulations revealed that precise sub-pixel matching is required to achieve a level of excess noise suppression exceeding 20 dB in magnitude. Since our spectrometer pixel size was just 10 micrometers, sub-pixel precision cannot be achieved by relying on standard spectrometer manufacturing tolerances. In the next section, we describe a new, proactive optomechanical matching approach to achieve such sub-pixel alignment of two different spectrometers for the first time.

6.4. Methods

6.4.1 Balanced visible light OCT system

We built a balanced visible light OCT system to achieve pixel matching, as shown in Figure 39. A visible light OCT reference arm and sample arm from a previously-reported [32] *in vivo* mouse retinal imaging system were employed. Relative to previous work, the system was improved and upgraded for dual balancing by adding a 90/10 fiber coupler in the source path, a pair of new spectrometers, and a less expensive, low repetition rate supercontinuum light source, all reported here for the first time. A 50/50 beamsplitter ensured that the returning reference light was split approximately evenly between the two detection paths, although the spectrometer A path incurred an additional 10% loss caused by the 90/10 coupler (Figure 39). The new spectrometers each employed a 101.6 mm focal length reflective collimator lens (MPD249-P01, Thorlabs), a 1000 lpmm (line per millimeter) volume transmission grating (Wasatch Photonics), a custom 217.7 mm focal length focusing lens, and a complementary metal-oxide semiconductor line scan camera (SPL 8192-70km, Basler) with two lines of 10 micrometer pixels, operated in vertical binning mode. The cameras were mounted to five-axis alignment stages (9081, Newport). To

push the limits of the excess noise suppression, we utilized a noisier and cheaper supercontinuum light source (WhiteLase Micro, NKT Photonics) with a low repetition rate of 30 MHz. This is almost an order of magnitude lower than the state-of-the-art low noise sources with a 320 MHz repetition rate that enables averaging of pulse-to-pulse fluctuations during the exposure time [103]. Brown et al. previously concluded that a similar source, originally sold by Fianium, resulted in high excess noise levels [60]. Thus, the chosen source is a prime candidate for demonstrating the improvement of balancing. With 4096 pixels, the system attained a spectral range of 173 nm. A center wavelength of 628 nm, 1.2 μm axial resolution in tissue, 70 kHz imaging speed, and 3.7 dB sensitivity rolloff over 1 mm in air were achieved. Note that each spectrometer achieved a rolloff comparable to our previous best-reported system [117]. We determined the dual balanced sensitivity to be 87 dB at a depth of 100 μm, with a power of 125 μW, at an a-line rate of 70 kHz (see below). Typically, it is assumed that supercontinuum pulses are independent. This assumption implies that the excess noise coefficient is inversely proportional to the number of pulses during the exposure. Likewise, the measurement of different pulses by each spectrometer will limit excess noise suppression. Thus, precise temporal synchronization is also required. For example, for a desired noise suppression of 20 dB in magnitude, leaving one part in a hundred residual excess noise, synchronization to <<1% of the exposure time is needed. This requires matched paths from the 50/50 beam splitter to each spectrometer, as well as precise triggering.

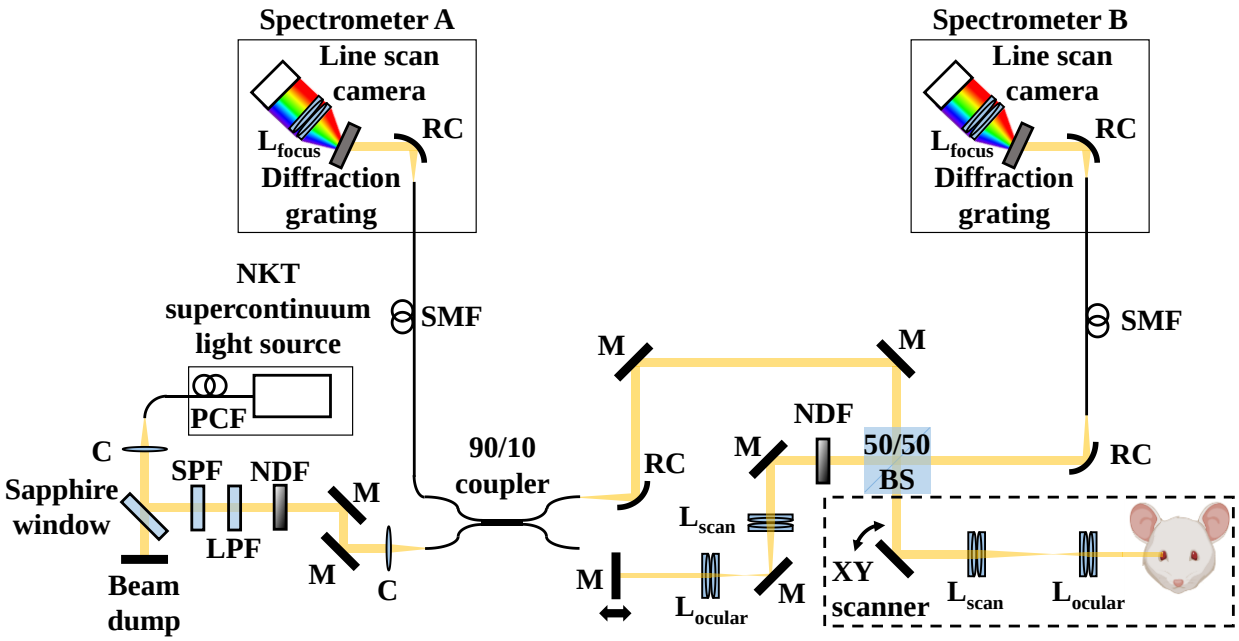

Figure 39. Schematic diagram of visible light OCT system with balanced detection. PCF: photonic crystal fiber, C: collimator, SPF: short pass filter, LPF: long pass filter, NDF: neutral density filter, M: mirror, SMF: single mode fiber, RC: reflective collimator, L_{scan}: scan lens, L_{ocular}: ocular lens, L_{focus}: focusing lens, BS: beamsplitter.

6.4.2 Proactive spectrometer matching

We next endeavored to achieve spectrometer matching through proactive alignment based on excess noise correlation matrices [52]. With incoherent excess noise, each source wavelength essentially has its own unique fluctuation pattern, or fingerprint. The quasi-diagonal of an auto-correlation matrix is defined as the portion where row and column measure overlapping source wavelengths, yielding high correlation values. The quasi-diagonal of the excess noise autocorrelation matrices, R_{AA} and R_{BB}, provides information about spectral resolution (characterization [52]), and the excess noise cross-correlation matrix, R_{AB}, provides information about pixel correspondence between spectrometers (cross-calibration [52]). The present work extends previous work [52] by employing correlation matrices as tools to proactively aid alignment.

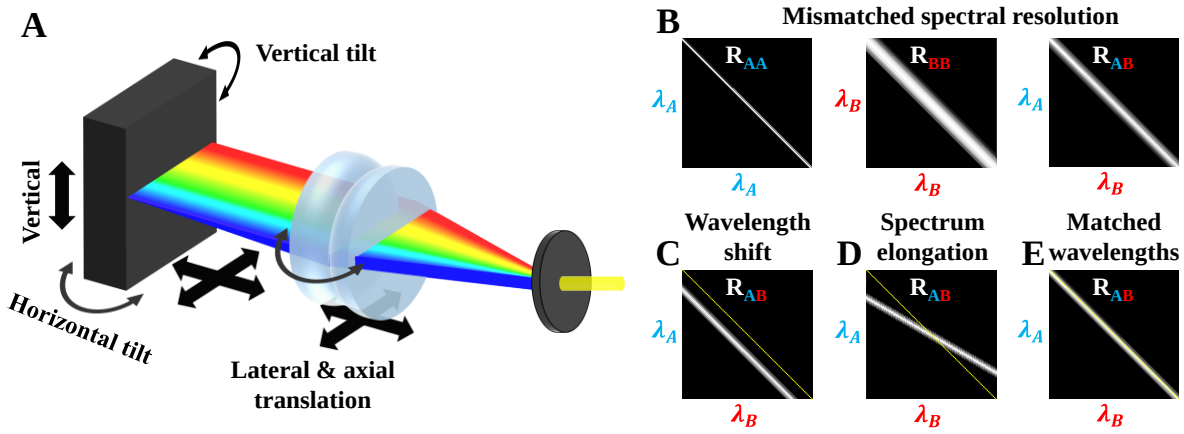

Figure 40. (A) Diagram of a single spectrometer showing available degrees of freedom for alignment. (B-E) Images of autocorrelation (R_{AA} and R_{BB}) and cross-correlation (R_{AB}) matrices for different hypothetical alignments. B) Mismatched spectral resolution: narrower R_{AA} quasi-diagonal width, indicative of a finer spectral resolution for spectrometer A than for spectrometer B. (C) Wavelength shift: shift of the quasi-diagonal of R_{AB} , indicative of a pure shift of spectra between spectrometers. (D) Spectrum elongation: a tilt of the quasi-diagonal of R_{AB} , indicative of a wider spectral width of spectrometer A relative to spectrometer B. (E) Matched wavelengths: the R_{AB} quasi-diagonal coincides with the matrix diagonal, indicative of matched spectrometers. The yellow dotted line indicates the matrix diagonal itself in C-E.

The quasi-diagonal widths of R_{AA} and R_{BB} are indicative of the spectral resolutions of spectrometer A and spectrometer B, respectively [52] . Once one spectrometer has optimal spectral resolution (narrowest autocorrelation quasi-diagonal width at all wavelengths), the other can be aligned primarily by changing the axial translation of the focusing lens as well as the horizontal tilt and axial translation of the line scan camera (Figure 40A) until the autocorrelation quasi-diagonal widths are identical (Figure 40B). Note that the intensities can also be maximized for all pixels by changing the vertical translation and vertical tilt of the camera. Pixel correspondence between the two spectrometers requires that the column and row maxima occur along the diagonal in R_{AB} (Figure 40E). The horizontal tilt and lateral translation of the focusing lens along with the horizontal tilt and lateral translation of the line scan camera are used to match the center wavelengths of each pixel.

We adjusted the system until R_{AB} was nearly diagonal, and the quasi-diagonal widths of R_{AA} and R_{BB} were nearly identical (Figure 41A-B). Our real time alignment of spectrometers A and B yielded a root mean squared sampling deviation of 0.04 pixels (Figure 41B), which is 0.001% of the spectral range. In a parallel set of experiments, we deliberately mismatched spectrometers, leading to a root mean squared sampling deviation of 0.4 pixels (Figure 41E), to compare excess noise suppression against matched spectrometers.

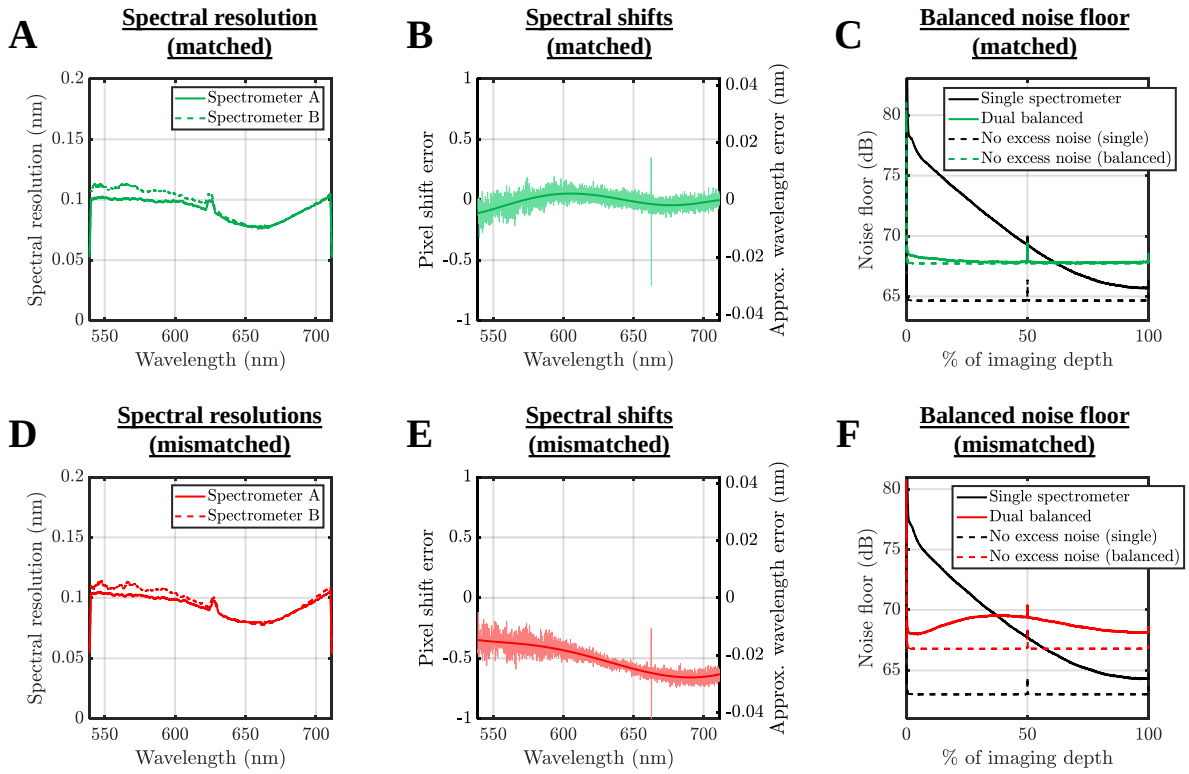

Figure 41. Matched alignment (A-C) improves balancing compared to mismatched alignment (D-F), if balancing is performed by scaled subtraction without interpolation. (A,D) The spectral resolution for both spectrometers, derived from autocorrelation matrix quasi-diagonal widths as previously described [52], for matched (A) and mismatched (D) alignment. Raw data are smoothed with a 100-pixel sliding window. (B,E) Pixel shift errors, derived from R_{AB} as previously described [52], for matched (B) and mismatched (E) alignment with shaded regions denoting raw data, and a 6th order polynomial shown in solid color. (C) With balanced detection and matched alignment, the noise floor approaches the no excess noise limit (dotted green line). (F) On the other hand, with balanced detection and mismatched alignment, the noise floor does not approach the no excess noise limit (dotted red line). This demonstrates that a mismatch of less than half a pixel can greatly degrade excess noise suppression.

We next chose the H matrix for balancing. As described in Section 6.2.1, H is the product of a scaling matrix, S, and an interpolation matrix, I_{AB}. We considered three *ad hoc* interpolation methods: no interpolation, nearest neighbor interpolation, and interpolation based on DFT upsampling in Section 6.4.6. For these three interpolation methods, the scaling matrix was taken as a diagonal matrix with $S_{ii} = R_{AB,ii} / R_{BB,ii}$ where i is the row and column index (This also happens to be the LMMSE scaling for the case of perfectly matched sampling). Finally, as a benchmark, we also tested the LMMSE estimator, which implicitly performs both scaling and interpolation. Sections 6.4.3-6.4.5 pertain to the metrics used in the evaluation of the balancing methods.

6.4.3 Evaluating noise floor and correlation matrices

A reasonable definition for the noise level is the temporal intensity or complex signal variance at each axial position (depth) over time. Yet, typically the OCT noise floor is evaluated as the offset in an averaged series of A scan intensities. If the noise in the complex A scan is circularly-symmetric Gaussian with independent and identically distributed real and imaginary parts, as is typically assumed, with mean 0 and variance σ^2 then the modulus squared (OCT intensity noise) is exponential with mean σ^2 and variance σ^4. Thus, whether the variance of the temporal intensity, variance of the complex signal, or the mean of the intensity are evaluated, the conclusions will be the same. Practically, achieving the zero-mean Gaussian complex noise requires precise mean subtraction. Therefore, we independently confirmed that the noise floor defined by the intensity mean is equivalent to the true noise floor defined by the complex variance. All variances and correlation matrices were calculated with a 512 a-line window, or "frame", for mean subtraction. Results were averaged across 64 consecutive frames.

6.4.4 Evaluating full well capacity

To estimate the excess noise of an SDOCT system, knowledge of both the detector and shot noise is needed. While detector noise can easily be measured without incident light, shot noise estimation requires knowledge of the full well capacity (FWC). We can describe the total noise variance (in units of DN^2) as

$\sigma^2[p(\lambda),\lambda] = a(\lambda) + bp(\lambda) + c(\lambda)p^2(\lambda)$ where $p(\lambda)$ is the DN level due to incident light, $a(\lambda)$ is the detector noise coefficient, b is the shot noise coefficient, and $c(\lambda)$ is the excess noise coefficient [23]. Since shot noise limited photoelectrons are a Poisson process, $b = (\frac{FWC}{2^{BD}})(\frac{2^{BD}}{FWC})^2 = (\frac{2^{BD}}{FWC})$ where BD is the bit depth of the camera (12 bits). We find b, and therefore FWC, through second-order polynomial fitting of $\sigma^2[p(\lambda),\lambda]$ using datasets with different levels of attenuation. For a group of 100 adjacent sensor pixels, we assume that b is constant while $a(\lambda)$ and $c(\lambda)$ vary. This is repeated for all sensor pixels and we average FWC across groups to yield a FWC of 12500 photoelectrons, or a b value of 2^{12} DN / 12500 photoelectrons. This b value is the conversion factor from reference DN level to shot noise variance in DN^2 (Section 6.2.3). We assumed the same b for both sensors.

6.4.5 Inverse autocorrelation matrix

The LMMSE estimator requires an inverse autocorrelation matrix, $(R_{BB})^{-1}$. As the matrix inverse is sensitive to noise, we first locally averaged the autocorrelation matrix R_{BB} using a square window whose size (in pixels) varied as $\lfloor 0.06|i-j| \rfloor$, where $\lfloor \bullet \rfloor$ denotes the floor, i is the row index, and j is the column index. This variable averaging window size ensured that the quasi-diagonal was accurately represented without blurring, while also ensuring adequate noise averaging away from the diagonal. After averaging, a pseudo-inverse with a singular value threshold of 30 (units of camera DN^2) was taken as the estimate of the inverse.

6.4.6 Balancing performance

Performing balancing as a simple scaled subtraction (Figure 41C), the experimental noise floor approached the sum of shot and detector noise (referred to as the no excess noise limit) with matched spectrometers. This limit was not achieved by a scaled subtraction with mismatched spectrometers (Figure 41F). Next, more advanced balancing approaches were compared in more detail (Figure 42 columns), ranging from

scaling with no interpolation (Figure 42 and Table 2, leftmost column) to the LMMSE estimate (Figure 42 and Table 2, rightmost column). Residual excess noise (Figure 42 top row) and excess noise suppression, or the ratio of excess noise after subtraction to excess before subtraction (Figure 42 second row), were evaluated versus depth. These comparisons revealed that the excess noise suppression for mismatched spectrometers particularly suffered at large depths, in agreement with simulations (Section 6.3). Accordingly, spectrometer matching achieved a dramatic improvement of more than tenfold in excess noise suppression at the end of the depth range when using the LMMSE estimator (Figure 42H). The spectral excess noise suppression (Figure 42 third row) showed that for mismatched spectrometers and nearest neighbor interpolation (columns 2), excess noise after balancing was worst at wavelengths where the pixel shift neared 0.5 pixels (Figure 41E). Rolloffs after balancing showed minor differences between matched and mismatched alignment for basic interpolation methods (Figure 42 last row, columns 1-2). Such differences were not evident for more advanced balancing methods (Figure 42 last row, columns 3-4).

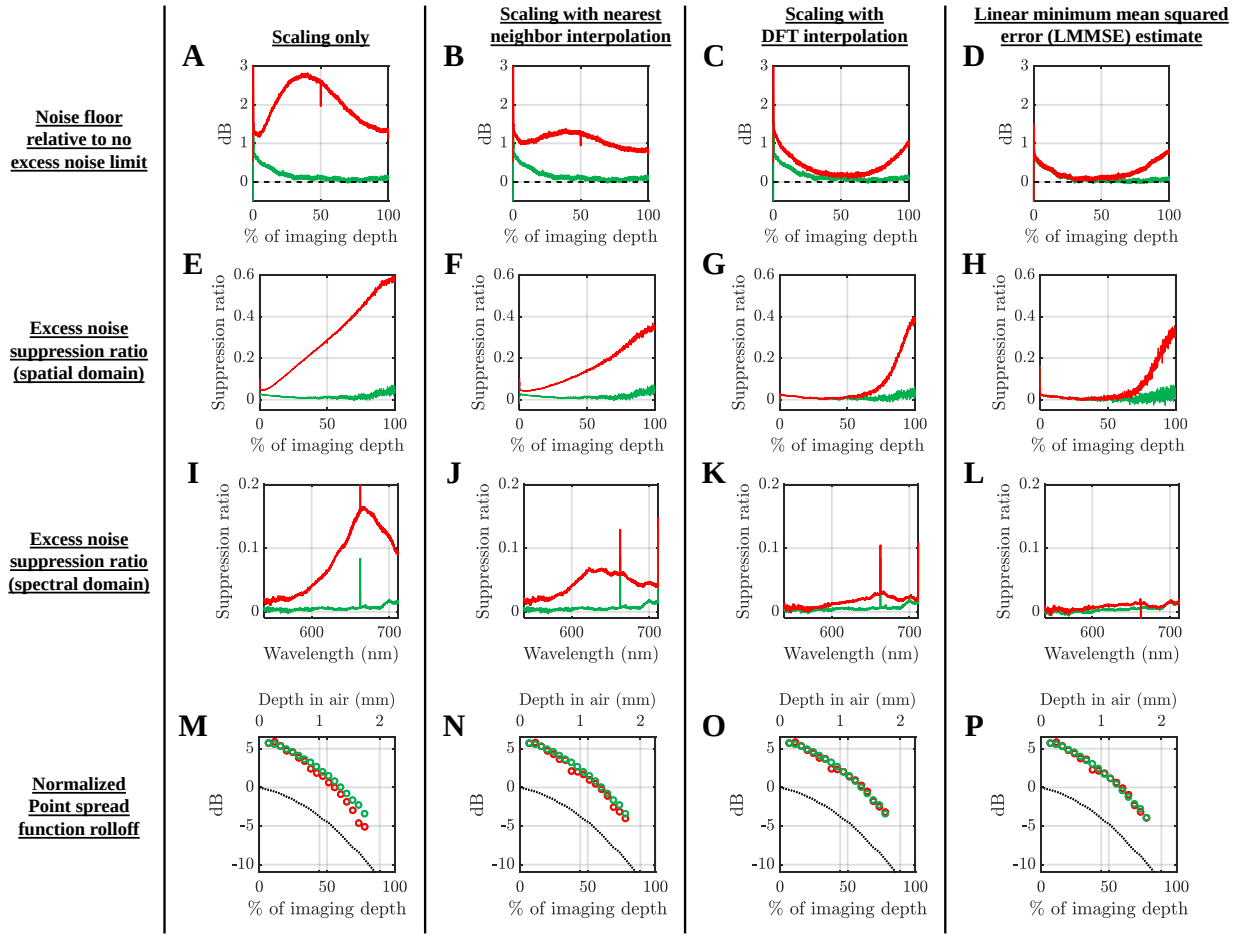

Figure 42. Comparison of different interpolation methods with respect to excess noise floor (A-D), spatial excess noise suppression (E-H), spectral excess noise suppression (I-L), and the point spread function rolloff (M-P) with matched (green) and mismatched alignment (red), as depicted in Figure 41. Dashed line in (A-D) refers to the no excess noise limit. Dotted line in (M-P) refers to the point spread function rolloff of a single spectrometer. Regardless of the balancing method, the excess noise suppression for matched alignment exceeds that for mismatched alignment, with particular improvement in the suppression ratio at larger depths (E-H). Overall excess noise suppression is shown in Table 2.

Table 2. Excess noise suppression, defined as the ratio of the excess noise corrupting the balanced signal, after subtraction, to the total excess noise corrupting the two spectrometer signals, before subtraction.

Interpolation Method	Scaling only	Scaling with nearest neighbor interpolation	Scaling with DFT interpolation	LMMSE Estimate
Mismatched	-9.6 dB	-12.9 dB	-16.8 dB	-19.8 dB
Matched	-21.2 dB	-21.2 dB	-21.4 dB	-22.6 dB

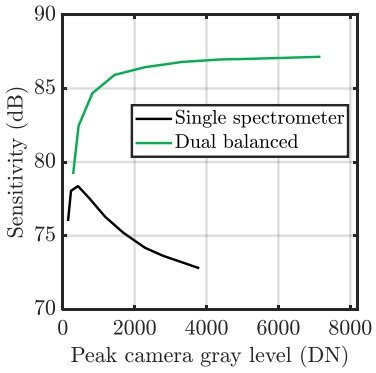

Figure 43. Sensitivity versus reference power at a depth of 100 µm in air for both the single spectrometer and proactively matched, balanced spectrometers. The single spectrometer has an optimal reference gray level (peak across spectrum shown) that maximizes sensitivity, by balancing heterodyne gain against excess noise (black). By comparison, the balanced sensitivity increases monotonically with gray level (peak of sum of two spectrometer gray levels shown), reaching a plateau, indicating negligible excess noise (green). Measurements were performed with 125 µW incident power and 60 dB attenuation, at a 70 kHz a-line rate. Note that if the noise floor is determined at shallower depths, sensitivity improvements will be greater, while if the noise floor is determined at greater depths, sensitivity improvements will be lower. A computationally-simple scaled subtraction with no interpolation was employed for balancing.

In the best configuration, with matched spectrometer alignment and the LMMSE estimator (Figure 42 last column), we obtained an overall excess noise suppression (total excess noise across all pixels remaining after subtraction divided by the total excess noise across all pixels prior to subtraction) of -22.6 dB (Table 2). With matched spectrometers and the LMMSE estimate, shot noise accounted for approximately 89% of the overall noise after balancing, while camera noise accounted for 8% of the overall noise after balancing, and excess noise contributed just 3% of the overall noise after balancing. The excess noise suppression was found to worsen with depth (Figure 42H), as predicted by simulations (Section 6.3). For matched spectrometers, the best sensitivity improvement at any depth relative to a single spectrometer, accounting for the ~6 dB signal gain, was approximately 28.5 dB; however, such a dramatic improvement was only observed at a relative depth of 0.1% of the total depth range. The sensitivity at 100 µm depth, 4.4% of the total depth range, showed a more modest improvement of 14.3 dB (Figure 43), with matched spectrometers and scaled subtraction (no interpolation).

6.5. Results

6.5.1 *In vivo* mouse retinal imaging

We tested the performance of shot noise limited visible light OCT by imaging the retina of a 19.5 month old male mouse (C57BL/6J, The Jackson Laboratory). All animal procedures and protocols were approved by the Institutional Animal Care and Use Committee at the University of California, Davis. Near-infrared OCT cannot clearly visualize the RPE in this highly pigmented strain [126]. Visible light OCT imaging was performed using a power of 125 μW on the cornea and a 70 kHz a-line rate. This represents just 6% of the incident photons per a-line acquired by our previous mouse retinal imaging system, which had an incident power and a-line rate of 300 μW and 10 kHz [32], respectively. Eight repeated volumetric datasets with 512 a-lines and 64 b-scans (frames) per volume were taken with an acquisition time of 3.7 seconds. We scanned a region of 1.44 mm along the fast axis and 120 micrometers along the slow axis on the retina. Spatially-dependent dispersion compensation was employed in the reconstruction, as previously described in Chapter 3 [32], and applied to the balanced signal [32]. Images were motion corrected and intensity-averaged to reduce speckle, as well as other noise sources.

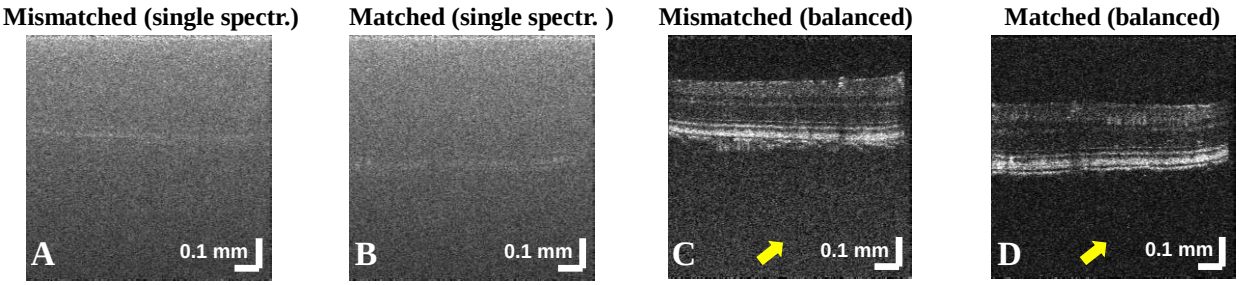

Figure 44. The signal from the mouse retina is overwhelmed by the excess noise in an image from a single unbalanced spectrometer (A-B). Yet the retina is clearly revealed by balancing (C-D). Matched spectrometers (B) further reduce the noise floor compared to mismatched spectrometers (A), as shown by the yellow arrows. A simple scaling was employed with no interpolation was employed for balancing. The difference in noise floors observed in A-B is consistent with that observed in Figure 41 and the first column of Figure 42.

Firstly, in individual frames from a single spectrometer without balancing (Figure 44A-B), very few details were observed, except for the retinal pigment epithelium (RPE). Balancing revealed the major retinal layers,

even at an a-line rate of 70 kHz with a noisy supercontinuum source. While the retrospectively-calibrated, mismatched spectrometers showed an increase in the noise floor at larger depths (Figure 44C), proactive matching of the spectrometers resulted in a more uniform and lower noise floor (Figure 44D). These results are fully consistent with the excess noise floors shown in Figure 41 and the first column of Figure 42.

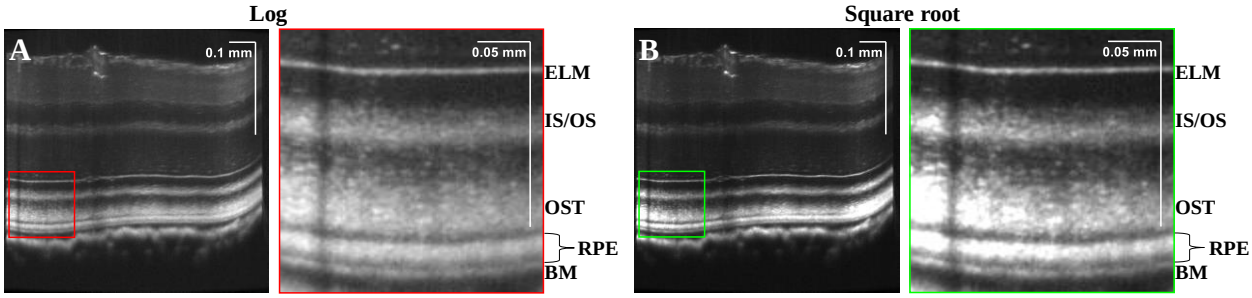

Figure 45. Average of 8 repeated volumes (64 frames per volume) after motion correction, depicts detail in the outer retina, including the separation between the retinal pigment epithelium (RPE) and photoreceptor outer segment tips (OST) and the separation between the RPE and Bruch's membrane (BM). This enables clear visualization of both the inner and outer aspect of the RPE in a highly pigmented mouse strain, which was not achieved in previous studies. ELM: external limiting membrane, IS/OS: photoreceptor inner segment/outer segment junction.

We next motion-corrected frames from the entire data set with 8 repeated volumes. Intensity-averaged images showed clear outer retinal bands. Notably both the inner and outer edges of the retinal pigment epithelium (RPE) band were well-visualized, even in the aged mouse (Figure 45).

6.6. Conclusions

It is well-known that matching of power or intensity is essential to achieve effective balancing and excess noise cancellation [112, 116]. This work highlights the importance of spectral matching (i.e. matching of wavelength sampling and resolution) in balanced SDOCT. Building on the realization that excess noise provides a useful tool for spectrometer calibration [52, 115] and characterization [52], we propose a proactive approach to achieve effective spectral matching. We show that while a retrospective calibration [52] of mismatched spectrometers can improve balancing, achieving the shot noise limit across the entire depth range requires proactive spectrometer matching at the sub-pixel level. In contrast to previous work

[115] that was restricted to assessing correlation between corresponding spectrometer pixels (i.e. the diagonal of the cross-correlation matrix), the present work employs the entire cross-correlation matrix to assess sub-pixel shifts. The present work also recognizes the importance of matching spectral resolutions, determined here from the respective autocorrelation matrices. Our proactive approach for matching two spectrometers while monitoring excess noise correlations achieves a precision of just 0.001% of the overall spectral range, better than standard manufacturing tolerances. Our matching approach may eventually help improve other applications of optical spectroscopy, including Raman, absorption, and fluorescence, where high precision will aid reproducible measurements of narrow spectral features.

This work also provides a detailed formulation of balancing as two constituent linear operations (matrix multiplications): interpolation and scaling. Our formalism succinctly described different balancing methods and provided a connection between spectrometer alignment, the optimal balancing approach, and noise suppression performance. Regardless of alignment we found that the degree of excess noise cancellation improved with more advanced digital cancellation schemes, culminating with the highest overall excess noise suppression of the LMMSE estimator. This is reasonable as the LMMSE estimate accounts for all pairwise noise correlations between pixels in deriving the optimal estimate. If proactive pixel matching is not possible or practical, the LMMSE estimator was shown to be the best balancing strategy for overall excess noise suppression.

Proactive matching achieved overall excess noise suppression of >20 dB (>100x) in magnitude. With proactive matching, even without any pixel interpolation (i.e. a pure scaled subtraction), it was possible to nearly achieve the performance of the LMMSE estimate. This makes sense, since the optimal interpolation matrix approaches the identity matrix as matching improves, meaning that interpolation is less critical for performance. A scaled subtraction requires P multiplies and P additions, where P is the number of pixels. This is much less computationally intensive than the Fast Fourier Transform, which requires $P/2\log_2 P$ multiplies and $P\log_2 P$ additions. Therefore, with proactive matching, effective excess noise cancellation can be achieved with minimal additional computational time compared to normal OCT

reconstruction. By comparison, retrospective matching approached 20 dB excess noise suppression, and only with a computationally complex balancing procedure.

Experimentally, for every single balancing and interpolation scheme, proactive spectrometer matching improved performance. In fact, all four balancing methods we investigated for matched spectrometers outperformed the highest-performing LMMSE estimate for mismatched spectrometers. While lower levels of excess noise suppression were tolerable in this study, the excess noise suppression value sets a hard upper limit on the overall sensitivity improvement of the balanced spectrometer. We project that proactive matching will be especially important for OCT systems with high noise sources or rapid imaging speeds, as such systems require a high degree of excess noise suppression to reach the shot noise limit. Our proactive matching approach can also be used with linear-in-k spectrometers [127] to remove the need for resampling.

High excess noise suppression enabled by precise balancing could enable visible light OCT in a new regime with higher speeds, lower repetition rates, and lower incident powers. To assess this potential, Table 3 summarizes the performance of exemplary visible light OCT systems in the literature with respect to the approximate spectral energy density per a-line, related to brightness of speckles, and the pulses per a-line, related to reduction of supercontinuum excess noise through averaging. Table 3 reveals that our study performs visible light OCT retinal imaging with the smallest number of pulses and the lowest spectral energy density per a-line compared to previous work.

Table 3. Performance of exemplary retinal visible light OCT systems in the literature. Key parameters are spectral density and number of pulses per a-line.

Authors	Harper et al. [128, 129]	Rubinoff et al. [130, 131]	Pi et al. [24, 25]	Ju et al. [28]	This work
Subject	Mouse	Mouse	Rat	Mouse	Mouse
Imaging speed	25 kHz	25 kHz	50 kHz	40 kHz	70 kHz
Power	900 μW	1200 μW	800 μW	110 μW	125 μW

Spectral density/a-line	240 $\frac{pJ}{nm}$	480 $\frac{pJ}{nm}$	180 $\frac{pJ}{nm}$	92 $\frac{pJ}{nm}$	12 $\frac{pJ}{nm}$
Repetition rate	78 MHz	>78 MHz	>78 MHz	30 MHz	30 MHz
Pulses/a-line	3120	3120	1560	750	429

The results of this study may also improve access to visible light OCT by reducing cost. This study reported an 87 dB sensitivity at a 70 kHz a-line rate and 125 μW incident power. Previously, without balancing, comparable performance required 1.25 times the incident power, and a more expensive low noise source with 5.2 times the repetition rate [23]. The 30 MHz source used in this study has a retail price ($25k) of less than half that of more standard, low noise supercontinuum sources ($65k). Yet performance approaching the shot noise limit was achieved with balancing, which only requires the addition of a frame grabber and camera ($10k). Thus, a net cost reduction of $30k, equal to almost half the initial light source cost, was achieved in this study.

Another challenge in visible light OCT is the retinal changes induced by visible light exposure. Light levels are typically set well below levels that cause permanent retinal changes, as dictated by the ANSI standards [132]. However, the high bleaching levels of visible light OCT induce water movements, cell swelling [133], scattering changes [133], as well as potentially, melanosome movement [134]. Given all of these confounds, we conclude that visible light OCT images should be collected with as little visible light exposure to the retina as possible. We found that the combination of the rapid imaging speed and relatively low power of 125 microwatts enabled us to align the mouse eye and acquire images quickly, minimizing (but certainly not eliminating) the potential for light induced physiological changes. Interestingly, with this rapid alignment, we found that the clarity of the RPE was improved in the aged, 19.5 month old mice, even relative to images we had acquired previously in mice that were a few months old [52]. The improved clarity enabled us to estimate RPE thickness, taken as the distance from the inner RPE band to the inner BM band. The RPE thickness in the C57BL/6J mouse was estimated as 6.6 ± 0.9 micrometers, which is significantly thinner than the human RPE [135].

In summary, in this work, we show that excess noise cancellation in balanced SDOCT cannot be achieved without spectral matching. With our method of matching spectrometers, overall excess noise suppression of more than two orders of magnitude was achievable with a simple scaled subtraction. Ultimately, to enable noisy supercontinuum

sources to achieve the SDOCT performance of SLD sources, we require excess noise suppression on the order of 30 dB. In this study, while pixel matching yielded the best experimental results, some residual excess noise remained. We found that an excess noise suppression magnitude of 27.2 dB (4.6 dB better than the best result in Table 2 for 4096 pixels) was achievable by utilizing only the first 2048 shorter wavelength pixels of the matched sensors. The reason for worse excess noise suppression at long wavelengths remains unclear, as the residual pixel and spectral resolution mismatch were not higher at longer wavelengths. In the future, contributions of the interferometric term to excess noise, digitization effects, and non-stationarity should be investigated as factors that may alter excess noise suppression.

Chapter 7: Discussion and conclusion

7.1. Future directions

7.1.1 Higher axial resolution for visible light OCT

Currently, the full spectral bandwidth of the dual balanced visible light OCT system, previously reported, is 345 nm if all 8192 pixels in the camera are used. However, the current best achievable axial resolution is only 1.2 micron in air since the spectrum does not utilize the full spectrometer bandwidth. We hypothesize that the spectrum is narrowed by the fiber coupler, fibers, diffraction efficiency of grating, and quantum efficiency of the sensor. A fully free-space system can eliminate any attenuation from the fiber couplers and fibers. As seen throughout this work, new retinal bands were discovered with finer axial resolution. We hope that visible light OCT can help discover new information regarding these bands. The first step is to validate the new bands against gold standard techniques. The sections below describe preliminary results towards these validations.

7.1.2 Retinal band validation with electron microscopy

The data in this section were acquired by me, with lots of help from Paul Fitzgerald and Brad Shibata. My colleague, Pooja Chauhan, has continued the project and has done all of the processing and figures, with input from myself and Dr. Srinivasan.

We plan to investigate the origins of the various bands that we discovered in this thesis by comparing visible light OCT images with electron microscopy (EM). In these studies, we imaged both eyes of four mice which were aged 2.5 months, 4.5 months, 13 months, and 19 months. Within a week of visible light OCT imaging, we euthanized the animals by carbon dioxide inhalation. Similar to the study of Meleppat et al. [136], the eyes were enucleated and postfixed in 2% glutaraldehyde in 0.1 M sodium phosphate buffer, pH 7.4 [137]. The lens was removed and the retina was separated. A 1 mm by 1 mm square, centered on the optic disc, was cut for *ex vivo* imaging. The tissue was blocked, rinsed in 0.1 M sodium phosphate buffer, stained with 1% osmium tetroxide, rinsed in distilled H_20, and dehydrated with an increasing series of ethanol. Next, the tissue was placed in a pre-inflitrate of 50% propylene oxide and 50% PolyBed resin overnight, then infiltrated with 100% PolyBed resin and polymerized in fresh resin. Thin sections (80-90 nm) were cut on an ultramicrotome, collected on copper slot grids, and stained with 4% uranyl acetate and 0.3% lead citrate in 0.1 N sodium hydroxide and examined with transmission electron microscope (Talos L120C TEM) [136]. For each eye, many EM images at 1250x or 1650x magnification were taken of the sample over an approximately 1 mm strip. EM and visible light OCT images were co-registered within ±0.5 mm.

7.1.2.1 Validation of outer nuclear layer dark band based on cell nuclei with electron microscopy

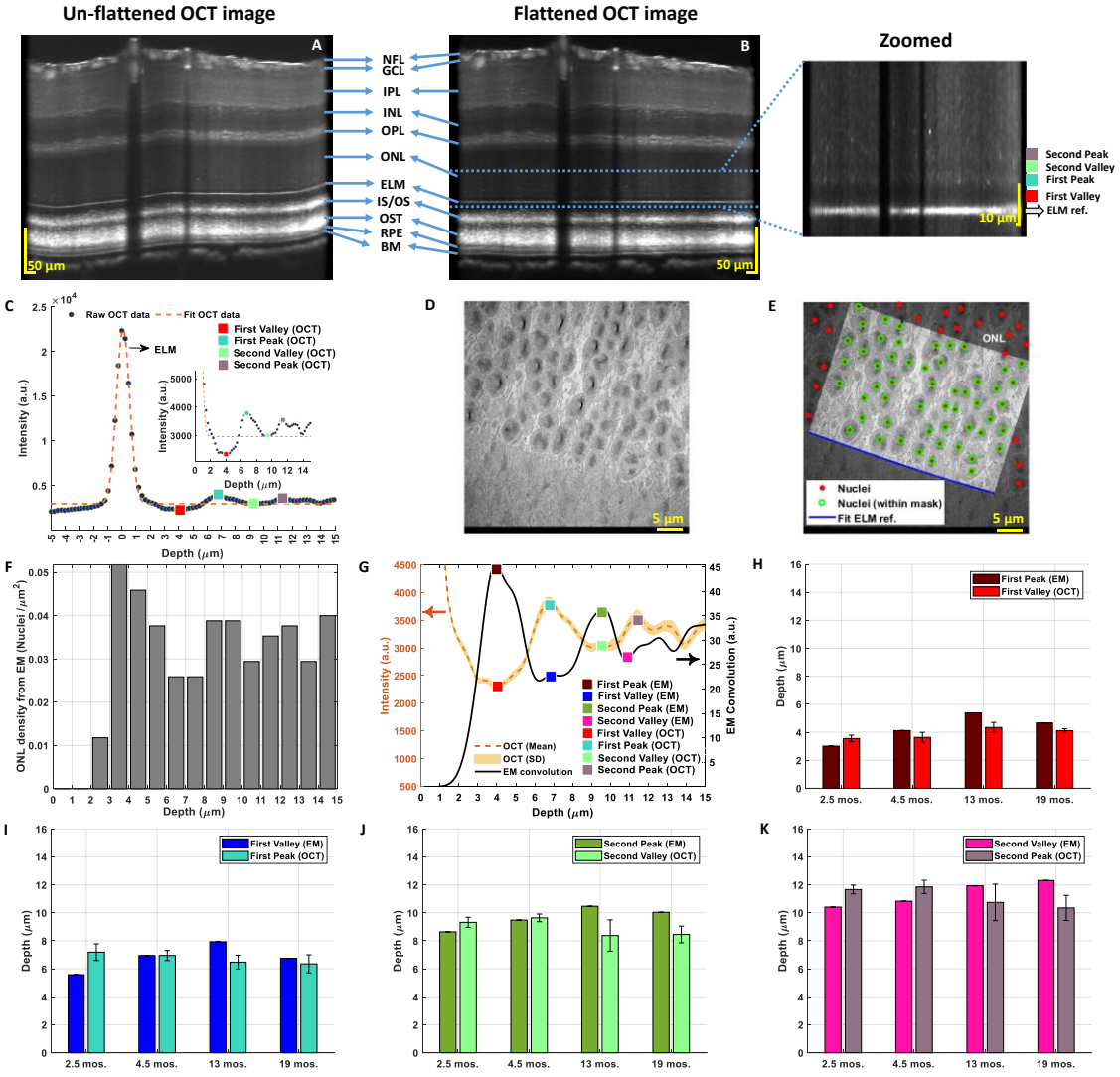

Figure 46. Visible light OCT linear-scaled scan of a 4.5 mos. mouse retina A) unflattened, B) flattened with corresponding zoomed view of outer ONL and ELM cell layers to visualize the dark band. C) Gaussian fitting of the raw OCT reflectivity profile. Cross-sectional view of EM images showing D) nuclei in the ONL cell layer, E) masking of nuclei by referencing the ELM cell layer. F) Histogram obtained for ONL density from the masking of nuclei in the EM image. G) Comparison plot of OCT reflectivity and convolved EM profiles. Comparison of H) EM first peak and OCT first valley, I) EM first valley and OCT first peak, J) EM second peak and OCT second valley, K) EM second valley and OCT second peak with depth in 2.5 mos., 4.5 mos., 13 mos., and 19 mos. mice (in terms of mean and standard deviation).

Following up on the discovery mentioned in section 4.6.6, we plan to investigate the band inner to the ELM by comparing the visible light OCT images to electron microscopy (EM) images. As a preliminary demonstration, 1250x EM images were taken of the ONL with the ELM in view. For each EM image, the ONL nuclei were masked (Figure 46E) to prevent biasing the ONL cell density. The shortest possible distance from the ONL nuclei and the ELM were recorded for all ONL nuclei and the ONL density was plotted as a function of depth (Figure 46F). The visible light OCT image (Figure 46A) was flattened (Figure 46B) and intensity profiles of the ONL were taken within 20 μm of the ELM (Figure 46C). We directly compared the ONL density from the EM images, convolved with the incoherent point spread function, to the intensities measured from the visible OCT data (Figure 46G). Surprisingly, we found that the peaks in the OCT data corresponded with the valleys of the ONL densities from the EM data (Figure 46G). This correspondence was consistent for all of the data from the four mice (Figure 46H-K and Figure 47).

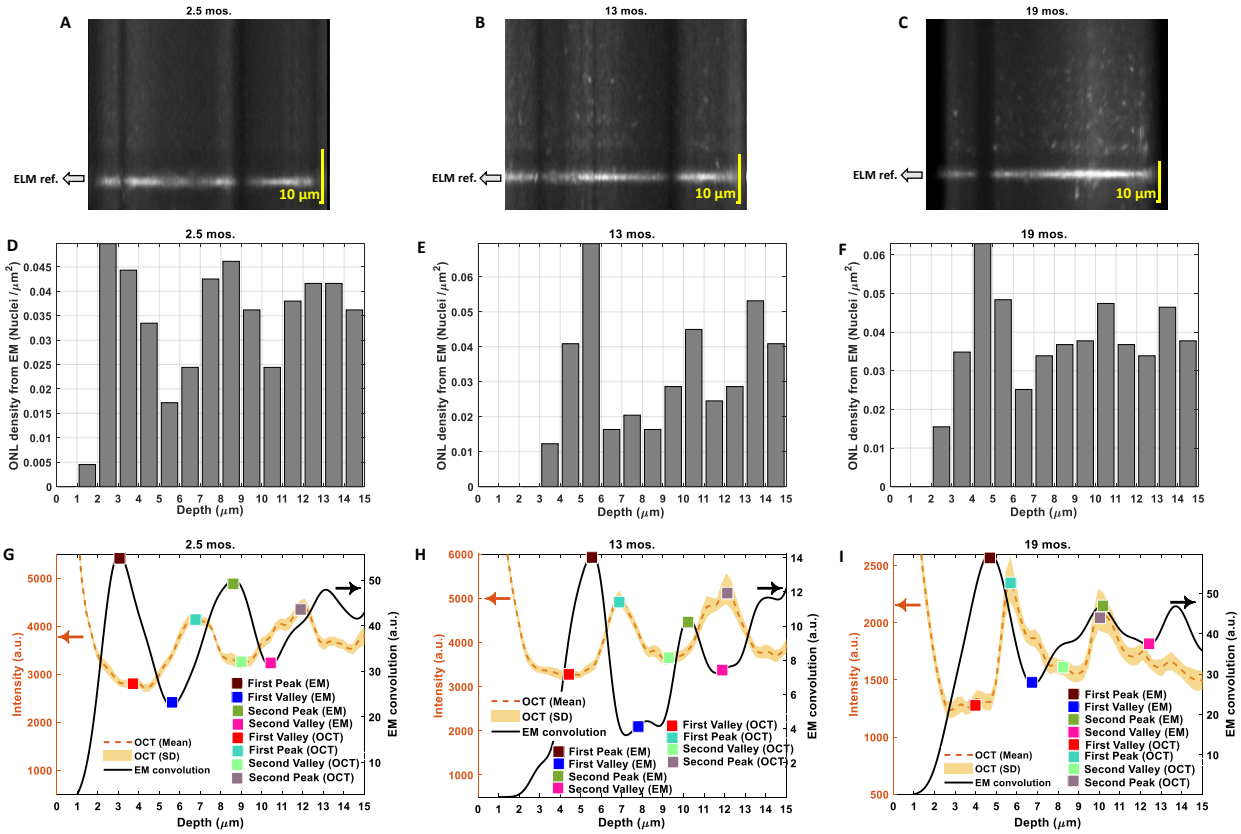

Figure 47. Zoomed linear-scaled view of outer ONL and ELM cell layers to visualize the dark band acquired from A) 2.5 mos., B) 13 mos., C) 19 mos. mice. Histogram plots corresponding to D) 2.5 mos., E) 13 mos., F) 19 mos. mice for ONL density from the masking of nuclei in the EM images. Comparison plots of OCT reflectivity and convolved EM profiles in G) 2.5 mos., H) 13 mos., I) 19 mos. mice.

7.1.2.2 Estimation of RPE width in visible light OCT

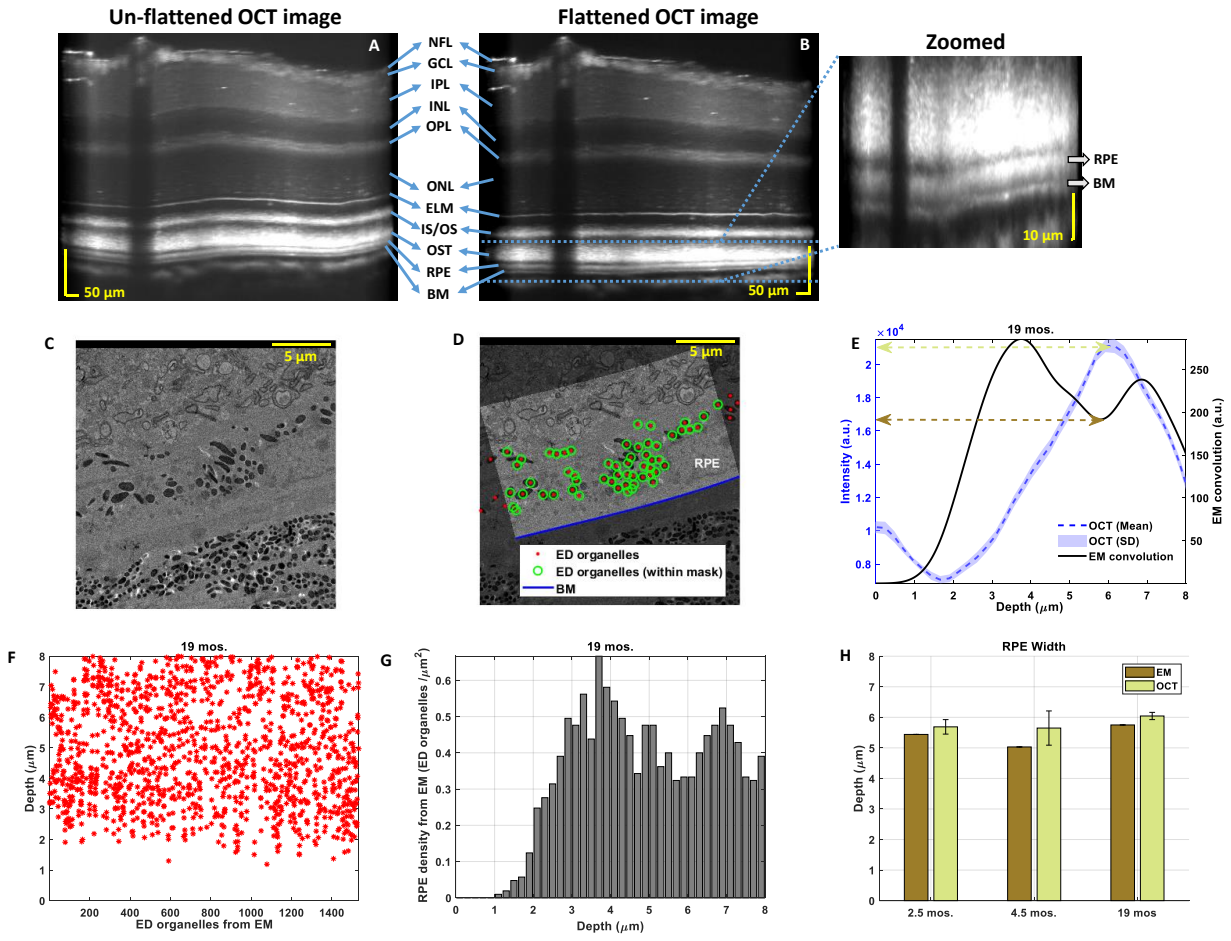

Figure 48. Visible light OCT linear-scaled scan of a 19 mos. mouse retina A) unflattened, B) flattened with corresponding zoomed view of outer RPE and BM cell layers. Cross-sectional view of EM images showing C) ED organelles in the RPE cell layer, D) masking of ED organelles by referencing the BM cell layer. E) Comparison plot of OCT reflectivity and convolved EM profiles. F) Density plot of ED organelles from EM. G) Histogram obtained for RPE density from the masking of ED organelles in the EM image. H) Correlation of RPE width by EM and OCT with depth in 2.5 mos., 4.5 mos., and 19 mos. mice (in terms of mean and standard deviation).

We also aim to validate the RPE width measured from visible light OCT with EM. As a preliminary demonstration, the visible light OCT images (Figure 48A) were flattened (Figure 48B) and the intensity was taken along the axial direction of the RPE. We apply a similar mask mentioned in Section 7.1.2.1 and apply it to the RPE organelles. Within the mask, we recorded the shortest distance between the electron dense (ED) RPE organelles and the BM (Figure 48F). We convolved the ED organelle density relative to

BM with the incoherent point spread function from the visible light OCT system. Assuming that the OCT intensity from the RPE band is correlated with RPE ED organelle density, we compared the RPE band intensity from the OCT data with the convolved RPE ED organelle density (Figure 48E). We saw good agreement between the RPE widths from OCT and EM data (Figure 48H).

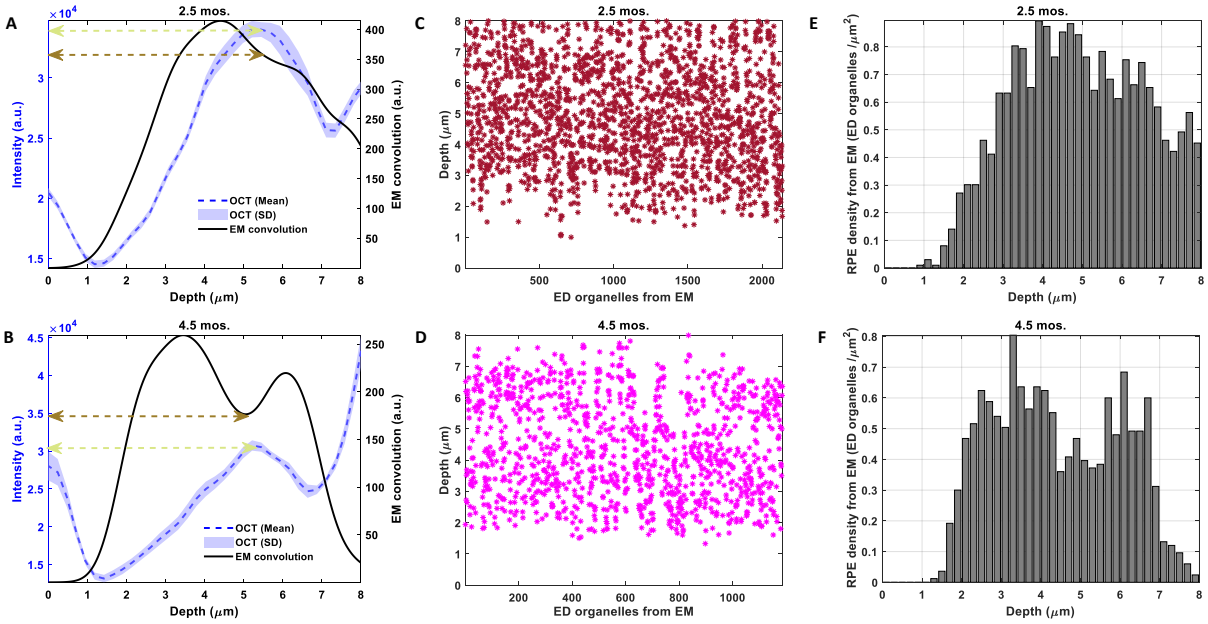

Figure 49. Comparison plots of OCT reflectivity and convolved EM profiles in A) 2.5 mos., and B) 4.5 mos., mice. Density plots of ED organelles from EM in C) 2.5 mos., and D) 4.5 mos., mice. Histogram plots corresponding to E) 2.5 mos., and F) 4.5 mos. for RPE density from the masking of ED organelles in the EM images.

7.1.2.3 Validation of outer retinal band 2 origin (IS ellipsoid or IS/OS junction) with electron microscopy

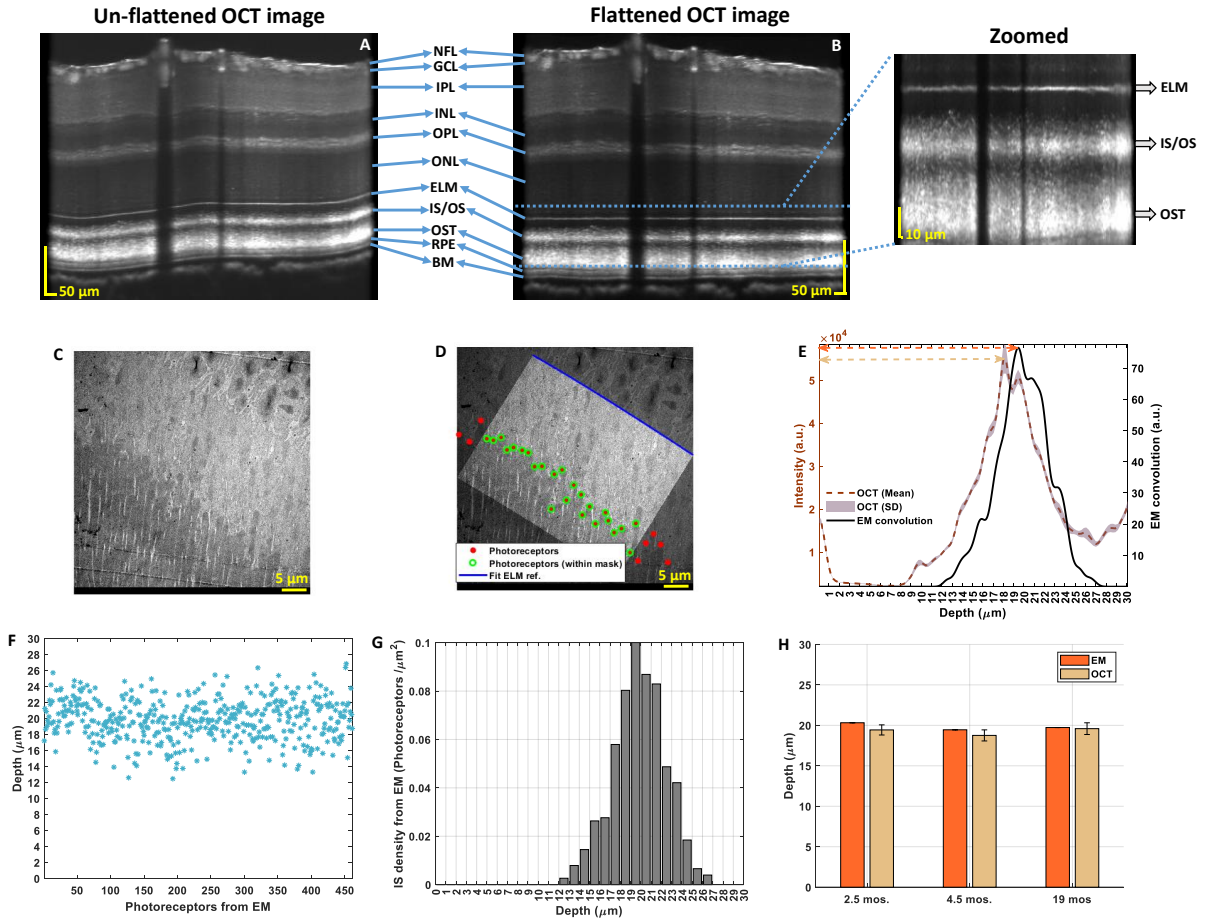

Figure 50. Visible light OCT linear-scaled scan of a 4.5 mos. mouse retina A) unflattened, B) flattened with corresponding zoomed view of outer ELM, IS/OS and OST cell layers. Cross-sectional view of EM images showing C) Photoreceptors in the IS cell layer, D) masking of photoreceptors by referencing the ELM cell layer. E) Comparison plot of OCT reflectivity and convolved EM profiles. F) Density plot of photoreceptors from EM. G) Histogram obtained for IS density from the masking of photoreceptors in the EM image. H) Correlation of width by EM and OCT with depth in 2.5 mos., 4.5 mos., and 19 mos. mice (in terms of mean and standard deviation).

There has been controversy about whether outer retinal band 2 arises from the inner segment ellipsoid or the IS/OS junction. Here, we aim to add to this discussion by comparing ultrahigh resolution visible light OCT images and EM images. As a preliminary demonstration, a similar mask to those described in Section 7.1.2.1-7.1.2.2 was applied to the IS/OS junctions and their distances were measured relative to the ELM (Figure 50D,F). Similarly, the axial profile of outer retinal band 2 in the visible light OCT was plotted as a

function of distance from the ELM band. This profile was convolved with the visible light OCT incoherent point spread function, similar to Section 7.1.2.2. Both the OCT axial profiles and the convolved EM data were compared (Figure 50E). We see that OCT band 2 and the IS/OS convolved distribution from EM both exhibit similar distances from the ELM and also similar shapes. This strengthens the argument that so-called outer retinal band 2 is the IS/OS junction.

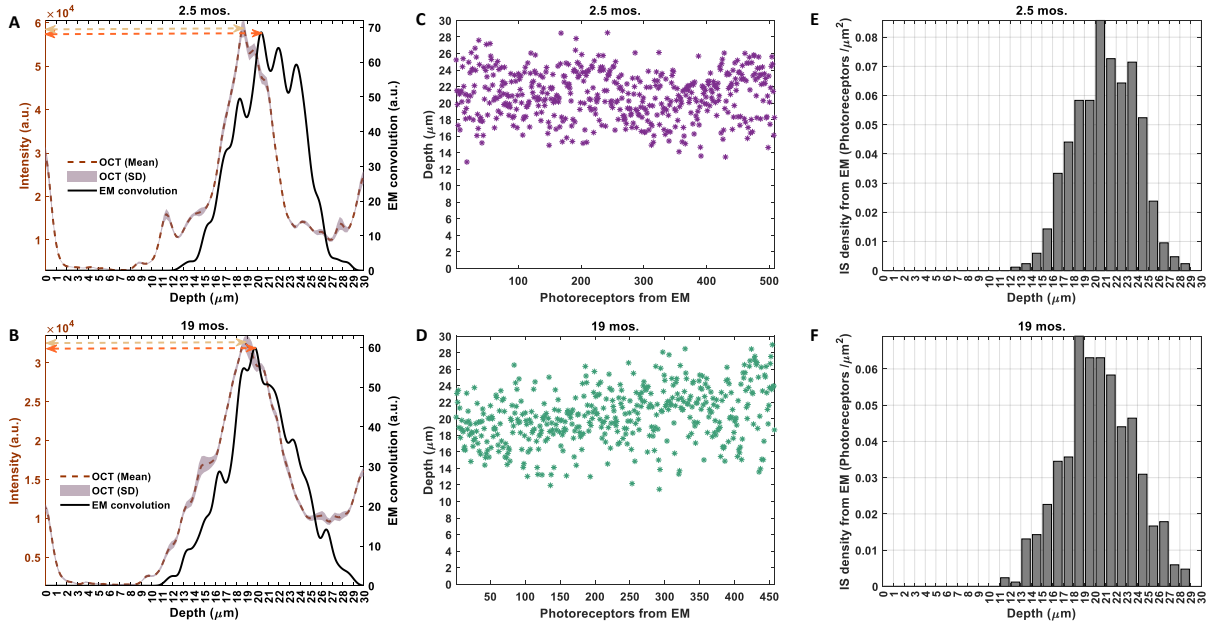

Figure 51. Comparison plots of OCT reflectivity and convolved EM profiles in A) 2.5 mos. and B) 19 mos. mice. Density plots of photoreceptors from EM in C) 2.5 mos., and D) 19 mos., mice. Histogram plots corresponding to E) 2.5 mos., and F) 19 mos. for IS density from the masking of photoreceptors in the EM images.

7.1.3 Higher speeds for visible light OCT

Previously, higher excess noise at faster speeds was limiting visible light OCT to mostly lower line rates [24, 26, 130]. Now that we have a method to suppress excess noise, we aim to push the speed of visible light OCT to those achievable with near infrared OCT. Our next step is to study photopigment bleaching changes with visible light OCT with imaging at speeds around 100-150 kHz and with 100 μW power.

7.1.3.4 Spectroscopic visible light OCT for rhodopsin quantification

Photoreceptor loss secondary to the RPE/BM changes directly impairs visual function. Visual acuity and color vision require the health of the cone photoreceptors. Low light sensitivity and full dark adaptation require the health of the rod photoreceptors. Multiple lines of evidence suggest that rods are affected more than cones in aging and AMD. First, rods are preferentially lost over cones in aging [138] and AMD [139]. Rod-mediated scotopic light sensitivity is lost in aging [140], more so than photopic sensitivity, and in AMD [141], with the AMD-related loss being most severe in the parafovea. Additionally, rod-mediated dark adaptation is prolonged in aging [142] and in AMD [143], probably related to impaired transport across a hydrophobic Bruch's membrane. Photopigment density may be a practical method to study photoreceptors without the need to count them.

Retinal densitometry aims to objectively quantify the concentration or density of photopigment in the retina, based on fundus measurements that have limited or no depth resolution. Photopigment densitometry [144] measures and compares the amount of light reflected before and after a bleaching stimulus, assuming that the reflections arise solely from posterior retinal layers, and changes are only due to photopigment bleaching [145-147]. These assumptions are invalidated by stray light, anterior retinal reflections, and importantly, fluctuations in photoreceptor reflectance that are not directly related to photopigment absorbance [148, 149].

This proposal leverages the recent improvements in resolution, sensitivity, and speed from the thesis of balanced detection visible light OCT to obviate these assumptions. Using the visible OCT beam as a bleaching stimulus, and leveraging the depth resolution of OCT, we can now assess reflections immediately anterior and posterior to the outer segments, eliminating the confounds of fundus reflectometry.

7.1.4 Mouse model imaging with visible light OCT

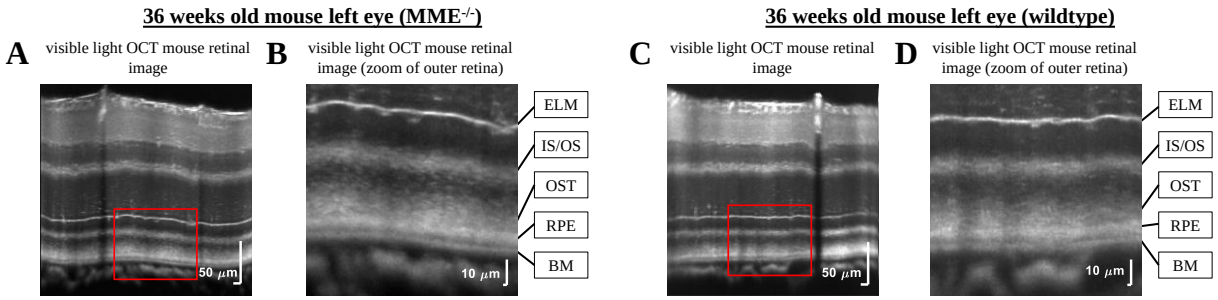

Figure 52. (A) Visible light OCT averaged b-scan image of a 36 weeks old MME$^{-/-}$ mouse model retina with a zoom (B) of the outer retina. (C) Visible light OCT averaged b-scan image of a 36 weeks old wildtype mouse retina with a zoom (D) of the outer retina.

In collaboration with Glenn Yiu's group from the department of Ophthalmology and Vision Science at University of California, Davis, we aim to investigate outer retinal changes, specifically Bruch's membrane changes, in a strain of neprilysin$^{-/-}$, or membrane metallo-endopeptidase (MME) $^{-/-}$, mutant mouse model. Although this model is typically used for Alzheimer's disease, these mice may develop retinal lesions with many features that emulate dry AMD including Bruch's membrane thickening [150-152]. Now that visible light OCT can visualize the Bruch's membrane band in MME$^{-/-}$ mutant strains (Figure 52) and wild type mouse retinas [32], we hope to show that Bruch's membrane thickness can be an AMD biomarker by demonstrating Bruch's membrane thickness differences between wildtype and MME$^{-/-}$ strain retinas.

7.2. Conclusion

In this thesis work, we improved visible light OCT in a variety of ways. We improved experimental axial resolution by implementing spatially dependent dispersion compensation and improving spectrometer alignment. We improved the sensitivity by improving spectrometer alignment and properly implementing dual balanced detection. As a result of eliminating excess noise and improving SNR, we were able to also increase the imaging speeds and utilize cheaper and smaller light sources that have similar, if not better, imaging quality. While this thesis focused on the mouse retina, the advances presented here also aided the first quantitative morphometric visible light OCT studies in humans [135, 153].

Although the emphasis of this work is to better understand retinal morphology, we hope these improvements aid in the dissemination and eventual commercialization of visible light OCT. Hopefully, the cost reduction and image quality improvement provided by this work brings visible light OCT closer to commercialization so the additional functionalities can benefit the public.

Chapter 8: References

1. Z. A. Auzzir, R. P. Haigh, and D. Amaratunga, "Public-private partnerships (PPP) in disaster management in developing countries: a conceptual framework," Procedia economics and finance **18**, 807-814 (2014).
2. J. C. Booij, D. C. Baas, J. Beisekeeva, T. G. Gorgels, and A. A. Bergen, "The dynamic nature of Bruch's membrane," Progress in retinal and eye research **29**, 1-18 (2010).
3. R. S. Ramrattan, T. L. van der Schaft, C. M. Mooy, W. De Bruijn, P. Mulder, and P. De Jong, "Morphometric analysis of Bruch's membrane, the choriocapillaris, and the choroid in aging," Investigative ophthalmology & visual science **35**, 2857-2864 (1994).
4. A. Okubo, R. Rosa, C. V. Bunce, R. A. Alexander, J. T. Fan, A. C. Bird, and P. J. Luthert, "The relationships of age changes in retinal pigment epithelium and Bruch's membrane," Investigative ophthalmology & visual science **40**, 443-449 (1999).
5. W. R. Green, "Histopathology of age-related macular degeneration," Mol Vis **5**, 1-10 (1999).
6. A.-R. E. D. S. R. Group, "The Age-Related Eye Disease Study severity scale for age-related macular degeneration: AREDS report no. 17," Archives of Ophthalmology **123**, 1484-1498 (2005).
7. R. P. Finger, Z. Wu, C. D. Luu, F. Kearney, L. N. Ayton, L. M. Lucci, W. C. Hubbard, J. L. Hageman, G. S. Hageman, and R. H. Guymer, "Reticular pseudodrusen: a risk factor for geographic atrophy in fellow eyes of individuals with unilateral choroidal neovascularization," Ophthalmology **121**, 1252-1256 (2014).
8. M. Fleckenstein, P. Mitchell, K. B. Freund, S. Sadda, F. G. Holz, C. Brittain, E. C. Henry, and D. Ferrara, "The progression of geographic atrophy secondary to age-related macular degeneration," Ophthalmology **125**, 369-390 (2018).
9. L. G. Fritsche, R. N. Fariss, D. Stambolian, G. R. Abecasis, C. A. Curcio, and A. Swaroop, "Age-related macular degeneration: genetics and biology coming together," Annu Rev Genomics Hum Genet **15**, 151-171 (2014).
10. S. Schmitz-Valckenberg, J.-A. Sahel, R. Danis, M. Fleckenstein, G. J. Jaffe, S. Wolf, C. Pruente, and F. G. Holz, "Natural history of geographic atrophy progression secondary to age-related macular degeneration (Geographic Atrophy Progression Study)," Ophthalmology **123**, 361-368 (2016).
11. D. M. Brown, P. K. Kaiser, M. Michels, G. Soubrane, J. S. Heier, R. Y. Kim, J. P. Sy, and S. Schneider, "Ranibizumab versus verteporfin for neovascular age-related macular degeneration," N Engl J Med **355**, 1432-1444 (2006).
12. A. R. Rudnicka, V. V. Kapetanakis, Z. Jarrar, A. K. Wathern, R. Wormald, A. E. Fletcher, D. G. Cook, and C. G. Owen, "Incidence of Late-Stage Age-Related Macular Degeneration in American Whites: Systematic Review and Meta-analysis," Am J Ophthalmol **160**, 85-93.e83 (2015).
13. A. Domalpally, R. P. Danis, R. Trane, B. A. Blodi, T. E. Clemons, and E. Y. Chew, "Atrophy in Neovascular Age-Related Macular Degeneration: Age-Related Eye Disease Study 2 Report Number 15," Ophthalmol Retina **2**, 1021-1027 (2018).
14. S. Vitale, T. E. Clemons, E. Agrón, F. L. Ferris, A. Domalpally, R. P. Danis, E. Y. Chew, and A.-R. E. D. S. R. Group, "Evaluating the validity of the Age-Related Eye Disease Study grading scale for age-related macular degeneration: AREDS2 Report 10," JAMA ophthalmology **134**, 1041-1047 (2016).
15. R. P. Danis, J. A. Lavine, and A. Domalpally, "Geographic atrophy in patients with advanced dry age-related macular degeneration: current challenges and future prospects," Clinical Ophthalmology (Auckland, NZ) **9**, 2159 (2015).
16. J. Hanus, F. Zhao, and S. Wang, "Current therapeutic developments in atrophic age-related macular degeneration," British Journal of Ophthalmology **100**, 122-127 (2016).

17. F. G. Holz, E. C. Strauss, S. Schmitz-Valckenberg, and M. van Lookeren Campagne, "Geographic atrophy: clinical features and potential therapeutic approaches," Ophthalmology **121**, 1079-1091 (2014).
18. K. B. Schaal, P. J. Rosenfeld, G. Gregori, Z. Yehoshua, and W. J. Feuer, "Anatomic clinical trial endpoints for nonexudative age-related macular degeneration," Ophthalmology **123**, 1060-1079 (2016).
19. M. Rudolf, S. D. Vogt, C. A. Curcio, C. Huisingh, G. McGwin Jr, A. Wagner, S. Grisanti, and R. W. Read, "Histologic basis of variations in retinal pigment epithelium autofluorescence in eyes with geographic atrophy," Ophthalmology **120**, 821-828 (2013).
20. B. Povazay, A. A. Apolonski, A. Unterhuber, B. Hermann, K. K. Bizheva, H. Sattmann, P. S. J. Russell, F. Krausz, A. F. Fercher, and W. Drexler, "Visible light optical coherence tomography," in *Coherence Domain Optical Methods in Biomedical Science and Clinical Applications VI*, (International Society for Optics and Photonics, 2002), 90-94.
21. B. Povazay, K. Bizheva, A. Unterhuber, B. Hermann, H. Sattmann, A. F. Fercher, W. Drexler, A. Apolonski, W. Wadsworth, and J. Knight, "Submicrometer axial resolution optical coherence tomography," Optics letters **27**, 1800-1802 (2002).
22. J. Yi, Q. Wei, W. Liu, V. Backman, and H. F. Zhang, "Visible-light optical coherence tomography for retinal oximetry," Optics letters **38**, 1796-1798 (2013).
23. S. P. Chong, M. Bernucci, H. Radhakrishnan, and V. J. Srinivasan, "Structural and functional human retinal imaging with a fiber-based visible light OCT ophthalmoscope," Biomedical optics express **8**, 323-337 (2017).
24. S. Pi, A. Camino, M. Zhang, W. Cepurna, G. Liu, D. Huang, J. Morrison, and Y. Jia, "Angiographic and structural imaging using high axial resolution fiber-based visible-light OCT," Biomedical optics express **8**, 4595-4608 (2017).
25. S. Pi, T. T. Hormel, X. Wei, W. Cepurna, B. Wang, J. C. Morrison, and Y. Jia, "Retinal capillary oximetry with visible light optical coherence tomography," Proceedings of the National Academy of Sciences **117**, 11658-11666 (2020).
26. D. J. Harper, M. Augustin, A. Lichtenegger, P. Eugui, C. Reyes, M. Glösmann, C. K. Hitzenberger, and B. Baumann, "White light polarization sensitive optical coherence tomography for sub-micron axial resolution and spectroscopic contrast in the murine retina," Biomedical optics express **9**, 2115-2129 (2018).
27. Z. Nafar, M. Jiang, R. Wen, and S. Jiao, "Visible-light optical coherence tomography-based multimodal retinal imaging for improvement of fluorescent intensity quantification," Biomedical optics express **7**, 3220-3229 (2016).
28. M. J. Ju, C. Huang, D. J. Wahl, Y. Jian, and M. V. Sarunic, "Visible light sensorless adaptive optics for retinal structure and fluorescence imaging," Optics letters **43**, 5162-5165 (2018).
29. S. P. Chong, C. W. Merkle, C. Leahy, H. Radhakrishnan, and V. J. Srinivasan, "Quantitative microvascular hemoglobin mapping using visible light spectroscopic Optical Coherence Tomography," Biomed Opt Express **6**, 1429-1450 (2015).
30. F. E. Robles, C. Wilson, G. Grant, and A. Wax, "Molecular imaging true-colour spectroscopic optical coherence tomography," Nature photonics **5**, 744-747 (2011).
31. F. Robles, R. N. Graf, and A. Wax, "Dual window method for processing spectroscopic optical coherence tomography signals with simultaneously high spectral and temporal resolution," Optics express **17**, 6799-6812 (2009).
32. A. Kho and V. J. Srinivasan, "Compensating spatially dependent dispersion in visible light OCT," Optics letters **44**, 775-778 (2019).
33. S. P. Chong, T. Zhang, A. Kho, M. T. Bernucci, A. Dubra, and V. J. Srinivasan, "Ultrahigh resolution retinal imaging by visible light OCT with longitudinal achromatization," Biomed Opt Express **9**, 1477-1491 (2018).
34. T. Zhang, A. M. Kho, and V. J. Srinivasan, "Improving visible light OCT of the human retina with rapid spectral shaping and axial tracking," Biomedical optics express **10**, 2918-2931 (2019).
35. Z. Ansi, "136.1 „American National Standard for Safe Use of Lasers," Laser Institute of America, Orlando (2000).
36. P. Youssef, N. Sheibani, and D. Albert, "Retinal light toxicity," Eye **25**, 1-14 (2011).
37. J. J. Hunter, J. I. Morgan, W. H. Merigan, D. H. Sliney, J. R. Sparrow, and D. R. Williams, "The susceptibility of the retina to photochemical damage from visible light," Progress in retinal and eye research **31**, 28-42 (2012).
38. X. Zhang, J. Hu, R. W. Knighton, X.-R. Huang, C. A. Puliafito, and S. Jiao, "Visible light optical coherence tomography for in vivo imaging the spectral contrasts of the retinal nerve fiber layer," in *Optical Coherence Tomography and Coherence Domain Optical Methods in Biomedicine XVI*, (International Society for Optics and Photonics, 2012), 82130H.

39. K. V. Vienola, B. Braaf, C. K. Sheehy, Q. Yang, P. Tiruveedhula, D. W. Arathorn, J. F. de Boer, and A. Roorda, "Real-time eye motion compensation for OCT imaging with tracking SLO," Biomedical optics express **3**, 2950-2963 (2012).
40. D. X. Hammer, T. E. Ustun, N. V. Iftimia, J. C. Magill, and R. D. Ferguson, "Dual OCT-SLO imager with 3D tracker," in *Ophthalmic Technologies XV*, (International Society for Optics and Photonics, 2005), 33-44.
41. M. F. Kraus, B. Potsaid, M. A. Mayer, R. Bock, B. Baumann, J. J. Liu, J. Hornegger, and J. G. Fujimoto, "Motion correction in optical coherence tomography volumes on a per A-scan basis using orthogonal scan patterns," Biomedical optics express **3**, 1182-1199 (2012).
42. Y. Chen, Y.-J. Hong, S. Makita, and Y. Yasuno, "Three-dimensional eye motion correction by Lissajous scan optical coherence tomography," Biomedical optics express **8**, 1783-1802 (2017).
43. D. C. Adler, R. Huber, and J. G. Fujimoto, "Phase-sensitive optical coherence tomography at up to 370,000 lines per second using buffered Fourier domain mode-locked lasers," Optics letters **32**, 626-628 (2007).
44. M. Azimipour, J. V. Migacz, R. J. Zawadzki, J. S. Werner, and R. S. Jonnal, "Functional retinal imaging using adaptive optics swept-source OCT at 1.6 MHz," Optica **6**, 300-303 (2019).
45. D. Hillmann, H. Spahr, C. Pfäffle, H. Sudkamp, G. Franke, and G. Hüttmann, "In vivo optical imaging of physiological responses to photostimulation in human photoreceptors," Proceedings of the National Academy of Sciences **113**, 13138-13143 (2016).
46. O. P. Kocaoglu, T. L. Turner, Z. Liu, and D. T. Miller, "Adaptive optics optical coherence tomography at 1 MHz," Biomedical optics express **5**, 4186-4200 (2014).
47. S. Mozaffari, F. Feroldi, F. LaRocca, P. K. Tiruveedhula, P. Gregory, B. H. Park, and A. J. Roorda, "Actively stabilized AOOCT with independent focus adjustment for optimal AOSLO-based eye tracking," Investigative Ophthalmology & Visual Science **62**, 10-10 (2021).
48. D. J. Fechtig, B. Grajciar, T. Schmoll, C. Blatter, R. M. Werkmeister, W. Drexler, and R. A. Leitgeb, "Line-field parallel swept source MHz OCT for structural and functional retinal imaging," Biomedical optics express **6**, 716-735 (2015).
49. T. Bonin, G. Franke, M. Hagen-Eggert, P. Koch, and G. Hüttmann, "In vivo Fourier-domain full-field OCT of the human retina with 1.5 million A-lines/s," Optics letters **35**, 3432-3434 (2010).
50. Y. Benny, S. Manzanera, P. M. Prieto, E. N. Ribak, and P. Artal, "Wide-angle chromatic aberration corrector for the human eye," JOSA A **24**, 1538-1544 (2007).
51. R. J. Zawadzki, B. Cense, Y. Zhang, S. S. Choi, D. T. Miller, and J. S. Werner, "Ultrahigh-resolution optical coherence tomography with monochromatic and chromatic aberration correction," Optics express **16**, 8126-8143 (2008).
52. A. M. Kho, T. Zhang, J. Zhu, C. W. Merkle, and V. J. Srinivasan, "Incoherent excess noise spectrally encodes broadband light sources," Light: Science & Applications **9**, 1-9 (2020).
53. P. Zhang, M. Goswami, R. J. Zawadzki, and E. N. Pugh, "The photosensitivity of rhodopsin bleaching and light-induced increases of fundus reflectance in mice measured in vivo with scanning laser ophthalmoscopy," Investigative ophthalmology & visual science **57**, 3650-3664 (2016).
54. R. K. Meleppat, P. Zhang, M. J. Ju, S. K. Manna, Y. Jian, E. N. Pugh, and R. J. Zawadzki, "Directional optical coherence tomography reveals melanin concentration-dependent scattering properties of retinal pigment epithelium," Journal of biomedical optics **24**, 066011 (2019).
55. M. T. Bernucci, C. W. Merkle, and V. J. Srinivasan, "Investigation of artifacts in retinal and choroidal OCT angiography with a contrast agent," Biomedical optics express **9**, 1020-1040 (2018).
56. T. Lamb and E. Pugh Jr, "Dark adaptation and the retinoid cycle of vision," Progress in retinal and eye research **23**, 307-380 (2004).
57. S. P. Chong, C. W. Merkle, C. Leahy, H. Radhakrishnan, and V. J. Srinivasan, "Quantitative microvascular hemoglobin mapping using visible light spectroscopic Optical Coherence Tomography," Biomedical optics express **6**, 1429-1450 (2015).
58. J. Yi, S. Chen, X. Shu, A. A. Fawzi, and H. F. Zhang, "Human retinal imaging using visible-light optical coherence tomography guided by scanning laser ophthalmoscopy," Biomed. Opt. Express **6**, 3701-3713 (2015).
59. V. Srinivasan, M. Wojtkowski, J. Fujimoto, and J. Duker, "In vivo measurement of retinal physiology with high-speed ultrahigh-resolution optical coherence tomography," Optics letters **31**, 2308-2310 (2006).
60. W. J. Brown, S. Kim, and A. Wax, "Noise characterization of supercontinuum sources for low-coherence interferometry applications," JOSA A **31**, 2703-2710 (2014).

61. M. Wojtkowski, V. Srinivasan, T. Ko, J. Fujimoto, A. Kowalczyk, and J. Duker, "Ultrahigh-resolution, high-speed, Fourier domain optical coherence tomography and methods for dispersion compensation," Opt Express **12**, 2404-2422 (2004).
62. D. L. Marks, A. L. Oldenburg, J. J. Reynolds, and S. A. Boppart, "Digital algorithm for dispersion correction in optical coherence tomography for homogeneous and stratified media," Applied optics **42**, 204-217 (2003).
63. A. G. Van Engen, S. A. Diddams, and T. S. Clement, "Dispersion measurements of water with white-light interferometry," Applied optics **37**, 5679-5686 (1998).
64. W. Choi, B. Baumann, E. A. Swanson, and J. G. Fujimoto, "Extracting and compensating dispersion mismatch in ultrahigh-resolution Fourier domain OCT imaging of the retina," Optics express **20**, 25357-25368 (2012).
65. B. Cense, N. A. Nassif, T. C. Chen, M. C. Pierce, S.-H. Yun, B. H. Park, B. E. Bouma, G. J. Tearney, and J. F. de Boer, "Ultrahigh-resolution high-speed retinal imaging using spectral-domain optical coherence tomography," Optics Express **12**, 2435-2447 (2004).
66. A. F. Fercher, C. K. Hitzenberger, G. Kamp, and S. Y. El-Zaiat, "Measurement of intraocular distances by backscattering spectral interferometry," Optics communications **117**, 43-48 (1995).
67. G. Lu and B. Fei, "Medical hyperspectral imaging: a review," Journal of biomedical optics **19**, 010901 (2014).
68. D. A. Long and D. Long, *Raman spectroscopy* (McGraw-Hill New York, 1977), Vol. 276.
69. J. B. Reeves III, "Near-versus mid-infrared diffuse reflectance spectroscopy for soil analysis emphasizing carbon and laboratory versus on-site analysis: where are we and what needs to be done?," Geoderma **158**, 3-14 (2010).
70. A. A. Bol'Shakov, J. H. Yoo, C. Liu, J. R. Plumer, and R. E. Russo, "Laser-induced breakdown spectroscopy in industrial and security applications," Applied Optics **49**, C132-C142 (2010).
71. S. Yun, G. Tearney, B. Bouma, B. Park, and J. F. de Boer, "High-speed spectral-domain optical coherence tomography at 1.3 μm wavelength," Optics express **11**, 3598-3604 (2003).
72. R. Leitgeb, C. Hitzenberger, and A. F. Fercher, "Performance of fourier domain vs. time domain optical coherence tomography," Optics express **11**, 889-894 (2003).
73. C. Dorrer, N. Belabas, J.-P. Likforman, and M. Joffre, "Spectral resolution and sampling issues in Fourier-transform spectral interferometry," JOSA B **17**, 1795-1802 (2000).
74. R. R. Alfano, "The supercontinuum laser source," (1989).
75. K. L. Corwin, N. R. Newbury, J. M. Dudley, S. Coen, S. A. Diddams, B. R. Washburn, K. Weber, and R. S. Windeler, "Fundamental amplitude noise limitations to supercontinuum spectra generated in a microstructured fiber," Applied Physics B **77**, 269-277 (2003).
76. L. Mandel, "Fluctuations of photon beams and their correlations," Proceedings of the Physical Society (1958-1967) **72**, 1037 (1958).
77. J. F. De Boer, B. Cense, B. H. Park, M. C. Pierce, G. J. Tearney, and B. E. Bouma, "Improved signal-to-noise ratio in spectral-domain compared with time-domain optical coherence tomography," Optics letters **28**, 2067-2069 (2003).
78. W. V. Sorin and D. M. Baney, "A simple intensity noise reduction technique for optical low-coherence reflectometry," IEEE Photonics Technology Letters **4**, 1404-1406 (1992).
79. S. Shin, U. Sharma, H. Tu, W. Jung, and S. A. Boppart, "Characterization and analysis of relative intensity noise in broadband optical sources for optical coherence tomography," IEEE Photonics Technology Letters **22**, 1057-1059 (2010).
80. L. Mandel, "Fluctuations of photon beams and their correlations," Proceedings of the Physical Society **72**, 1037 (1958).
81. H. Hodara, "Statistics of thermal and laser radiation," Proceedings of the IEEE **53**, 696-704 (1965).
82. J. M. Dudley, G. Genty, and S. Coen, "Supercontinuum generation in photonic crystal fiber," Reviews of modern physics **78**, 1135 (2006).
83. B. Wetzel, A. Stefani, L. Larger, P.-A. Lacourt, J.-M. Merolla, T. Sylvestre, A. Kudlinski, A. Mussot, G. Genty, and F. Dias, "Real-time full bandwidth measurement of spectral noise in supercontinuum generation," Scientific reports **2**, 882 (2012).
84. P. Béjot, J. Kasparian, E. Salmon, R. Ackermann, and J.-P. Wolf, "Spectral correlation and noise reduction in laser filaments," Applied Physics B **87**, 1 (2007).
85. B. H. Park, M. C. Pierce, B. Cense, S.-H. Yun, M. Mujat, G. J. Tearney, B. E. Bouma, and J. F. de Boer, "Real-time fiber-based multi-functional spectral-domain optical coherence tomography at 1.3 μm," Optics Express **13**, 3931-3944 (2005).

86. E. Götzinger, M. Pircher, and C. K. Hitzenberger, "High speed spectral domain polarization sensitive optical coherence tomography of the human retina," Optics express **13**, 10217-10229 (2005).
87. S. Makita, T. Fabritius, and Y. Yasuno, "Full-range, high-speed, high-resolution 1-μm spectral-domain optical coherence tomography using BM-scan for volumetric imaging of the human posterior eye," Optics express **16**, 8406-8420 (2008).
88. D. Huang, E. A. Swanson, C. P. Lin, J. S. Schuman, W. G. Stinson, W. Chang, M. R. Hee, T. Flotte, K. Gregory, and C. A. Puliafito, "Optical coherence tomography," science **254**, 1178-1181 (1991).
89. M. Jensen, I. B. Gonzalo, R. D. Engelsholm, M. Maria, N. M. Israelsen, A. Podoleanu, and O. Bang, "Noise of supercontinuum sources in spectral domain optical coherence tomography," JOSA B **36**, A154-A160 (2019).
90. W. J. Brown, S. Kim, and A. Wax, "Noise characterization of supercontinuum sources for low-coherence interferometry applications," J. Opt. Soc. Am. A **31**, 2703-2710 (2014).
91. X. Yao, Y. Gan, C. C. Marboe, and C. P. Hendon, "Myocardial imaging using ultrahigh-resolution spectral domain optical coherence tomography," Journal of biomedical optics **21**, 061006 (2016).
92. S. P. Chong, M. Bernucci, H. Radhakrishnan, and V. J. Srinivasan, "Structural and functional human retinal imaging with a fiber-based visible light OCT ophthalmoscope," Biomed Opt Express **8**, 323-337 (2017).
93. M. A. Choma, M. V. Sarunic, C. Yang, and J. A. Izatt, "Sensitivity advantage of swept source and Fourier domain optical coherence tomography," Optics express **11**, 2183-2189 (2003).
94. A. G. van Rossum, W. M. Aartsen, J. Meuleman, J. Klooster, A. Malysheva, I. Versteeg, J.-P. Arsanto, A. Le Bivic, and J. Wijnholds, "Pals1/Mpp5 is required for correct localization of Crb1 at the subapical region in polarized Müller glia cells," Human molecular genetics **15**, 2659-2672 (2006).
95. E. West, R. Pearson, M. Tschernutter, J. Sowden, R. MacLaren, and R. Ali, "Pharmacological disruption of the outer limiting membrane leads to increased retinal integration of transplanted photoreceptor precursors," Experimental eye research **86**, 601-611 (2008).
96. J. W. Goodman, "Statistical properties of laser speckle patterns," in *Laser speckle and related phenomena* (Springer, 1975), pp. 9-75.
97. D. A. Boas and A. K. Dunn, "Laser speckle contrast imaging in biomedical optics," Journal of biomedical optics **15**, 011109 (2010).
98. S.-W. Lee, H.-W. Jeong, B.-M. Kim, Y.-C. Ahn, W. Jung, and Z. Chen, "Optimization for axial resolution, depth range, and sensitivity of spectral domain optical coherence tomography at 1.3 μm," The journal of the Korean Physical Society **55**, 2354 (2009).
99. Z. Hu, Y. Pan, and A. M. Rollins, "Analytical model of spectrometer-based two-beam spectral interferometry," Applied optics **46**, 8499-8505 (2007).
100. Z. Hu and A. M. Rollins, "Fourier domain optical coherence tomography with a linear-in-wavenumber spectrometer," Optics letters **32**, 3525-3527 (2007).
101. K. L. Corwin, N. R. Newbury, J. M. Dudley, S. Coen, S. A. Diddams, K. Weber, and R. Windeler, "Fundamental noise limitations to supercontinuum generation in microstructure fiber," Physical review letters **90**, 113904 (2003).
102. T. Hori, J. Takayanagi, N. Nishizawa, and T. Goto, "Flatly broadened, wideband and low noise supercontinuum generation in highly nonlinear hybrid fiber," Optics Express **12**, 317-324 (2004).
103. S. Rao D. S, M. Jensen, L. Grüner-Nielsen, J. T. Olsen, P. Heiduschka, B. Kemper, J. Schnekenburger, M. Glud, M. Mogensen, N. M. Israelsen, and O. Bang, "Shot-noise limited, supercontinuum-based optical coherence tomography," Light: Science & Applications **10**, 133 (2021).
104. B. M. Hoeling, A. D. Fernandez, R. C. Haskell, E. Huang, W. R. Myers, D. C. Petersen, S. E. Ungersma, R. Wang, M. E. Williams, and S. E. Fraser, "An optical coherence microscope for 3-dimensional imaging in developmental biology," Optics Express **6**, 136-146 (2000).
105. W. V. Sorin and D. M. Baney, "Measurement of Rayleigh Backscattering at 1.55 mu m with 32 mu m Spatial Resolution," IEEE Photonics Technology Letters **4**, 374-376 (1992).
106. A. G. Podoleanu, "Unbalanced versus balanced operation in an optical coherence tomography system," Applied Optics **39**, 173-182 (2000).
107. S. H. Yun, G. J. Tearney, J. F. de Boer, N. Iftimia, and B. E. Bouma, "High-speed optical frequency-domain imaging," Optics Express **11**, 2953-2963 (2003).
108. R. Huber, M. Wojtkowski, K. Taira, J. G. Fujimoto, and K. Hsu, "Amplified, frequency swept lasers for frequency domain reflectometry and OCT imaging: design and scaling principles," Optics express **13**, 3513-3528 (2005).

109. A. Bradu and A. G. Podoleanu, "Fourier domain optical coherence tomography system with balance detection," Optics express **20**, 17522-17538 (2012).
110. J. F. de Boer, B. Cense, B. H. Park, M. C. Pierce, G. J. Tearney, and B. E. Bouma, "Improved signal-to-noise ratio in spectral-domain compared with time-domain optical coherence tomography," Opt Lett **28**, 2067-2069 (2003).
111. A. J. Black and T. Akkin, "Polarization-based balanced detection for spectral-domain optical coherence tomography," Appl Opt **54**, 7252-7257 (2015).
112. A. Bradu and A. G. Podoleanu, "Fourier domain optical coherence tomography system with balance detection," Opt Express **20**, 17522-17538 (2012).
113. M. G. Hyeon, H. J. Kim, B. M. Kim, and T. J. Eom, "Spectral domain optical coherence tomography with balanced detection using single line-scan camera and optical delay line," Opt Express **23**, 23079-23091 (2015).
114. C. Dai, X. Liu, and S. Jiao, "Simultaneous optical coherence tomography and autofluorescence microscopy with a single light source," Journal of biomedical optics **17**, 080502 (2012).
115. R. C. Niemeier, Z. J. Simmons, and J. D. Rogers, "Noise reduction in supercontinuum sources for OCT by single-pulse spectral normalization," Applied Optics **59**, 5521-5526 (2020).
116. Y. Chen, D. M. de Bruin, C. Kerbage, and J. F. de Boer, "Spectrally balanced detection for optical frequency domain imaging," Optics express **15**, 16390-16399 (2007).
117. A. M. Kho, T. Zhang, J. Zhu, C. W. Merkle, and V. J. Srinivasan, "Incoherent excess noise spectrally encodes broadband light sources," Light Sci Appl **9**, 172 (2020).
118. W.-C. Kuo, Y.-S. Lai, C.-M. Lai, and Y.-S. Huang, "Balanced detection spectral domain optical coherence tomography with a multiline single camera for signal-to-noise ratio enhancement," Applied optics **51**, 5936-5940 (2012).
119. W.-C. Kuo, C.-M. Lai, Y.-S. Huang, C.-Y. Chang, and Y.-M. Kuo, "Balanced detection for spectral domain optical coherence tomography," Optics express **21**, 19280-19291 (2013).
120. E. Bo, X. Liu, S. Chen, X. Yu, X. Wang, and L. Liu, "Spectral-domain optical coherence tomography with dual-balanced detection for auto-correlation artifacts reduction," Optics express **23**, 28050-28058 (2015).
121. M. G. Hyeon, H.-J. Kim, B.-M. Kim, and T. J. Eom, "Spectral domain optical coherence tomography with balanced detection using single line-scan camera and optical delay line," Optics express **23**, 23079-23091 (2015).
122. R. Tripathi, N. Nassif, J. S. Nelson, B. H. Park, and J. F. de Boer, "Spectral shaping for non-Gaussian source spectra in optical coherence tomography," Opt Lett **27**, 406-408 (2002).
123. N. Wiener, *Extrapolation, Interpolation, and Smoothing of Stationary Time Series: With Engineering Applications* (Technology Press of M.I.T. and Wiley, 1957).
124. T. Kailath, A. H. Sayed, and B. Hassibi, *Linear Estimation* (Prentice Hall, 2000).
125. J. Bibby, J. M. Bibby, and H. Toutenburg, *Prediction and Improved Estimation in Linear Models* (Wiley, 1977).
126. P. Zhang, E. B. Miller, S. K. Manna, R. K. Meleppat, E. N. Pugh, and R. Zawadzki, "Temporal speckle-averaging of optical coherence tomography volumes for in-vivo cellular resolution neuronal and vascular retinal imaging," Neurophotonics **6**, 041105 (2019).
127. W. Song, W. Shao, and J. Yi, "Wide-Field and Micron-Resolution Visible Light Optical Coherence Tomography in Human Retina by a Linear-K Spectrometer," in *Bio-Optics: Design and Application*, (Optical Society of America, 2021), DM2A. 4.
128. D. J. Harper, M. Augustin, A. Lichtenegger, P. Eugui, C. Reyes, M. Glosmann, C. K. Hitzenberger, and B. Baumann, "White light polarization sensitive optical coherence tomography for sub-micron axial resolution and spectroscopic contrast in the murine retina," Biomed Opt Express **9**, 2115-2129 (2018).
129. D. J. Harper, T. Konegger, M. Augustin, K. Schützenberger, P. Eugui, A. Lichtenegger, C. W. Merkle, C. K. Hitzenberger, M. Glösmann, and B. Baumann, "Hyperspectral optical coherence tomography for in vivo visualization of melanin in the retinal pigment epithelium," Journal of biophotonics **12**, e201900153 (2019).
130. I. Rubinoff, L. Beckmann, Y. Wang, A. A. Fawzi, X. Liu, J. Tauber, K. Jones, H. Ishikawa, J. S. Schuman, and R. Kuranov, "Speckle reduction in visible-light optical coherence tomography using scan modulation," Neurophotonics **6**, 041107 (2019).
131. S. Chen, X. Shu, J. Yi, A. A. Fawzi, and H. F. Zhang, "Dual-band optical coherence tomography using a single supercontinuum laser source," Journal of biomedical optics **21**, 066013 (2016).
132. "ANSI Z80.36 Ophthalmics - Light Hazard Protection For Ophthalmic Instruments," Laser Institute of America (2016).

133. P. Zhang, R. J. Zawadzki, M. Goswami, P. T. Nguyen, V. Yarov-Yarovoy, M. E. Burns, and E. N. Pugh, "In vivo optophysiology reveals that G-protein activation triggers osmotic swelling and increased light scattering of rod photoreceptors," Proceedings of the National Academy of Sciences **114**, E2937-E2946 (2017).
134. Q.-X. Zhang, R.-W. Lu, J. D. Messinger, C. A. Curcio, V. Guarcello, and X.-C. Yao, "In vivo optical coherence tomography of light-driven melanosome translocation in retinal pigment epithelium," Scientific reports **3**, 1-8 (2013).
135. T. Zhang, A. M. Kho, G. Yiu, and V. J. Srinivasan, "Visible Light Optical Coherence Tomography (OCT) Quantifies Subcellular Contributions to Outer Retinal Band 4," Transl Vis Sci Technol **10**, 30 (2021).
136. R. K. Meleppat, K. E. Ronning, S. J. Karlen, M. E. Burns, E. N. Pugh, and R. J. Zawadzki, "In vivo multimodal retinal imaging of disease-related pigmentary changes in retinal pigment epithelium," Scientific reports **11**, 1-14 (2021).
137. J.-D. Ding, R. Y. Salinas, and V. Y. Arshavsky, "Discs of mammalian rod photoreceptors form through the membrane evagination mechanism," Journal of Cell Biology **211**, 495-502 (2015).
138. C. Curcio, C. L. Millican, K. Allen, and R. Kalina, "Aging of the human photoreceptor mosaic: evidence for selective vulnerability of rods in central retina," Investigative ophthalmology & visual science **34**, 3278-3296 (1993).
139. C. A. Curcio, C. Owsley, and G. R. Jackson, "Spare the rods, save the cones in aging and age-related maculopathy," Investigative ophthalmology & visual science **41**, 2015-2018 (2000).
140. G. R. Jackson and C. Owsley, "Scotopic sensitivity during adulthood," Vision research **40**, 2467-2473 (2000).
141. C. Owsley, G. R. Jackson, A. V. Cideciyan, Y. Huang, S. L. Fine, A. C. Ho, M. G. Maguire, V. Lolley, and S. G. Jacobson, "Psychophysical evidence for rod vulnerability in age-related macular degeneration," Investigative ophthalmology & visual science **41**, 267-273 (2000).
142. G. R. Jackson, C. Owsley, and G. McGwin Jr, "Aging and dark adaptation," Vision research **39**, 3975-3982 (1999).
143. C. Owsley, G. R. Jackson, M. White, R. Feist, and D. Edwards, "Delays in rod-mediated dark adaptation in early age-related maculopathy," Ophthalmology **108**, 1196-1202 (2001).
144. R. Sabesan, H. Hofer, and A. Roorda, "Characterizing the human cone photoreceptor mosaic via dynamic photopigment densitometry," PloS one **10**, e0144891 (2015).
145. S. Y. Schmidt and R. D. Peisch, "Melanin concentration in normal human retinal pigment epithelium. Regional variation and age-related reduction," Investigative ophthalmology & visual science **27**, 1063-1067 (1986).
146. A. E. Elsner, S. A. Burns, E. Beausencourt, and J. J. Weiter, "Foveal cone photopigment distribution: small alterations associated with macular pigment distribution," Investigative ophthalmology & visual science **39**, 2394-2404 (1998).
147. A. E. Elsner, S. A. Burns, and L. A. Lobes, "Foveal cone optical density in retinitis pigmentosa," Applied optics **26**, 1378-1384 (1987).
148. A. E. Elsner, S. A. Burns, G. W. Hughes, and R. H. Webb, "Reflectometry with a scanning laser ophthalmoscope," Applied optics **31**, 3697-3710 (1992).
149. A. E. Elsner, S. A. Burns, and R. H. Webb, "Mapping cone photopigment optical density," JOSA A **10**, 52-58 (1993).
150. H. L. Ramkumar, J. Zhang, and C.-C. Chan, "Retinal ultrastructure of murine models of dry age-related macular degeneration (AMD)," Progress in retinal and eye research **29**, 169-190 (2010).
151. J. Wang, K. Ohno-Matsui, T. Yoshida, A. Kojima, N. Shimada, K.-i. Nakahama, O. Safranova, N. Iwata, T. C. Saido, and M. Mochizuki, "Altered function of factor I caused by amyloid β: implication for pathogenesis of age-related macular degeneration from drusen," The Journal of Immunology **181**, 712-720 (2008).
152. T. Yoshida, K. Ohno-Matsui, S. Ichinose, T. Sato, N. Iwata, T. C. Saido, T. Hisatomi, M. Mochizuki, and I. Morita, "The potential role of amyloid β in the pathogenesis of age-related macular degeneration," The Journal of clinical investigation **115**, 2793-2800 (2005).
153. T. Zhang, A. M. Kho, and V. J. Srinivasan, "In vivo morphometry of inner plexiform layer (IPL) stratification in the human retina with visible light Optical Coherence Tomography," Frontiers in Cellular Neuroscience **15**(2021).